TRANSIENT SIMULATION OF AMMONIA-WATER MIXTURE DESORPTION FOR ABSORPTION HEAT PUMPS

AND

OPTIMAL CONTROL OF AN ELECTRIC VEHICLE CABIN AIR CONDITIONING SYSTEM

A Thesis
Presented to
The Academic Faculty

By

Alexander Aryn Roeder

In Partial Fulfillment
Of the Requirement for the Degree
Master of Science in Mechanical Engineering

Georgia Institute of Technology

December 2018

TRANSIENT SIMULATION OF AMMONIA-WATER MIXTURE DESORPTION FOR ABSORPTION HEAT PUMPS

AND

OPTIMAL CONTROL OF AN ELECTRIC VEHICLE CABIN AIR CONDITIONING SYSTEM

Approved by:

Dr. Srinivas Garimella, Advisor
Woodruff School of Mechanical Engineering
Georgia Institute of Technology

Dr. G. Paul Neitzel
Woodruff School of Mechanical Engineering
Georgia Institute of Technology

Professor Dr. Oliver Sawodny
Institüt for Systemdynamik
Universität Stuttgart

Dr. Ulf Säger
Research and Development
Daimler AG

Date Approved: September 24, 2018

DEDICATION

To my entire family, Jackie, Gary, and Derek Roeder, for their support in all my pursuits in life and continually pushing me to be the best I can be.

ACKNOWLEDGEMENTS

I would first like to thank my advisor from the Georgia Institute of Technology, Dr. Srinivas Garimella, for his guidance, support, and advice throughout the course of this work. He took a chance on me when he brought me under his wing. I cannot thank him enough for the opportunity.

Next, I would like to thank my mentor at Daimler AG, Dr. Ulf Säger. The opportunity to work at a German automotive company was a childhood dream come true for me. Dr. Säger's mentorship made my time at Daimler a truly memorable experience, even if I got lost some days in Deutsch.

I would like to give my utmost thanks to the members of the Sustainable Thermal Systems Laboratory (STSL), especially Anurag Goyal, Marcel Staedter, and Daniel Boman for their input and support during my Masters work while in Atlanta. From Universität Stuttgart, I would like to thank Stefan Schaut from the Institute for System Dynamics (ISYS) for his guidance in assembling Part II of this thesis.

I would like to thank the rest of the members of my committee, Dr. G. Paul Neitzel from the Woodruff School of Mechanical Engineering at the Georgia Institute of Technology and Prof. Dr. Oliver Sawodny from the Institut für Systemdynamik at Universtät Stuttgart, for their input and guidance in this work.

Finally, I would also like to thank Advanced Research Projects Agency (ARPA-E) (Award #: DE-AR0000370) and Daimler AG for the financial support for this work.

Table of Contents

Acknowledgements ..... **iv**

List of Tables ..... **ix**

List of Figures ..... **x**

Nomenclature ..... **xiii**

Summary ..... **xvii**

Part I **1**

1. Introduction **2**

2. Mathematical modeling **5**

2.1 Governing equations 6

2.2 Discretized equations 10

2.3 Geometric and heat transfer parameters 13

3. Solver implementation **16**

3.1 Boundary and initial conditions 16

3.1.1. Input parameter ramping function 16

3.2 DAE solver 18

4. Results and discussion **21**

4.1 Simulation parameters 21

4.2 Steady-state performance 23

4.3 Start-up performance 26

4.3.1. Variation of temperatures 29

4.3.2. Variation of heat transfer rates 30

4.3.3. Variation of outlet mass flow rates 33

4.3.4. Run time of cases considered 34

4.4 Transient performance 34

4.4.1. Response to change in solution inlet mass flow rate 34

4.4.2. Response to change in coupling fluid inlet temperature 42

4.4.3. Response to change in ambient temperature 49

5. Conclusions and Recommendations 58

5.1 Conclusions 58

5.2 Recommendations 59

Part II 61

6. Introduction 62

6.1 Overview 62

6.2 Climate conditioning in vehicles 63

6.2.1 Air conditioning system modeling 64

6.2.2 Cabin modeling 65

6.3 Climate control 66

6.4 Outline 69

7. Mathematical modeling 71

7.1 Cabin 71

7.1.1 Cabin outlet temperature 74

7.2 Air system 77

7.2.1 Recirculation flap 78

7.2.2 Blower 79

7.2.3 AC system 79

7.3 Overall model composition 82

7.4 Air property surfaces curve fits 83

8. Optimization and control 85

8.1 Optimal control problem formulation 85

8.1.1 Constraints 87

8.1.2 Integration method and solver 89

8.2 Benchmark control model 90

8.3 Software packages 92

8.3.1 MATLAB® 92

8.3.2 Simulink™ 92

8.3.3 CasADi & IPOPT 93

8.3.4 CoolProp 93

9. Results and Discussion 94

9.1 Simulation parameters 94

9.2 Basic test cases 97

9.3 Advanced test cases 105

9.3.1 Tunnel route 105

9.3.2 Variation in number of occupants 108

9.3.3 Thunderstorm 111

9.4 Summary of results 113

10. Conclusions and Recommendations 114

10.1 Conclusions 114

10.2 Recommendations 115

References 117

LIST OF TABLES

PART I

Table 1	Properties of desorber per solution plate and coupling fluid sheet pair.	14
Table 2	General simulation parameter values.	22
Table 3	Comparison of dynamic model and Delahanty (2015) component inputs.	23
Table 4	Initial and final conditions for start-up cases.	27
Table 5	Start-up simulation input times.	28
Table 6	Initial and final conditions, and simulation times for desorber solution inlet mass flow rate perturbation cases.	35
Table 7	Initial and final conditions, and simulation times for desorber coupling fluid inlet temperature perturbation cases.	43
Table 8	Initial and final conditions, and simulation times for desorber ambient temperature perturbation cases.	50

PART II

Table 9	Summary of the humid air property surface fits performed using the MATLAB® curve fitting toolbox.	84
Table 10	Summary of the constant cabin, ambient, and other simulation parameters.	95
Table 11	Disturbances and initials conditions for the basic test cases for the optimal controller and simple benchmark controller.	97
Table 12	Disturbances and initials conditions for the basic test cases for the optimal controller and simple benchmark controller.	98
Table 13	Results of the basic test cases for the optimal controller and simple benchmark controller.	99

LIST OF FIGURES

PART I

Figure 1	Schematic of the branched tray desorber.	5
Figure 2	Discretized desorber component; Left: solution-side discretization; Right: solution, wall, and coupling fluid region discretization.	10
Figure 3	Solution-side tray control volume.	11
Figure 4	Complete desorber solution plate (left) and coupling fluid sheet (right) pair (Keinath *et al.*, 2015).	13
Figure 5	Sigmoid ramping from 0.2 to 0.8 over 30 seconds.	18
Figure 6	MATLAB® ODE solver flowchart.	20
Figure 7	Comparison of the spatial variation of refrigerant vapor, dilute solution, and coupling fluid temperatures in the desorber at steady-state.	24
Figure 8	Comparison of sheet heat transfer as a function of solution inlet mass flow rate.	25
Figure 9	Time evolution of the solution and coupling fluid inlet and outlet temperatures.	30
Figure 10	Variation of desorber heat transfer rates during start-up.	31
Figure 11	Variation of the desorber inlet and outlet solution mass flow rates during start-up.	33
Figure 12	Response of desorber flow rates to an increase (A) and decrease (B) of solution inlet mass flow rate.	36
Figure 13	Response of desorber heat transfer rates to an increase (A) and decrease (B) of solution inlet mass flow rate.	38
Figure 14	Response of desorber temperatures to an increase (A) and decrease (B) of solution inlet mass flow rate.	40
Figure 15	Response of desorber concentrations to an increase (A) and decrease (B) of solution inlet mass flow rate.	41

Figure 16	Response of desorber flow rates to an increase (A) and decrease (B) in the coupling fluid inlet temperature.	44
Figure 17	Response of desorber heat transfer rates to an increase (left) and decrease (right) in the coupling fluid inlet temperature.	46
Figure 18	Response of desorber temperatures to an increase (A) and decrease (B) in the coupling fluid inlet temperature.	47
Figure 19	Response of desorber concentrations to an increase (A) and decrease (B) in the coupling fluid inlet temperature.	48
Figure 20	Response of desorber flow rates to an increase (A) and decrease (B) in ambient temperature.	52
Figure 21	Response of desorber heat transfer rates to an increase (A) and decrease (B) in ambient temperature.	53
Figure 22	Response of desorber temperatures to an increase (A) and decrease (B) in ambient temperature.	55
Figure 23	Response of desorber concentrations to an increase (A) and decrease (B) in ambient temperature.	56

PART II

Figure 24	Schematic of a common automotive AC system.	64
Figure 25	General vehicle diagram including cabin and air system.	71
Figure 26	Schematic of the vehicle cabin.	72
Figure 27	Comparison of cabin temperatures for various outlet air temperature equations: (A) Nitz and Hucho (1979), (B) Frank (1971), (C) average of cabin temperatures, and (D) equal to mean cabin air temperature.	76
Figure 28	Schematic of vehicle air system consisting of the recirculation flap, the blower, and the evaporator.	78
Figure 29	Psychrometric chart for humid air at atmospheric pressure. Red area highlights approximate operating range of the AC evaporator inlet and the blue area the approximate range of the evaporator outlet (Ogawa, 2009).	81

Figure 30	Comparison of the OCP and simple feedback controller input (Plot A) and state (Plot B) vector trajectories for basic test case 1.	100
Figure 31	Comparison of the OCP and simple feedback controller cabin mean air, mean interior surface, and outlet air temperature trajectories for basic test case 1.	102
Figure 32	Comparison of the OCP and simple feedback controller input (Plot A) and state (Plot B) vector trajectories for basic test case 6.	103
Figure 33	Comparison of the OCP and simple feedback controller cabin mean air, mean interior surface, and outlet air temperature trajectories for basic test case 6.	105
Figure 34	Disturbance vector trajectories for the simulated tunnel route. The tunnel period occurs during the period from 15 to 30 minutes.	106
Figure 35	Input (Plot A) and state (Plot B) vector trajectories for the simulated tunnel route.	107
Figure 36	Disturbance vector trajectories for the scenario of a variation in the number of passengers. The increase in the number of passengers occurs during the period from 5 to 30 minutes.	109
Figure 37	Input (Plot A) and state (Plot B) vector trajectories for the scenario of a variation in the number of passengers.	110
Figure 38	Disturbance vector trajectories for a simulated thunderstorm. The increase change in the ambient conditions begins at t = 5 minutes.	112
Figure 39	Input (Plot A) and state (Plot B) vector trajectories for a simulated thunderstorm.	113

NOMENCLATURE

PART I

Variables

A	Area (m^2)
CV	Control volume
Cp	Specific heat capacity (J kg^{-1} K^{-1})
δ	Energy residual (J s^{-1})
e	Specific internal energy (J kg^{-1})
$\dot{E}$	Energy storage rate (J s^{-1})
F	Ammonia-water property call
f_b	Body force vector (m s^{-2})
G	Input vector
h	Specific enthalpy (J kg^{-1})
κ	Sigmoid ramping function steepness (s^{-1})
m	Mass (kg)
$\dot{m}$	Mass flow rate (kg s^{-1})
M	Mass matrix
N	Number of trays or sets
v	Specific volume (m^3 kg^{-1})
P	Pressure (kPa)
$Pe\ (= RePr)$	Peclet Number
Per	Perimeter of flow passage (m)
Pr	Prandtl Number
q	Vapor mass quality (kg kg^{-1})
q''	Heat flux vector (J m^{-2} s^{-1})
$\dot{Q}$	Heat transfer rate (J s^{-1})
$\dot{Q}'''$	Volumetric heat transfer rate (J m^{-3} s^{-1})
Re	Reynolds Number
ρ	Density (kg m^{-3})
S	Sigmoid (logistic) ramping function
σ	Stress tensor (kg $m^{-1}s^{-2}$)
t	Time (s)
T	Temperature (K)
τ	Shear stress tensor (kg $m^{-1}s^{-2}$)
u	Axial velocity (m s^{-1})
U	Heat transfer coefficient (W m^{-2} K^{-1})
UA	Overall conductance (W K^{-1})
V	Volume (m^3)
x	Solution liquid ammonia concentration (kg kg^{-1})
y	Solution vapor ammonia concentration (kg kg^{-1})
Y	State vector
z	Axial coordinate (m)

Subscripts

acc	Accumulator
cf	Coupling fluid
conv	Convective heat transfer
cs	Cross section
end	End of ramping period
f	Working fluid – liquid on tray
final	Final value
flux	Heat transfer flux
i	Node center of CV
in	Inlet
j	Boundary of CV
L	Working fluid - liquid
out	Outlet
seg	Segment
set	Desorber plate and coupling fluid shims set
start	Start of ramping period
store	Energy storage
tray	Desorber tray
V	Working fluid - vapor
w	Heat exchanger wall
0	Initial condition

PART II

Variables

a	General constant coefficient
A	Area (m^2)
c	Specific heat capacity ($J\ kg^{-1}\ K^{-1}$)
C	Heat capacity ($J\ K^{-1}$)
COP	Coefficient of performance (-)
d	Disturbances vector
dt	Time step (s)
f	System dynamics function
h	Specific enthalpy ($J\ kg^{-1}$) & algebraic variables function
J	Cost function
k	Runge-Kutta slope variable
$\dot{m}$	Mass flow rate ($kg\ s^{-1}$)
n	Number (-)
N	Control interval count (-)
p	Pressure (Pa)
P	Power (W)
$\dot{q}$	Specific heat flux ($W\ m^{-2}$)
$\dot{Q}$	Heat flux (W)

R	Relative humidity (-)
S	Penalty coefficient (W K^{-2})
t	Time (s)
T	Temperature (K)
u	Input vector
U	Overall heat transfer coefficient (W m^{-2} K^{-1})
V	Volume (m^{-3})
$\dot{W}$	Work (W)
x	Concentration (kg kg^{-1}) & State vector
z	Component variables vector

Greek

α	Convective heat transfer coefficient (W m^{-2} K^{-1})
δ	Recirculation flap position (-)
ρ	Density (kg m^{-3})
τ	Transmissivity (-)

Superscripts

a	Air
CO2	Carbon-dioxide
H2O	Water
i	Interior
in	Inlet
out	Outlet

Subscripts

amb	Ambient
bl	Blower
bod	Body, vehicle
c	Comfort
cab	Cabin
comp	Compressor, AC system
crit	Critical value
end	End or final value
evap	Evaporator, AC system
FB	Feedback
goal	Goal, target value
max	Maximum value
min	Minimum value
pas	Passenger
RC	Recirculation
sun	Sun
Tc	Cabin temperature
u	Usable
0	Initial state

Acronyms

AC	Air conditioning
CFD	Computational fluid dynamics
CO_2	Carbon-dioxide
COP	Coefficient of performance
DAE	Differential algebraic equation
EV	Electric vehicle
H_2O	Water
HVAC	Heating, ventilation, and air conditioning
ICEV	Internal combustion engine vehicle
MPC	Model predictive controller
OCP	Optimal control problem
OSHA	Occupational Safety and Health Administration
PD	Proportional-derivative
PID	Proportional-integral-derivative

SUMMARY

Part one of the thesis presents a mathematical framework to simulate the transient response of a desorber for small-capacity ammonia-water absorption heat pumps. The model is based on dynamic analysis of conservation equations and accounts for the thermal capacitances in the heat exchanger wall material and fluid volumes. The numerical solver and its implementation are presented. Improved computational performance is achieved by using advanced solvers for stiff differential-algebraic equations. The model is utilized to predict desorber performance at steady-state conditions and to simulate the transient response of the component to ramping or perturbation of input parameters from steady state. It can also be used to develop reduced-order models suitable for the design of control strategies to optimize system performance.

Part two of the thesis presents an optimal control scheme for an electric vehicle cabin air conditioning system. The energy efficient control of a vehicle's air conditioning (AC) system is of great importance in any modern automobile. However, the goal of maximizing the driving range of battery electric vehicles has increased the interest in sophisticated control strategies. This work presents a control scheme for the air conditioning system of an electric vehicle based on non-linear, constrained optimal control theory with the simultaneous goals of reducing the energy consumption of the AC system and meeting the passengers' required cabin conditions. Cabin and air system models are derived to define the dynamics of the thermal system. Different formulations of the cabin outlet air temperature available in the literature are explored. From these models, an optimal control problem (OCP) is formulated, with system constraints explicitly considered. The OCP is transformed into a non-linear program using the direct multiple shooting strategy and fourth-order Runge-Kutta method. The open-source IPOPT solver is applied, with the required derivatives provided by the CasADi toolkit. The effectiveness of the proposed optimal control

scheme in reducing the energy consumption of the electric vehicle AC system is compared to a simple feedback controller using scenarios with constant and time-varying disturbances

PART I

Transient Simulation of Ammonia-Water Mixture Desorption for Absorption Heat Pumps

1. INTRODUCTION

There is renewed interest in absorption heat pumps due to the global efforts to reduce the use of fossil-based electrically driven vapor compression systems. Absorption systems are thermally-driven and use natural refrigerants, which could lead to primary energy savings and a lower global warming potential (GWP), especially when the system is coupled with non-fossil fuel driven processes (Srikhirin *et al.*, 2001).

Vapor absorption systems are similar to vapor compression systems in that they employ a condenser, evaporator, and an expansion valve to satisfy a given cooling or heating load. The main difference in the design of the two systems lies in a thermal compressor comprising an absorber, desorber, dilute solution expansion valve, solution pump, and a solution heat exchanger replacing the mechanical compressor. Vapor absorption systems have typically been used in large commercial applications due to their larger size, increased system complexity, and higher installation cost compared to vapor compression systems. However, recent research has demonstrated the viability of small-scale absorption chillers with cooling capacities to meet residential and light-commercial applications (Determan and Garimella, 2012; Garrabrant *et al.*, 2013; Garimella *et al.*, 2016). These small-capacity systems operate under frequent load transients and larger variations in operating conditions, such as changes in the ambient temperature. These variations in operating conditions can cause the system performance to degrade. Therefore, a control system is required to maintain optimal performance of the system for a range of operating conditions. The control system design needs a transient model of the system that can predict the time response of the system to changes in operating conditions and tunable input parameters. Several researchers have investigated the transient response and dynamics of vapor absorption systems, using both numerical simulations and experiments (Jeong *et al.*, 1998; Kim and Park,

2007; Kohlenbach and Ziegler, 2008; Zinet *et al.*, 2012; Viswanathan *et al.*, 2013). These studies demonstrated simulation paradigms ranging from simplified lumped-parameter approaches to detailed discretized models. The heat and mass exchangers employed in an absorption system can be broadly classified into two categories. The first category includes single-inlet single-outlet components such as the evaporator, condenser, absorber, and recuperative heat exchangers. The second category includes single-inlet multiple-outlet heat and mass exchangers such as the desorber and rectifier, or multiple-inlet, single-outlet components such as the absorber. Details of the modeling process for single-inlet single-outlet components are provided by (Goyal *et al.*, 2017). The modeling of the absorber and desorber has received more attention than other heat and mass exchangers in absorption systems. This is due to more complex geometries and coupled two-phase heat and mass transfer processes in these components.

Several studies have demonstrated miniaturization of absorption systems for small-capacity residential systems. Particular emphasis is on desorber designs to ensure the most efficient refrigerant generation and stable operation of the overall system (Determan and Garimella, 2011; Delahanty *et al.*, 2015; Garimella *et al.*, 2016). These designs also ensure small fluid inventories that minimize the thermal capacitance. One of these designs, a branched-tray desorber presented by Delahanty *et al.* (2015), demonstrates features analogous to distillation columns used in chemical separation processes such as pool-boiling in trays and stage-wise purification of the generated vapor. It should be noted that distillation columns differ markedly from the desorber column as they are typically not heat assisted along the length of the column. However, the conservation equations and tray inefficiency formulation are found to be analogous to those employed for the desorber. Comprehensive reviews of transient models for distillation columns are available in the literature (Gani *et al.*, 1986; Luyben, 1989; Skogestad, 1997; Bequette, 1998).

The primary focus of this work is to develop a detailed first principles-based transient model of the desorber in absorption systems. This will lead to generalization of numerical models for the design and analysis of control algorithms for absorption systems. The state of the art can benefit significantly from a generalized modeling paradigm to further advance the analysis of absorption systems. The thesis is organized as follows: Chapter 2 presents the assumptions and equations used in the development of the mathematical model along with the heat exchanger parameters; Chapter 3 discusses the features of the numerical solver and its implementation; Chapter 4 presents different case studies involving varying input parameters of the desorber, both for comparison of steady-state response and analysis of transient performance; finally, Chapter 5 concludes the present work and provides recommendations for future development.

2. MATHEMATICAL MODELING

The desorber is the main refrigerant generating component in a vapor absorption system. Figure 1 shows a schematic of a branched-tray desorber. This geometry is the focus of this work as it can be utilized in a compact small-capacity absorption chiller as demonstrated by Garimella *et al.* (2016). In this configuration, the concentrated solution (rich in ammonia) is received from the solution heat exchanger and flows downward through the desorber. At each tray, the liquid solution exchanges heat through the desorber wall and the coupling fluid flowing in a counter-flow configuration. Vapor is predominantly generated by pool boiling at each tray, rising counter-current to the liquid solution flow due to buoyancy, and exits at the top of the desorber. The dilute solution (poor in ammonia concentration) exits at the bottom of the desorber, returning to the

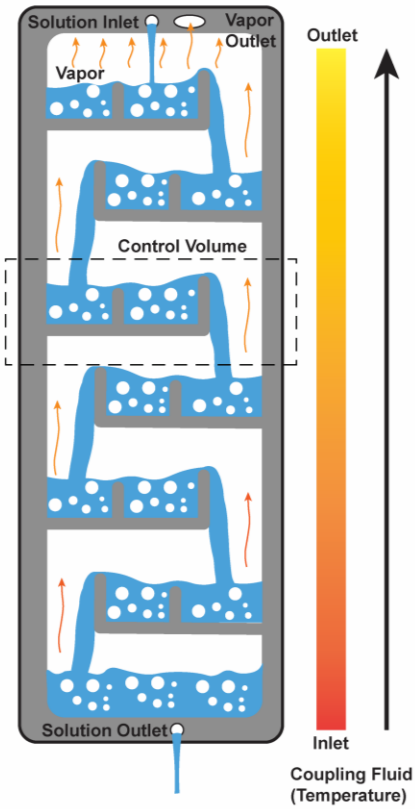

Figure 1: Schematic of the branched tray desorber.

solution heat exchanger. Finally, the dilute solution and refrigerant vapor mix in the absorber, regenerating the concentrated solution.

This chapter presents the mathematical equations to formulate the transient model of the desorber. The conservation equations with simplifying assumptions pertinent to the component geometry and operating conditions are explained. Finally, the form of equations suitable for a differential equation solver are presented.

2.1 Governing equations

All fluids within a vapor absorption system are assumed Newtonian and, thus, are governed by the three conservation equations for mass, momentum, and energy:

$$\frac{\partial \rho}{\partial t} + \nabla \cdot (\rho u) = 0 \tag{1}$$

$$\frac{\partial \rho u}{\partial t} + \nabla \cdot (\rho u u) = \rho f_b + \nabla \cdot \sigma \tag{2}$$

$$\frac{\partial \rho \left[e + \frac{u \cdot u}{2} \right]}{\partial t} + \nabla \cdot \rho u \left(h + \frac{u \cdot u}{2} \right) = -\nabla \cdot q'' + \rho f_b \cdot u + \nabla \cdot (\tau \cdot u) + \dot{Q} \tag{3}$$

Equations 1 – 3 are simplified using assumptions based on experimental observations and practical considerations, as discussed below.

- 1-D compressible flow of two-phase ammonia-water working fluid is assumed.
- Body forces and viscous forces are neglected.
- Pressure on the solution-side of the component may vary with time, but is assumed spatially constant as the pressure wave is assumed to propagate much faster than thermal and mass storage effects.

- Pressure drop in the component is neglected as it is a small fraction of the operating pressure. This allows for the omission of the momentum equation from the final set of equations.
- Axial conduction effects are neglected as the Peclet (*Pe*) number is typically large
- Homogenous flow of the liquid and vapor phases is assumed.
- Constant cross-sectional area of flow and wall is assumed.
- Uniform heat transfer coefficient is assumed for both fluids.
- Axial conduction in the component wall is neglected.
- 1-D incompressible flow of coupling fluid is assumed. Pressure drop, viscous dissipation, and axial conduction effects are neglected. The coupling fluid is in counter-flow with the solution flow.

Applying these assumptions, the governing conservation equations can be simplified to remove second-order derivatives and the coupling between pressure and velocity terms. The simplified solution mass and energy conservation equations become:

$$\frac{\partial \rho_f}{\partial t} + \frac{\partial \rho_f u_f}{\partial z} = 0 \tag{4}$$

$$\frac{\partial \left(\rho_f h_f - P_f \right)}{\partial t} + \frac{\partial \left(\rho_f u_f h_f \right)}{\partial z} - \frac{U_f Per_f \left(T_w - T_f \right)}{A_{cs}} = 0 \tag{5}$$

These equations form a system of partial differential equations with solution enthalpy and velocity as the state variables. The equations require initial conditions and the definition of time-dependent boundary conditions. The inlet and outlet boundary conditions are established by the components up- and down-stream, respectively. As ammonia-water is a binary mixture, an additional species conservation equation is added to track species storage and transport.

$$\frac{\partial \rho_f x_f}{\partial t} + \frac{\partial (\rho_f u_f x_f)}{\partial z} = 0 \tag{6}$$

The above equations are converted to their mass flow forms by multiplying by the cross-sectional area of the flow. The state variables then become solution mass flow rate, concentration, and enthalpy:

$$\frac{\partial A_{cs} \rho_f}{\partial t} + \frac{\partial \dot{m}_f}{\partial z} = 0 \tag{7}$$

$$\frac{\partial A_{cs} \rho_f x_f}{\partial t} + \frac{\partial \dot{m}_f x_f}{\partial z} = 0 \tag{8}$$

$$\frac{\partial A_{cs} [\rho_f h_f - P_f]}{\partial t} + \frac{\partial \dot{m}_f h_f}{\partial z} - U_f Per_f (T_w - T_f) = 0 \tag{9}$$

The wall energy and incompressible coupling fluid energy conservation equations take the form:

$$\rho_w Cp_w A_{cs,w} \frac{\partial T_w}{\partial t} + U_f Per_f (T_w - T_f) - U_{cf} Per_{cf} (T_{cf} - T_w) = 0 \tag{10}$$

$$\rho_{cf} Cp_{cf} A_{cs,cf} \frac{\partial T_{cf}}{\partial t} + \frac{\partial (\dot{m}_{cf} Cp_{cf} T_{cf})}{\partial z} + U_{cf} Per_{cf} (T_{cf} - T_w) = 0 \tag{11}$$

In addition to the assumptions listed above, the key assumptions applied to the desorber component of a small-scale ammonia-water absorption system to further simplify the system of equations are as follows:

- The solution vapor and liquid are in counter-flow.
- The liquid and vapor phases throughout the component are at saturated thermodynamic states as the desorber is continuously heated along the length and vapor and liquid phases exist at each location.

- Heat transfer between the component wall and vapor is neglected as the convective heat transfer coefficient for vapor flow is significantly smaller than the boiling heat transfer coefficient.
- Phase equilibrium is approximated using thermal equilibrium between the liquid and vapor phases. It is assumed here that the interaction between the two phases is primarily driven by thermal inequilibrium with chemical interactions having a small effect.
- Vapor holdup is neglected in all control volumes. Although the volume occupied by the vapor is large, the liquid density is much higher than that of the vapor, and therefore, the mass of each control volume can be assumed to be liquid-only.
- The liquid on all trays is assumed perfectly mixed and incompressible. Therefore, the liquid solution exiting the trays is assumed to be at the tray temperature and concentration.
- All trays are assumed inefficient, requiring the inclusion of a tray efficiency equation. A vapor-phase tray efficiency expression is used with the efficiency values for each tray selected based upon experimentally observed steady-state vapor outlet temperatures and concentrations (Delahanty *et al.*, 2015).

$$\varepsilon_{V_i} = \frac{y_j - y_{j-1}}{y_j^* - y_{j-1}} \tag{12}$$

The term y_j^* is the concentration of vapor exiting the tray if it was in thermal equilibrium with the liquid on the tray.

These assumptions do not change the governing differential equations 7 – 11 when applied to the desorber. However, the discretized governing equations for the desorber are modified, as presented in the following section.

2.2 Discretized equations

Figure 2 shows the discretized counter-flow desorber. The control volumes (CV) are chosen such that one boiling tray is centered in each segment. Equations 7 – 11 are integrated over each CV and discretized using an upwinding differencing scheme (UDS) (Patankar, 1980) for liquid flux terms to formulate a system of ordinary differential equations (ODEs) for all nodes. Vapor flux terms are not discretized using UDS because the vapor exiting each CV is not at the tray temperature due to tray inefficiencies. These ODEs are solved simultaneously to obtain the transient response of the desorber.

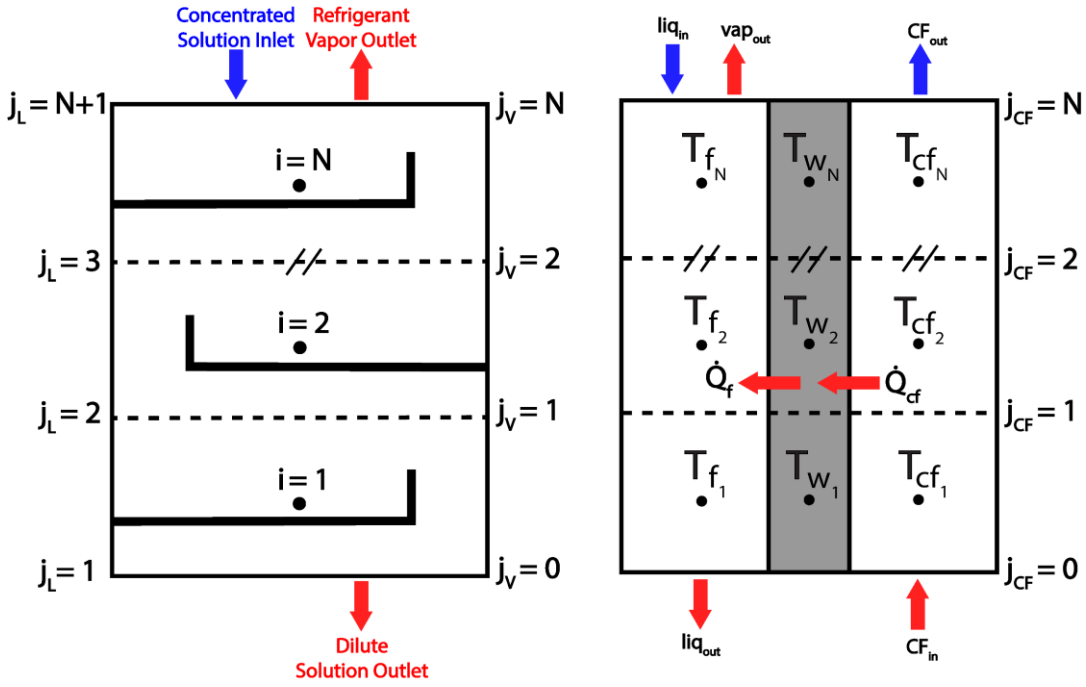

Figure 2: Discretized desorber component; Left: solution-side discretization; Right: solution, wall, and coupling fluid region discretization.

Figure 3 shows an individual tray with solution-side CV. Liquid solution and vapor enter the CV from the trays above and below, respectively. The outlet vapor state is defined according to the tray efficiency definition (Equation 12), which provides the thermal non-equilibrium vapor concentration, the component pressure (known boundary condition), and the saturated vapor quality (q = 1). Outlet vapor enthalpy, temperature, and other thermodynamic properties can be determined using this triplet.

The discretized equations for mass, species, and energy conservation for the solution, wall, and coupling fluid are:

$$\left(\frac{\partial \rho_{f,i}}{\partial P_f}\right)\frac{dP_f}{dt}+\left(\frac{\partial \rho_{f,i}}{\partial x_i}\right)\frac{dx_i}{dt}+\left(\frac{\partial \rho_{f,i}}{\partial h_{f,i}}\right)\frac{dh_{f,i}}{dt_i}=\frac{1}{V_{f,seg}}\left[\dot{m}_{L,j+1}-\dot{m}_{L,j}+\dot{m}_{V,j-1}-\dot{m}_{V,j}\right] \qquad (13)$$

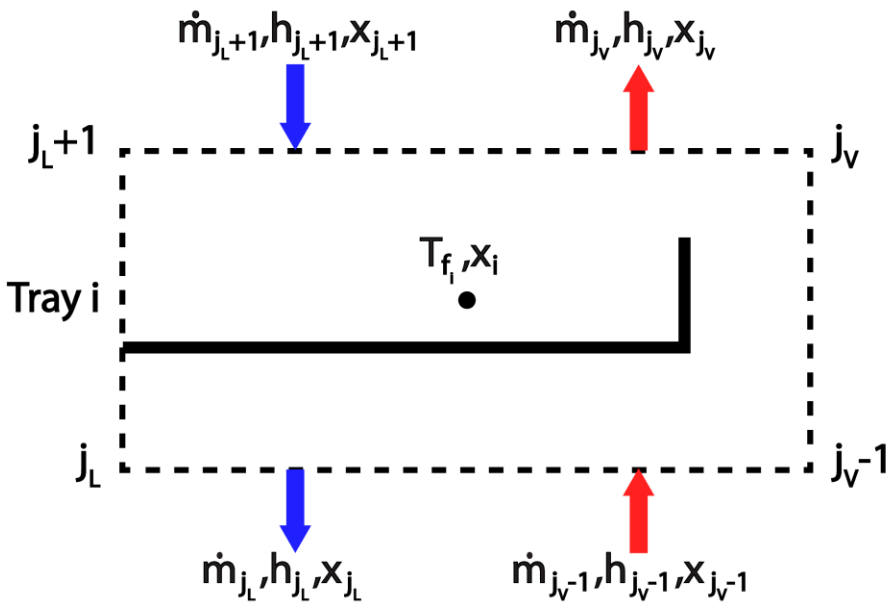

Figure 3: Solution-side tray control volume.

$$\left(x_i \frac{\partial \rho_{f,i}}{\partial P_f}\right)\frac{dP_f}{dt}+\left(\rho_{f,i}+x_i \frac{\partial \rho_{f,i}}{\partial x_i}\right)\frac{dx_{f,i}}{dt}+\left(x_i \frac{\partial \rho_{f,i}}{\partial h_{f,i}}\right)\frac{dh_{f,i}}{dt}= \frac{1}{V_{f,seg}}\left[\dot{m}_{L,j+1}x_{j+1}-\dot{m}_{L,j}x_j+\dot{m}_{V,j-1}y_{j-1}-\dot{m}_{V,j}y_j\right] \tag{14}$$

$$\left(\frac{\partial \rho_{f,i}}{\partial P_f}-\frac{1}{V_{f,seg}}\right)\frac{dP_f}{dt}+\left(\frac{\partial \rho_{f,i}}{\partial x_i}\right)\frac{dx_i}{dt}+\left(\frac{\partial \rho_{f,i}}{\partial h_{f,i}}h_{f,i}+\rho_{f,i}\right)\frac{dh_{f,i}}{dt}= \frac{1}{V_{f,seg}}\left[\dot{m}_{L,j+1}h_{L,j+1}-\dot{m}_{L,j}h_{L,j}+\dot{m}_{V,j-1}h_{V,j-1}-\dot{m}_{V,j}h_{V,j}+(UA)_f\left(T_{w,i}-T_{f,i}\right)\right] \tag{15}$$

$$(m_w Cp_w)_i \frac{dT_{w,i}}{dt}=(UA)_{cf}\left(T_{cf,i}-T_{w,i}\right)-(UA)_f\left(T_{w,i}-T_{f,i}\right) \tag{16}$$

$$(m_{cf} Cp_{cf})_i \frac{dT_{cf,i}}{dt}=\dot{m}_{cf} Cp_{cf}\left(T_{cf,j-1}-T_{cf,j}\right)-(UA)_{cf}\left(T_{cf,i}-T_{w,i}\right) \tag{17}$$

$$y_j = y_{j-1}+E_{V_i}\left(y_j^*-y_{j-1}\right) \tag{18}$$

$$y_j^* = F\left(T_{f,i}, P_f, q=1\right) \tag{19}$$

$$x_{f,i} = F\left(T_{f,i}, P_f, q=0\right) \tag{20}$$

$$h_{L,j} = h_{f,i} \tag{21}$$

$$x_j = x_{f,i} \tag{22}$$

$$T_{cf,j} = T_{cf,i} \tag{23}$$

Equations 12 – 20 along with Equations 21 – 23 (UDS) are formulated for all *N* trays (CVs or nodes), which results in a system of 8*N* equations with 8*N* unknowns: nodal liquid enthalpy and concentration, ideal outlet vapor concentration, actual outlet vapor concentration, nodal wall and coupling fluid temperature, and outlet liquid and vapor mass flow rates. Equations 12 – 20 form a system of differential-algebraic equations (DAEs).

2.3 Geometric and heat transfer parameters

The geometric and heat transfer parameters used in this study are representative of the desorber-rectifier components developed by Keinath *et al.* (2015) and Delahanty *et al.* (2015). The compact ammonia-water desorber-rectifier developed by Keinath *et al.* (2015) is shown in Figure 4. The solution plate of the component (left) consists of three sections: the desorber, analyzer, and rectifier. Each solution plate has two coupling fluid sheets (right) attached to it. The focus of this study is on the desorber section of the complete desorber-rectifier component. Any dynamic effects of the analyzer are neglected and the rectifier is not simulated. However, the methods presented in this study can be adapted to include these sections.

Table 1 provides a summary of the key parameters of the desorber. All parameters are for a single solution plate and coupling fluid sheet set. The number of trays is based upon the geometry shown in Figure 4. The two tray channels are assumed to be lumped into one solution channel with

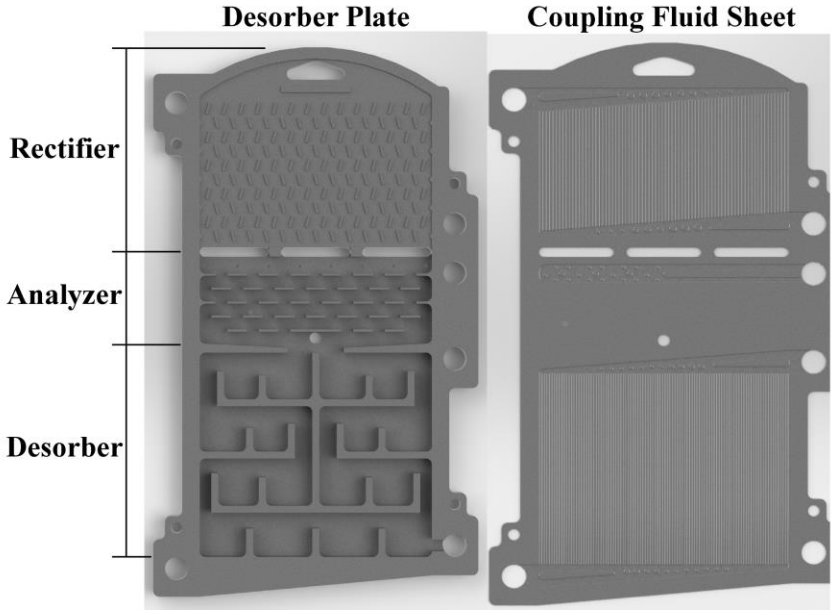

Figure 4: Complete desorber solution plate (left) and coupling fluid sheet (right) pair (Keinath *et al.*, 2015).

Table 1: Properties of desorber per solution plate and coupling fluid sheet pair.

	Description	Units	Nomenclature	Value
Component	Number of plate/sheet sets	-	N_{set}	8
NH_3-H_2O solution	Number of trays	-	N_{tray}	4
	Fluid region volume	m^3	V_f	7×10^{-5}
	Heat transfer conductance	$W\ K^{-1}$	$(UA)_f$	67.5
Wall	Mass of wall	kg	m_w	6.37
	Specific heat	$J\ kg^{-1}\ K^{-1}$	Cp_w	480
CF	Density	$kg\ m^{-1}$	ρ_{cf}	789
	Fluid region volume	m^3	V_{cf}	3.18×10^{-6}
	Mass of fluid	kg	m_{cf}	2.51×10^{-3}
	Specific heat	$J\ kg^{-1}\ K^{-1}$	Cp_{cf}	2690
	Overall conductance	$W\ K^{-1}$	$(UA)_{cf}$	26.625

enlarged trays. The solution fluid region volume is approximated by the overall desorber region volume minus the volume of the tray material. The solution heat transfer conductance is representative of the results of Delahanty *et al.* (2015), which take into account heat loss to the surroundings. Due to the relatively large uncertainties in the experimental values, the present study assumes a uniform average value for the solution heat transfer conductance. The wall mass is approximated as the mass of the desorber section of one solution tray and two coupling fluid sheets, calculated using engineering drawings of the sections made of AISI 304 steel. The specific heat capacity of the wall material is also representative of AISI 304 steel.

The coupling fluid for the desorber is heated Paratherm NF^{TM}, a mineral-oil heat transfer fluid. Specific heat capacity and density values for the coupling fluid were obtained from the manufacturer. Thermal properties were calculated at an average coupling fluid temperature of 165°C. The coupling fluid region volume is calculated using the number of coupling fluid channels (102), channel length (0.101 m), and channel hydraulic diameter (442×10^{-6} m). This fluid region volume is then doubled to account for the fact that two coupling fluid sheets are attached to each solution plate. The coupling fluid heat transfer conductance is also representative of the desorber investigated by Delahanty *et al.* (2015).

3. SOLVER IMPLEMENTATION

This section discusses the implementation of initial and boundary conditions and the algorithm for the DAE solver.

3.1 Boundary and initial conditions

The only inlet into the desorber is the concentrated solution assumed to be entering in a saturated liquid phase. It is assumed that no vapor flows into the desorber. In a complete vapor absorption system, the state of the inlet solution would be determined by the solution heat exchanger outlet located upstream of the desorber. In the present study, the inlet state is set using the knowledge of steady-state operating conditions specified by a steady-state cycle model.

There are two cases of initial conditions:

- all regions at the same temperature, constant liquid mass flow rate, and no vapor flow, or
- final profile for a previous simulation as the initial condition for a new trial.

The first case is applied to a startup simulation to bring the desorber model to the design steady-state. The second case is used in subsequent studies where the transient response of the desorber to perturbation in the input parameters from the design steady-state is of interest.

3.1.1. Input parameter ramping function

During the simulations, the time-dependent boundary conditions must be changed in a smooth and well-defined manner to ensure solver stability. These parameter values are ramped using a logistic function. The logistic function is a sigmoid-shaped curve defined as:

$$S(t) = S_0 + \frac{S_{final} - S_0}{1 + \exp[-\kappa(t - t_0)]} \tag{24}$$

where:

- S_0 = the initial value of the function
- S_{final} = the final value of the function
- κ = the steepness of the curve defined by:

$$\kappa = \frac{10}{t_{end} - t_{start}} \tag{25}$$

  where t_{start} is the time the function starts ramping and t_{end} is the time that the function reaches the final value. The numerator is chosen through trial and error to ensure that a major portion of the ramping is completed in the defined time range.

- t = time in seconds
- t_0 = the x-value of the midpoint of the sigmoid curve defined by:

$$\frac{t_{start} + t_{end}}{2} \tag{26}$$

An example of a logistic ramping profile is shown in Figure 5. The function is ramped from 0.2 to 0.8 from t = 15 to t = 45 s. The function value is shown as a solid line and its derivative is shown as a dashed line. The function remains at its initial value until the ramping start time, where it ramps with an approximately exponential profile. As the function reaches saturation, its growth slows until it reaches its final value at the end of the defined time range. The logistic function is chosen over a simple piece-wise step-change or cubic-spline functions because it is continuously differentiable and smoothly defined. These characteristics are key for the stability of the MATLAB® solver described in the following section.

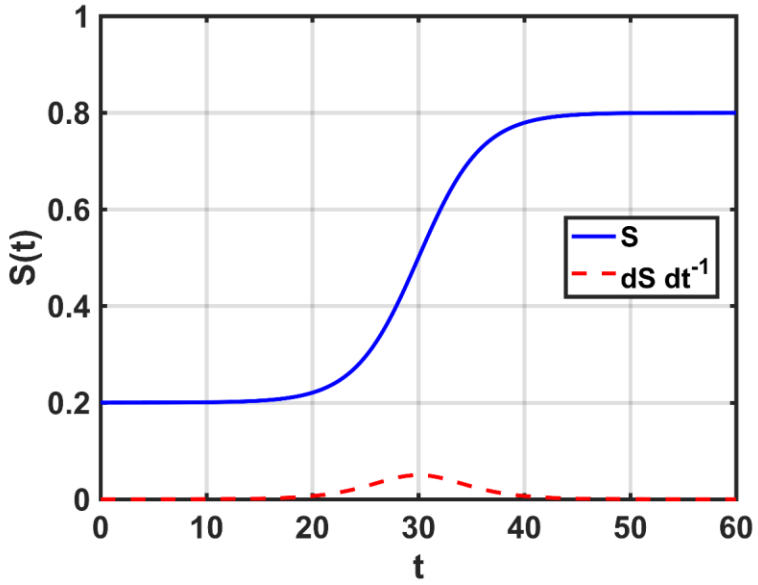

Figure 5: Sigmoid ramping from 0.2 to 0.8 over 30 seconds.

3.2 DAE solver

The built-in, variable time-step, implicit solver *ode15s* in MATLAB® (Mathworks, 2016) is chosen to solve the system of equations for the desorber transient model. The solver is designed to solve systems of stiff differential equations and DAEs, making it a good choice for the present system. The dynamic system of equations is defined in matrix form by:

$$M(t,Y)\cdot\dot{Y}(t)=G(t,Y) \tag{27}$$

Here, *M(t,Y)* is the mass matrix of the system, $\dot{Y}(t)$ is a vector of the time derivatives of the state variables, and *G(t,Y)* is a vector of the non-derivative terms of the system of equations. The solver integrates the system of equations over a given time range with specified initial and boundary conditions. During the simulation, if the solver encounters a period of sharp gradients in state variables, it adjusts the time step accordingly until the tolerance criterion is achieved for the solution. A set of options can also be provided to the solver routine to define, among others,

the mass matrix, the Jacobian of the system, Jacobian sparsity, maximum differentiation order of the solver, maximum allowable solver time step, initial slope of the state variables, and the relative tolerance for each time step. Shampine and Reichelt (1997) provide a comprehensive tutorial on the MATLAB® ODE solver suite.

A flowchart of the solver used in this study is shown in Figure 6. At the start of a simulation, constant geometric and simulation parameters such as fluid region volumes and heat transfer areas, heat transfer coefficients, desorber geometry, specific heats, mass of the wall, number of nodes, tray efficiencies, and tolerance to convergence are set. The initial values of the state variables and the time-varying profiles of the boundary conditions are then provided. Next, the equations to be solved are defined and the mass matrix is assembled. The ODE solver is called at this point with the input of the simulation options, initial conditions, time range, and functions to be solved. Internal to the solver, at each time step, the state derivative vector is evaluated as well as any algebraic equations. The solution is checked for convergence and if it has converged, the state derivative vector is integrated in time, and the state vector and the boundary conditions are updated. If convergence is not achieved, the time step is adjusted until the solution converges. These steps are repeated until the solver reaches the end of the simulation time. All the variables are then saved for post-processing.

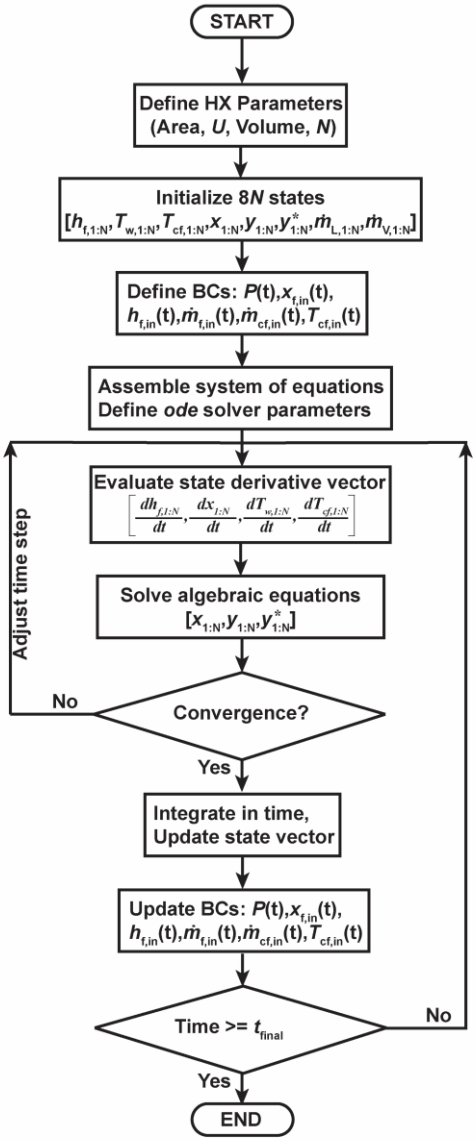

Figure 6: MATLAB® ODE solver flowchart.

4. RESULTS AND DISCUSSION

The results of the transient model of an ammonia-water desorber using the finite volume method described above are described here. First, the general parameters for the simulations are outlined. Second, the steady-state performance of the dynamic model is compared with experimental and simulation data available in the literature. Third, the dynamic model is used to simulate the start-up of the ammonia-water desorber from ambient conditions. Lastly, the transient response of the desorber to changes in component inputs (e.g., coupling fluid inlet temperature, solution inlet mass flow rate, ambient conditions) is analyzed.

4.1 Simulation parameters

For each test case simulation, the solver and simulation parameters must be set. These values include the maximum time step the solver may take (*MaxStep*), the relative error tolerance to determine convergence (*RelTol*), the differential changes in pressure, concentrations, and enthalpy for use in the density time derivative approximation (ΔP_f, Δx_f, Δh_f), and finally, the tray efficiencies (E_{V_i}). The values of these parameters for all cases, unless otherwise noted, are provided in Table 2.

The maximum time step size for the ODE solver is set to 0.5 seconds. This aids solver stability by ensuring that the solver does not take large time steps over periods of large-amplitude gradients by increasing the time step size prematurely. Although the variable-time step MATLAB® solver automatically adjusts the time-step, the step was limited due to the highly non-linear nature of the ammonia-water property routines around saturation. Additionally, the relative error tolerance is set to 1×10^{-6} to ensure high accuracy of the solved variables. The maximum order of

Table 2: General simulation parameter values.

Parameter	Value (Units)
MaxStep	0.5 (s)
RelTol	1×10^{-6}
MaxOrder	2
ΔP_f	10 (Pa)
Δx_f	0.000001 (kg kg^{-1})
Δh_f	0.1 (J kg^{-1})
ε_{V_i}	1.0 (bottom), 0.87, 0.73, 0.6 (top)

the numerical differencing formulas (NDFs) internal to the MATLAB® solver, *MaxOrder*, is maintained at '2'. Second-order NDFs are used in this work to provide reasonable accuracy and computational efficiency. The ODE solver options and their usage are discussed in more detail in the MATLAB® documentation (Mathworks, 2016).

The differential changes in pressure, concentration, and enthalpy are used in the density partial derivative approximations, which are in turn used in the solution-side energy, mass, and species continuity equations (Equations 13-15). The differential changes are set such that any changes around the current state point are captured and are orders of magnitude smaller than their corresponding state variable values.

Finally, the tray efficiencies are set assuming a spatially linear variation in the efficiency starting from the bottom tray ($i = 1$) and moving up the desorber. The top tray ($i = N$) efficiency is chosen to be 0.6 through trial and error to achieve outlet vapor concentration and temperature at

design conditions comparable to those demonstrated by Delahanty *et al.* (2015) and Keinath *et al.* (2015).

4.2 Steady-state performance

The results of the dynamic model developed in this study were compared with those from an experimental study (Delahanty, 2015) of the desorber geometry mentioned in Chapter 2. First, a comparison of the spatial variation of solution vapor, solution liquid, and coupling fluid temperatures in the desorber at steady-state operation and change in heat transfer rate with varying solution inlet flow rate are compared with those presented by Delahanty (2015) in Table 3. The solution inlet temperature, pressure, solution inlet mass flow rate, and coupling fluid mass flow rate are identical for both studies. The variation in inlet concentration between the numerical study of the present work and the experimental study is due to the solution entering the experimental test section in a subcooled state, whereas the present model assumes a saturated liquid inlet. It was,

Table 3: Comparison of dynamic model and Delahanty (2015) component inputs.

Parameter	Dynamic Model	Delahanty (2015)	Percentage Deviation
Solution inlet temperature (°C)	82.8	82.8	-
Pressure (kPa)	1626	1626	-
Solution inlet vapor quality (-)	0	*Subcooled*	-
Solution inlet concentration (kg kg^{-1})	0.5235	0.479	9.29
Solution mass flow rate (kg s^{-1})	0.0009	0.0009	-
Coupling fluid inlet temperature (°C)	180	179.5	0.279
Coupling fluid mass flow rate (kg s^{-1})	0.00765	0.00765	-

however, determined that for temperature and heat transfer rate comparison purposes, matching the solution inlet temperature was more important.

A comparison of the spatial variation of fluid temperatures within one set of passages of the desorber is presented in Figure 7. In the plot, the top of the desorber, where the concentrated solution enters the component and refrigerant vapor exits, is denoted with normalized location '1'. The coupling fluid enters the desorber and the dilute solution exits at location '0'. For the present study, liquid temperatures are computed at the center of the control volumes. The vapor temperatures are only calculated at the control volume boundaries due to thermal inequilibrium with the liquid on each tray. The dynamic model compares well with the experimental results. Outlet temperatures for all three fluid streams (dilute solution, refrigerant vapor and coupling fluid) are in close agreement. The discrepancies in the trends of the refrigerant vapor and liquid

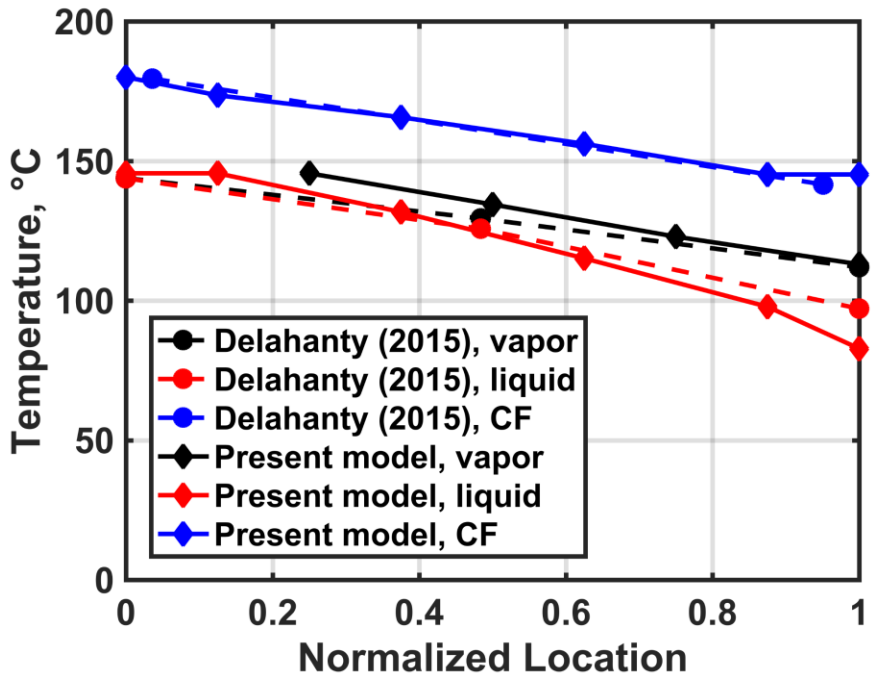

Figure 7: Comparison of the spatial variation of refrigerant vapor, dilute solution, and coupling fluid temperatures in the desorber at steady-state.

temperatures are due to the assumptions made in temperatures from the upwinding differencing scheme and the saturated inlet quality assumption of the present model.

The effect of solution inlet flow rate on heat transfer rate is compared in Figure 8 for the present model, the steady-state system model of Garimella *et al.* (2016) developed using the Engineering Equation Solver (EES) platform, and the experimental results of Delahanty (2015). As mentioned previously, the desorber is made of eight solution plate and coupling fluid sheets sets. Delahanty (2015) tested the heat transfer performance of one of these pairs. The experimental heat transfer data taken from Figure 4.6 of Delahanty (2015) used in Figure 8 are for the coupling fluid heat duty. For the model developed in the present study, the heat loss rate is assumed to be zero. As shown in the figure, the predictions of the two numerical models compare well with experimental data at design, as well as at off-design operating conditions. The desorber heat duty

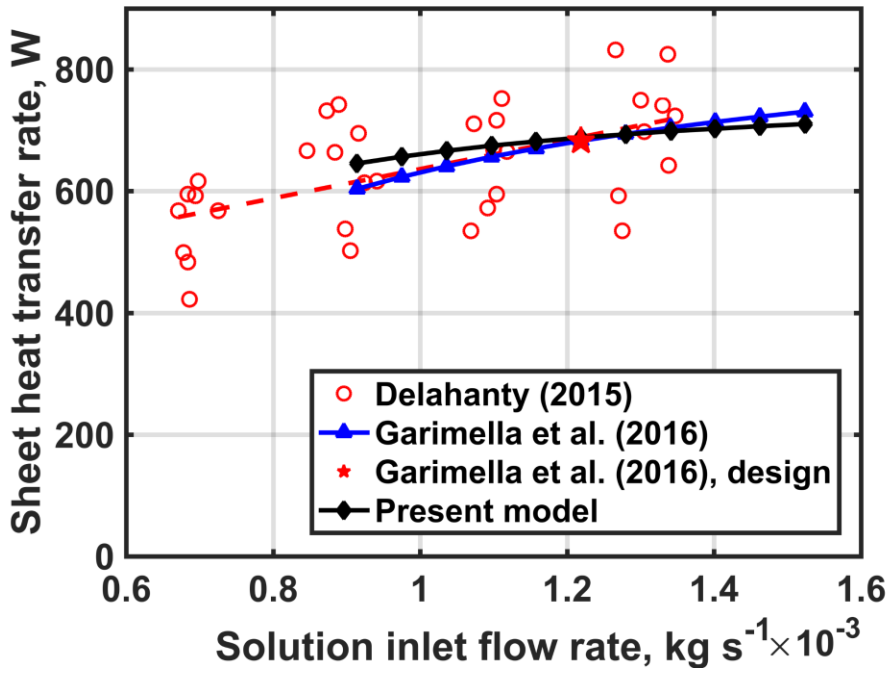

Figure 8: Comparison of sheet heat transfer as a function of solution inlet mass flow rate.

increases with solution inlet flow rate. Both models maintain constant heat transfer conductance values. Therefore, the key parameter governing the heat transfer rate is the driving temperature difference. The coupling fluid inlet conditions remain unchanged, but the solution inlet temperature changes due to variations in pressure and concentration. The additional mass flow rate leads to the corresponding variation in the heat transfer rate. The difference in the slope of the heat duty profiles is attributed to the difference in the inlet quality for the two models and assumption of constant temperature inequilibrium between exiting vapor and entering solution in the EES system model. The saturated liquid inlet assumption causes the present model to predict a higher heat transfer rate at solution flow rates below design due to a larger temperature difference between the solution and coupling fluid sides. Above the design solution flow rate, the EES system model predicts higher heat transfer rate as compared to the present study, because the constraint on the vapor-liquid inequilibrium temperature causes the exiting vapor enthalpy to be significantly lower than that predicted by the present model. Overall, the solution mass flow rate is observed to have a significant effect on the performance of the desorber. This knowledge may be used later by utilizing the solution mass flow rate as a key process variable.

The discussion on steady-state performance of the present model shows that the dynamic model of the desorber developed in this work performs well when compared with other numerical models, as well as experimental results. The following sections present the dynamic performance of the present model.

4.3 Start-up performance

This section presents the transient behavior of the ammonia-water desorber during start-up. The initial and final conditions for the start-up cases are provided in Table 4.

Table 4: Initial and final conditions for start-up cases.

Constant Parameters	Value	
Solution inlet flow rate (kg s^{-1})	0.00975	
Coupling fluid flow rate (kg s^{-1})	0.084	
Solution inlet vapor quality (-)	0	
Ramped Parameters	**Initial**	**Final**
Solution inlet temperature (°C)	25	102.5
Pressure (kPa)	400	2087
Solution inlet concentration (kg kg^{-1})	0.5689	0.4789
Coupling fluid inlet temperature (°C)	25	180

The component is initially set at a uniform temperature of 25°C with an equilibrium pressure of 400 kPa. Assuming a saturated liquid condition throughout the desorber sets the initial solution concentration at 0.5689 kg kg^{-1}. The solution inlet and coupling fluid mass flow rates are held constant for the duration of the simulation at 0.00975 kg s^{-1} and 0.084 kg s^{-1}, respectively. The final steady-state conditions for the solution and coupling fluid sides are representative of the design conditions for the desorber.

The parameter ramping times for the simulation cases are provided in Table 5. The desorber is held at the initial conditions for 60 seconds at the beginning of all cases to mitigate any numerical instabilities during start-up simulation. The coupling fluid and solution side property ramps are initiated simultaneously following this "*dead*" period. As the present model is used to simulate the open-loop performance of the desorber, the coupling fluid inlet temperature is ramped faster than the solution-side properties to emulate the delayed response of the solution side to coupling fluid

Table 5: Start-up simulation input times.

Parameter	Time
Solution side dead time (s)	60
Coupling fluid dead time (s)	60
Pressure ramp time (s)	600
Solution inlet temperature ramp time (s)	600
Solution inlet concentration ramp time (s)	600
Coupling fluid inlet temperature ramp time (s)	360
Total simulation time (s)	1200

temperature changes observed in actual systems. The solution side pressure, inlet concentration, and inlet temperature are ramped together.

The start-up simulations were performed with the simulation parameters shown in Table 2, except for the relative error tolerance (*RelTol*) and maximum step size (*MaxStep*) parameters, which were increased to 1×10^{-3} and decreased to 0.15 seconds, respectively, to improve the stability of the solver while maintaining a high level of accuracy. The start-up cases experience much larger property gradients in comparison to the steady-state cases presented above, which decrease stability. By relaxing the error tolerance and reducing the maximum step size, the solver is able to capture transient effects at a higher temporal resolution, although they may be solved in a coarser manner due to increased relative tolerance.

The open-loop nature of the present model requires manual ramping of the solution inlet properties in addition to the coupling fluid properties. Future integration into a system model would remove the solution side manual ramping requirement, as the desorber outlet conditions would feed back through other system components to set the inlet conditions of the concentrated solution. It should be noted that the start and end conditions of the simulations are realistic, steady-state conditions. The open-loop results presented here still provide valuable insight into the dynamic response of the desorber and can be used to develop control strategies for the component and the overall system.

Using the input parameters presented above, the desorber was simulated during start-up using the dynamic model. The time evolution of the desorber heat transfer rates, outlet mass flow rates, and variation of outlet temperatures were tracked and are presented in the following sections.

4.3.1. Variation of temperatures

The variation in the inlet and outlet temperatures of the desorber are shown in Figure 9. As the coupling fluid inlet temperature rises, heat transfer to the solution side increases, increasing the exiting dilute solution and refrigerant vapor temperatures. The dilute solution exiting the bottom of the desorber is hotter than the refrigerant vapor exiting the top because of the counter-flow configuration of coupling fluid and ammonia-water solution in the desorber. The solution side temperatures lag behind the coupling fluid temperature increase due to the damping characteristic of the desorber wall. As the coupling fluid heats rapidly, the temperature difference of the two fluid regions is transmitted via the desorber wall. The increase in wall temperature is driven by the balance of the two convective heat transfer terms, with a fraction of the heat transfer rate from the coupling fluid being used to heat the wall. The refrigerant vapor cools as it makes its way up the desorber interacting with the cooler solution.

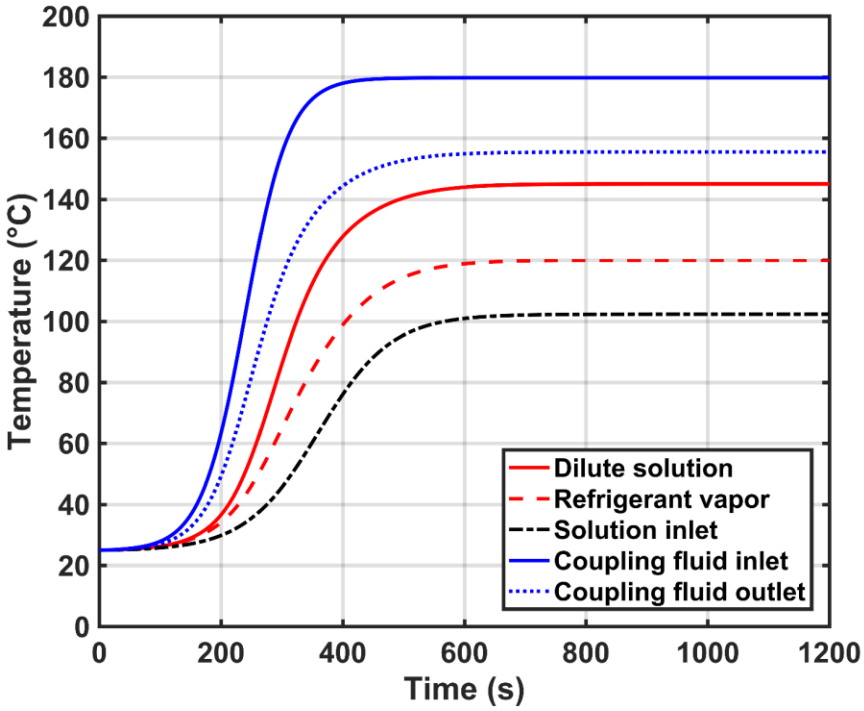

Figure 9: Time evolution of the solution and coupling fluid inlet and outlet temperatures.

4.3.2. Variation of heat transfer rates

The transient responses of the desorber heat transfer rates during start-up are presented in Figure 10. Solution-side, wall, and coupling fluid heat transfer rates are considered, including transverse heat flux, streamwise convective heat transfer, and energy storage terms. Axial conduction is neglected. Equations 28 – 31 define the overall energy balance and individual rate terms.

$$\dot{E}_{store} = \dot{Q}_{flux} + \dot{Q}_{conv} \tag{28}$$

$$\dot{E}_{store} = \frac{1}{\Delta t}\sum_{i=1}^{N}\left[m_i(t)\cdot u_i(t) - m_i(t-\Delta t)\cdot u_i(t-\Delta t)\right] \tag{29}$$

$$\dot{Q}_{flux}(t) = \sum\left[\dot{m}_{in}(t)\cdot h_{in}(t)\right] - \sum\left[\dot{m}_{out}(t)\cdot h_{out}(t)\right] \tag{30}$$

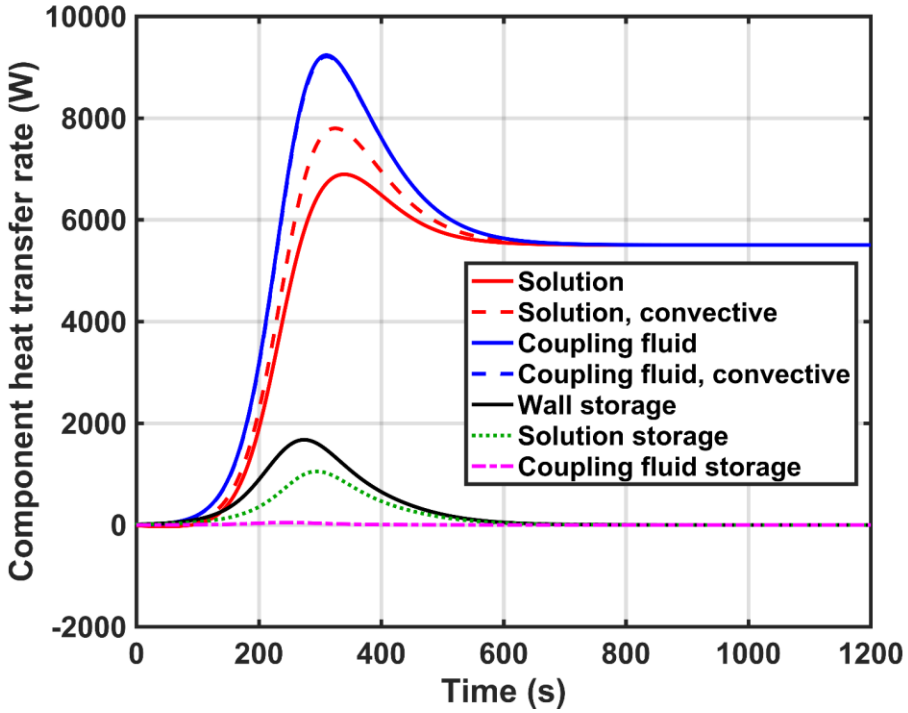

Figure 10: Variation of desorber heat transfer rates during start-up.

$$\dot{Q}_{conv}(t) = UA \cdot \left[\sum_{i=1}^{N} \Delta T_i \right] \tag{31}$$

After the completion of the dead period, the coupling fluid heat transfer rates increase rapidly, with the convective term closely following the flux term. This response is due to the increasing coupling fluid inlet temperature heating the coupling fluid region, which in turn is transferred to the cooler wall by convective heat transfer. The coupling fluid energy storage rate is small because of the microchannel geometry of the coupling fluid passages that minimizes fluid inventory and settles to zero at steady state. The initial peak in the coupling fluid heat transfer rate is attributed to rapid heat transfer to the wall, and subsequently to the solution, driven by large temperature differences. As the wall heat transfer rate starts to decrease and achieve a steady-state, the coupling fluid heat transfer rate also settles to its steady-state design value.

The wall energy storage rate term initially follows the growth of the coupling fluid heat transfer rates. But, the solution convective and heat flux heat transfer rates exceed the wall energy storage rate at approximately 55 and 80 seconds after ramping begins, respectively. Following the initial peak, the wall storage rate settles to its equilibrium value of zero at steady state.

The solution side energy storage is at its peak around 290 seconds and settles to zero at steady state. With the coupling fluid heat transfer rates achieving their peak values at about 310 seconds, the solution side convective heat transfer and flux terms lag behind by about 15 and 30 seconds, respectively. The solution side flux term has the slowest response of all the heat transfer rates, but its response speeds up as the solution outlet mass flow rates and outlet enthalpies reach their steady-state values.

Overall, the predicted heat transfer rate profiles resemble an underdamped system. A driving input, in this case an increase in system inlet temperatures, forces the desorber into a rapid rise in system heat transfer rates. This response is damped by energy storage in the solution and wall, pulling the system back to an equilibrium position. At steady-state, the desorber heat duty is 5.5 kW. This value agrees well with the results presented previously for the steady-state cases. During transients, the coupling fluid residual remains insignificant, while the solution side residual never exceeds an absolute value of 1 W, less than 0.1% of the steady-state heat transfer rate. In all transient simulations presented in this work, energy residuals remain below 1% of steady-state heat transfer values.

4.3.3. Variation of outlet mass flow rates

The transient response of the solution mass flow rates is shown in Figure 11. After the initial dead period where no vapor generation occurs, the desorber rapidly begins to generate refrigerant vapor as heat transfer from the coupling fluid increases. This causes a simultaneous decrease in the dilute solution flow rate. The peak of vapor generation and the minimum of dilute solution flow rates occur at about 310 seconds, which corresponds to the peak of coupling fluid heat transfer rate. As the heat transfer rate from the coupling fluid settles to its steady-state value, the outlet mass flow rates similarly achieve a steady state. The mass stored in the desorber is calculated using Equation 32.

$$M_{store}(t) = \sum_{i=1}^{N_{tray}} \rho_{f,i}(t) \times V_{f,seg} \tag{32}$$

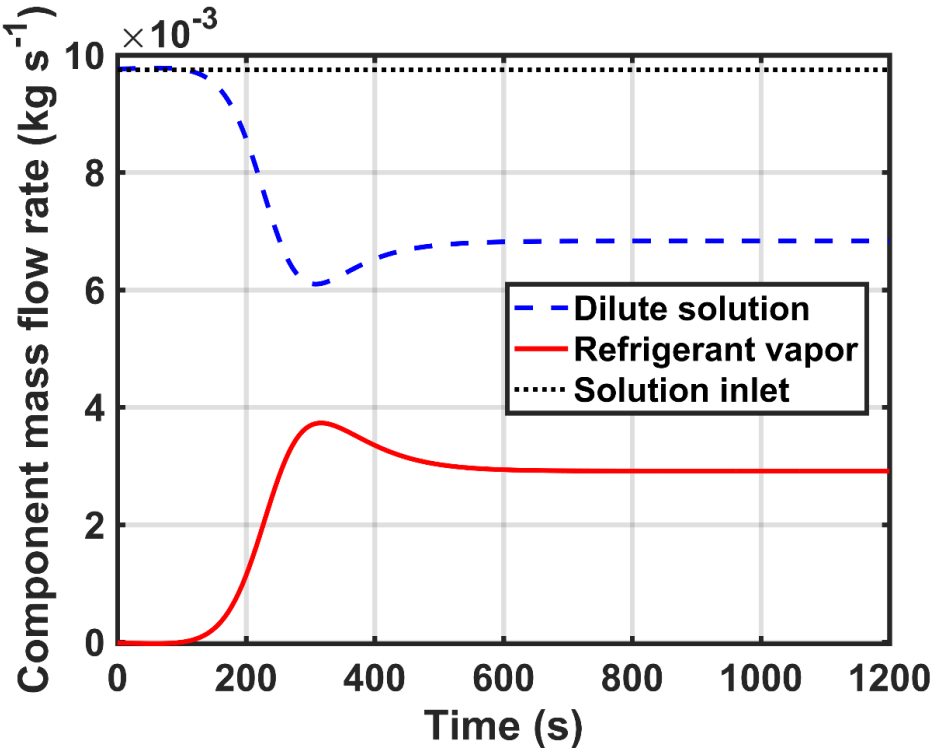

Figure 11: Variation of the desorber inlet and outlet solution mass flow rates during start-up.

4.3.4. Run time of cases considered

The start-up analyses in this study were performed using MATLAB® 2016b on a 2.40 GHz computer with 16 GB of RAM and ranged from 1,000 seconds to 1,360 seconds for a simulation time of 1,200 seconds.

4.4 Transient performance

The response of the desorber to extreme changes in inlet conditions from their design values is investigated here. These cases provide insights about desorber performance at off-design conditions that can be used in the design of a control system to adjust input parameters to maintain system cooling demand.

Three main categories of simulations are presented: 1) solution inlet mass flow rate variation (0.00731 kg s^{-1} to 0.1219 kg s^{-1}), 2) coupling fluid inlet temperature variation (150°C to 180°C), and 3) ambient temperature variation (29°C to 45°C). Each simulation starts with the desorber at its steady-state design conditions, as previously presented in Table 4 and ambient temperature of 35°C. A given input variable is then either increased or decreased from its design value to a given extreme operating condition. Ramping times for these input parameters vary for each test case and are intended to emulate trends expected in actual operation.

4.4.1. Response to change in solution inlet mass flow rate

One of the key control methods for an absorption system is the tuning of the solution mass flow rate through the adjustment of a variable speed solution pump. The input conditions and simulation times for the solution inlet mass flow rate cases are presented in Table 6.

Table 6: Initial and final conditions, and simulation times for desorber solution inlet mass flow rate perturbation cases.

Constant Parameters		**Value**
Coupling fluid inlet temperature (°C)		180
Coupling fluid flow rate (kg s^{-1})		0.084
Solution inlet vapor quality (-)		0
Ambient temperature (°C)		35
Ramped Parameters	**Initial**	**Final**
Solution inlet flow rate (kg s^{-1})	0.00975	0.00731, 0.01219
Solution inlet temperature (°C)	102.5	96.86, 106.26
Pressure (kPa)	2087	2001, 2123
Solution inlet concentration (kg kg^{-1})	0.4789	0.4982, 0.4639
Simulation Time Name		**Time**
Total simulation time (s)		400
Solution side dead time (s)		15
Solution inlet mass flow rate ramp time (s)		15
Pressure ramp time (s)		60
Solution inlet temperature ramp time (s)		60
Solution inlet concentration ramp time (s)		60

Two cases are considered in this category: 1) the solution inlet mass flow rate is ramped down to 0.00731 kg s^{-1} from the design condition of 0.00975 kg s^{-1} over 15 seconds and 2) the solution inlet mass flow rate is ramped up to 0.01219 kg s^{-1} from the design condition of 0.00975 kg s^{-1} over 15 seconds. During both transients, the coupling fluid inlet temperature and mass flow rate remain at their design conditions of 180°C and 0.084 kg s^{-1}, respectively. The solution pressure, inlet temperature, and inlet concentration are ramped over 60 seconds in response to the change in solution inlet mass flow rate. For the case where the solution inlet mass flow is increased,

the pressure is increased from 2087 kPa to 2123 kPa, the solution inlet temperature from 102.5°C to 106.3°C, and the solution inlet concentration decreased from 0.4789 kg kg^{-1} to 0.4639 kg kg^{-1}. In the second case, the pressure is decreased from 2087 kPa to 2001 kPa, the solution inlet temperature from 102.5°C to 96.9°C, and the solution inlet concentration increased from 0.4789 kg kg^{-1} to 0.4982 kg kg^{-1}. The simulations are conducted for 400 seconds total, after which steady state is deemed to have been achieved as the energy and mass residuals decrease below 1% of the steady-state conditions. The plots shown in this section, however, are shown for the interval from t = 0 s to t = 200 s to show the detail in the time-evolution of various responses.

4.4.1.1. Mass flow rate variation

The variation of inlet and outlet mass flow rates in response to a change in the solution inlet mass flow rate is shown in Figure 12. Plot A presents the mass flow rate response to a 25% increase in solution inlet mass flow rate from the design condition of 0.00975 kg s^{-1}, while Plot B shows the response to a 25% decrease in inlet flow rate.

As discussed in the previous section, the model maintains constant heat transfer conductance values. Therefore, the key parameter governing heat transfer rate is the driving

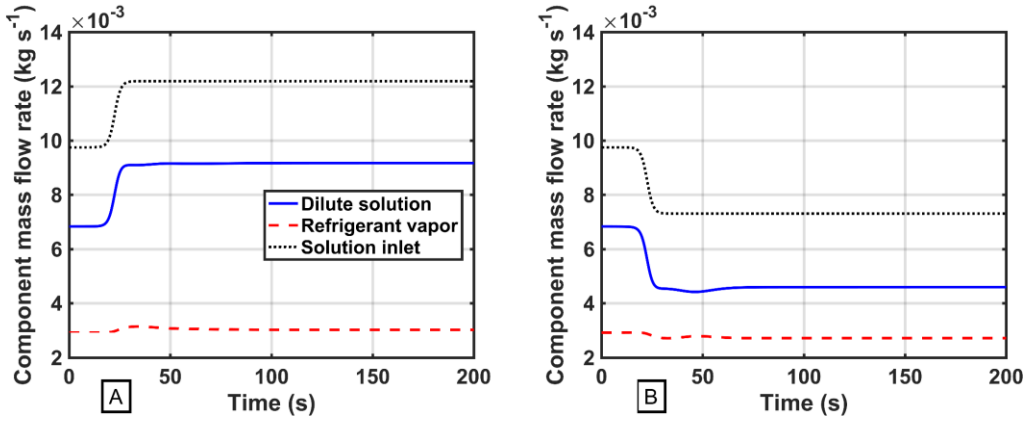

Figure 12: Response of desorber flow rates to an increase (A) and decrease (B) of solution inlet mass flow rate.

temperature difference. The coupling fluid inlet conditions remain unchanged, but the solution inlet temperature changes due to variations in pressure and concentration. The additional mass flow rate, coupled with species and energy conservation equations, leads to a corresponding variation in the heat transfer rate. In general, an increase in the inlet mass flow rate results in increases in the refrigerant vapor and dilute solution mass flow rates. The stored fluid mass in the component remains relatively constant as the density of ammonia-water at the inlet remains approximately constant with simultaneous changes in inlet temperature, pressure and concentration.

As shown in Plot A of Figure 12, an increase in the solution inlet flow rate from 0.00975 kg s^{-1} to 0.01219 kg s^{-1} results in an increase in the refrigerant vapor flow rate from 0.002917 kg s^{-1} to 0.003021 kg s^{-1}, and an increase in the dilute solution flow rate from 0.006833 kg s^{-1} to 0.009171 kg s^{-1}. During transients, the dilute solution mass flow rate increases quickly and smoothly during the 15 seconds of inlet mass flow rate ramping to its final steady-state value. This effect is driven by the inlet solution flow and is affected very little by variations in other properties. The refrigerant vapor flow rate, however, is affected by other thermodynamic property changes, such as temperature, pressure and concentration during transients. In the 15-second period of inlet flow rate ramping, the vapor flow rate peaks at a flow rate of 0.003142 kg s^{-1}, and then settles at its new steady-state value of 0.003021 kg s^{-1} in the following 70 seconds (t = 100 s). This overshoot is due to the rapid influx of additional mass into the system while the component thermodynamic properties (pressure, temperature, concentration) lag behind. After the variation in the inlet flow rate of the concentrated solution, the pressure and solution inlet temperature continue to increase, which reduce vapor generation due to decreased heat transfer as compared to the peak of the transients.

Figure 12 (B) presents the outlet mass flow rates in response to a decrease in the solution inlet mass flow rate from 0.00975 kg s^{-1} to 0.007309 kg s^{-1} over 15 seconds. The mass flow rate of dilute solution decreases from 0.006833 kg s^{-1} to a new steady-state value of 0.004596 kg s^{-1}, while the refrigerant vapor decreases from 0.002917 kg s^{-1} to 0.002712 kg s^{-1}. During the period where the solution inlet mass flow rate is decreasing (t = 15 s to t = 30 s), the dilute solution and vapor mass flow rates decrease simultaneously to points just beyond their steady-state values due to the decrease in the inlet mass flow rate. As the end of the mass flow rate transient duration is reached, the pressure and solution inlet temperature continue to decrease for another 45 seconds till t = 75 s. During this period, the refrigerant vapor increases to a peak of 0.002786 kg s^{-1} at about t = 50 s and then decreases to its steady-state value. The dilute solution flow rate also decreases during this period to 0.00442 kg s^{-1} due to the increased vapor generation.

4.4.1.2. Heat transfer rate variation

The variation in desorber heat transfer rates due to a solution inlet flow rate increase (Plot A) and decrease (Plot B) are shown in Figure 13. In general, the desorber heat transfer rates

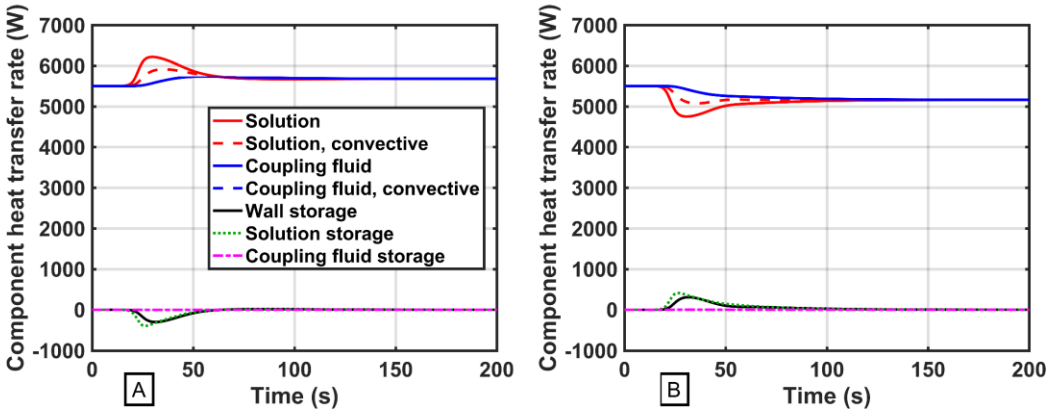

Figure 13: Response of desorber heat transfer rates to an increase (A) and decrease (B) of solution inlet mass flow rate.

increase with an increase in the solution inlet mass flow rate, and decrease with a decrease in the solution inlet mass flow rate.

In Plot A of Figure 13, the desorber heat transfer rate response to an increase in solution inlet flow rate results in an increase in the desorber heat transfer rate from 5.50 kW to 5.68 kW. Noticeable inflection points in the solution flux and convective heat transfer rates occur during the transient period, as well as a corresponding decrease in the solution and wall storage rates. These peaks are an initial response to the increase in the mass flow rate in the system, while the thermodynamic properties experience a time delay imposed by the ramping conditions that are representative of typical values observed in experiments. As the temperatures in the component decrease, the heat transfer rate from the coupling fluid increases due to a larger temperature differential. The system then settles at its new steady-state heat transfer rate of 5.68 kW, and component energy storage rates decrease to zero as the pressure, inlet temperature, and inlet concentration reach their final values.

The desorber heat transfer rate response to a decrease in the solution inlet flow rate is presented in Plot B of Figure 13. The steady-state heat transfer rate of the system decreases from 5.50 kW to 5.16 kW. During the transient, reverse trends in the solution flux and convective heat transfer rates occur due to the decreased mass flow rate. This results in a higher heat transfer rate from the coupling fluid than from the solution. In response, the solution and wall storage rates increase and the solution temperature increases. Finally, the energy storage is reduced to zero and the heat transfer rates settle at their new steady-state position.

4.4.1.3. Temperature variation

Figure 14 presents the variation in the desorber inlet and outlet temperatures in response to an increase (A) and decrease (B) in the solution inlet mass flow rate. In general, an increase in

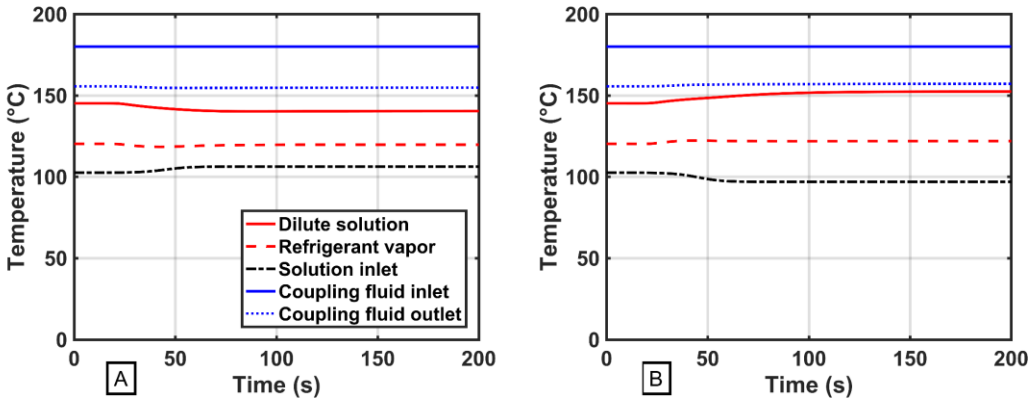

Figure 14: Response of desorber temperatures to an increase (A) and decrease (B) of solution inlet mass flow rate.

solution inlet mass flow rate results in a decrease in outlet temperatures, while a decrease in solution inlet mass flow rate leads to an increase in outlet temperatures.

Figure 14 (A) shows the response of the desorber temperatures to an increase in the solution inlet mass flow rate. The dilute solution steady-state temperature decreases from 145.2°C to 140.4°C due to the increased mass flow rate in the system and the increased dilute solution concentration. Similarly, the refrigerant vapor steady-state temperature decreases from 120.2°C to 119.7°C due to the increase in the refrigerant concentration and increased mass flow rate. During the transient period of mass flow rate and solution inlet property ramping (t = 15 s to t = 75 s), the dilute solution temperature decreases smoothly to its new steady-state position. On the other hand, the refrigerant vapor temperature first decreases to 118.4°C before settling at its new steady-state value of 119.7°C. This underdamped response is a result of the rapid mass flow rate variation. The increased heat transfer rate also causes the reduction of the coupling fluid outlet temperature from 155.6°C to 154.8°C.

The desorber temperature response to a decrease in the solution inlet mass flow rate is shown in Plot A of Figure 14. The refrigerant vapor temperature increases from 120.2°C to

121.9°C, while the dilute solution temperature increases from 145.2°C to 152.4°C. During the transient period, the dilute solution temperature rises smoothly to its new steady state, whereas the refrigerant vapor temperature first overshoots its final temperature in an underdamped manner.

4.4.1.4. Concentration variation

In Figure 15, the responses of the desorber concentrations to an increase (A) and decrease (B) in the solution inlet mass flow rate are shown. In general, an increase in the solution inlet mass flow rate results in an increase in the dilute solution and refrigerant vapor concentrations, and a decrease in the inlet flow rate leads to a decrease in the concentration of the two solution outlet streams.

With an increase in the solution inlet flow rate, the refrigerant vapor concentration increases from 0.9387 kg kg^{-1} to 0.9414 kg kg^{-1}, while the dilute solution concentration increases from 0.2826 kg kg^{-1} to 0.3066 kg kg^{-1}. The dilute solution concentration profile during the transient is representative of its temperature profile. The resulting refrigerant vapor concentration profile is dynamically determined by tray efficiencies, which define the thermal inequilibrium at the outlet of the desorber. As the dilute solution concentration increases, the vapor concentration on the

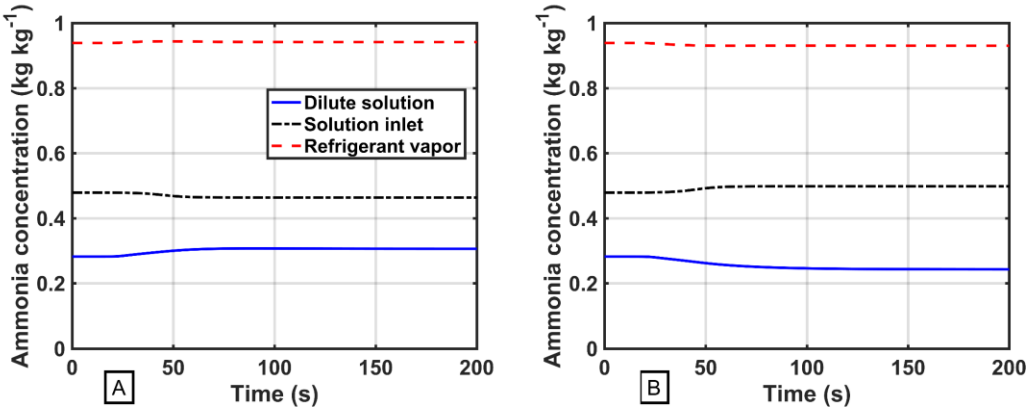

Figure 15: Response of desorber concentrations to an increase (A) and decrease (B) of solution inlet mass flow rate.

bottom tray also increases due to the constant tray efficiency relationship. This increase in concentration has a cascading effect through the remaining trays in the desorber, finally increasing the refrigerant vapor concentration.

Figure 15 (B) shows the response of the desorber concentrations to a decrease in the solution inlet mass flow rate. The refrigerant vapor concentration decreases from 0.9387 kg kg^{-1} to 0.9302 kg kg^{-1}, while the dilute solution concentration decreases from 0.2826 kg kg^{-1} to 0.2434 kg kg^{-1}.

4.4.2. Response to change in coupling fluid inlet temperature

The transient response of the desorber to a change in the coupling fluid inlet temperature is presented here. This scenario occurs in an absorption system when the heat source (natural gas combustor, waste-heat streams, solar energy, etc.) that supplies heat to the coupling fluid loop changes. By controlling this energy input, the performance of the desorber and the complete absorption system can be modified. The input conditions and simulation times for the coupling fluid inlet temperature cases are presented in Table 7.

Two cases are presented: 1) the coupling fluid inlet temperature is increased from 180°C to 200°C, and 2) the coupling fluid inlet temperature is decreased from 180°C to 150°C. In both cases, the coupling fluid mass flow rate, solution inlet mass flow rate, and ambient temperature are held constant at 0.084 kg s^{-1}, 0.00975 kg s^{-1}, and 35°C, respectively. To begin the simulations, the system is first held at initial conditions for 15 seconds to account for any start-up effects. At the end of this "dead" period, the coupling fluid inlet temperature is ramped to its final value over

Table 7: Initial and final conditions, and simulation times for desorber coupling fluid inlet temperature perturbation cases.

Constant Parameters		**Value**
Coupling fluid flow rate (kg s-1)		0.084
Solution inlet flow rate (kg s^{-1})		0.00975
Solution inlet vapor quality (-)		0
Ambient temperature (°C)		35
Ramped Parameters	**Initial**	**Final**
Coupling fluid inlet temperature (°C)	180	150, 200
Solution inlet temperature (°C)	102.5	94.6, 107.5
Pressure (kPa)	2087	1911, 2202
Solution inlet concentration (kg kg^{-1})	0.4789	0.4988, 0.4668
Simulation Time Name		**Time**
Total simulation time (s)		400
Solution side dead time (s)		15
Coupling fluid side dead time (s)		15
Solution side ramp time (s)		120
Coupling fluid inlet temperature ramp time (s)		60

60 seconds (t = 15 s to t = 75 s). At the same time, the solution inlet properties are ramped over 120 seconds (t = 15 s to t = 135 s). The solution properties respond to the change in coupling fluid inlet temperature, resulting in a longer ramp time. For the case in which the coupling fluid inlet temperature increases, the solution pressure increases from 2087 kPa to 2202 kPa, the solution inlet temperature increases from 102.5°C to 107.5°C, and the solution inlet concentration decreases from 0.4789 kg kg^{-1} to 0.4668 kg kg^{-1}. In the case in which the coupling fluid inlet temperature decreases, the solution pressure decreases from 2087 kPa to 1911 kPa, the solution

inlet temperature decreases from 102.5°C to 94.6°C, and the solution inlet concentration increases from 0.4789 kg kg^{-1} to 0.4988 kg kg^{-1}.

4.4.2.1. Mass flow rate variation

The variations in the desorber mass flow rates because of an increase (Plot A) and decrease (Plot B) in the coupling fluid inlet temperature are presented in Figure 16. In general, an increase in the coupling fluid inlet temperature results in an increase in the refrigerant vapor flow rate and a decrease in the dilute solution flow rate. Conversely, a decrease in the coupling fluid inlet temperature leads to a decrease in the refrigerant vapor flow rate and an increase in the dilute solution flow rate.

Increasing the coupling fluid inlet temperature from 180°C to 200°C from t = 15 s to t = 75 s results in the solution mass flow rate response shown in Plot A of Figure 16. The refrigerant vapor mass flow rate increases from 0.002917 kg s^{-1} to 0.00333 kg s^{-1}, while the dilute solution mass flow rate decreases from 0.006833 kg s^{-1} to 0.00642 kg s^{-1}. The increase in vapor generation rate in the desorber is due to the increased temperature difference between the coupling fluid and solution, which increases the heat transfer rate. During the transient period (t = 15 s to t = 135 s),

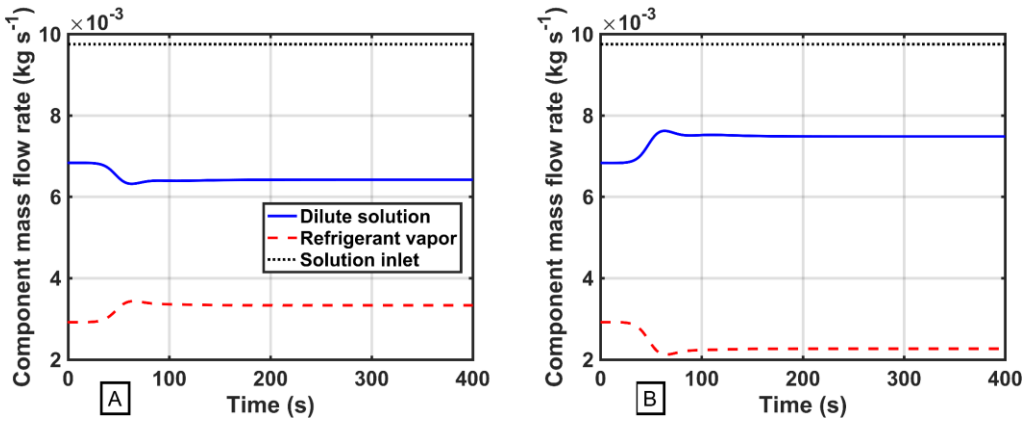

Figure 16: Response of desorber flow rates to an increase (A) and decrease (B) in the coupling fluid inlet temperature.

both the refrigerant and dilute solution flow rates overshoot their respective steady-state values. The refrigerant flow rate achieves a peak value of 0.003433 kg s^{-1} and the dilute solution a minimum of 0.006319 kg s^{-1}. This response is due to the lag in the solution side inlet properties compared to the increase in the coupling fluid inlet temperature rise. During the transient period, the coupling fluid heat transfer rate is elevated, generating more vapor. As the solution-side pressure and inlet temperature increase, heat transfer from the coupling fluid decreases and the flow rates return to their steady-state levels.

The response of the desorber mass flow rates to a decrease in the coupling fluid temperature from 180°C to 150°C is shown in Plot B of Figure 16. The refrigerant flow rate decreases from 0.002917 kg s^{-1} to 0.002267 kg s^{-1}, while the dilute solution flow rate increases from 0.006833 kg s^{-1} to 0.007483 kg s^{-1}. The decrease in vapor generation is due to the reduction in the temperature difference between the coupling fluid and solution, which in turn decreases the heat transfer rate During the transient period, the dilute solution overshoots its steady-state value, reaching a peak at about t = 65 s of 0.007622 kg s^{-1}. Conversely, the refrigerant vapor flow rate has a minimum value of 0.002124 kg s^{-1}. This response is due to the rapid decrease in the coupling fluid heat transfer rate. The solution inlet properties lag the change in coupling fluid temperature, leading to the abovementioned response. As the pressure and solution inlet temperature decrease beyond the end of the coupling fluid inlet temperature ramp, the dilute solution flow rate decreases, and the refrigerant vapor flow rate increases, respectively, to their final steady-state values.

4.4.2.2. Heat transfer rate variation

The responses of the desorber heat transfer rate to an increase (A) and decrease (B) in the coupling fluid inlet temperature are shown in Figure 17. If the coupling fluid inlet temperature is

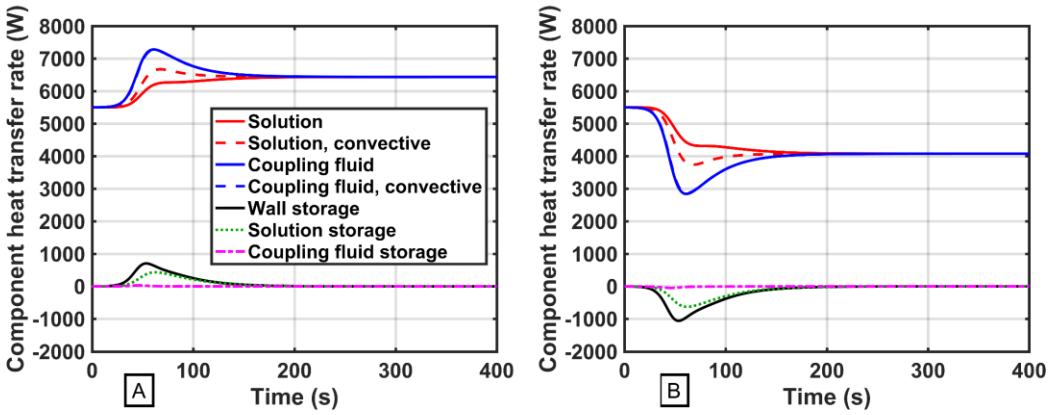

Figure 17: Response of desorber heat transfer rates to an increase (left) and decrease (right) in the coupling fluid inlet temperature.

increased, the heat transfer rates increase, whereas if the coupling fluid inlet temperature decreases, the heat transfer rates decrease.

Heat transfer rates that result from an increase in the coupling fluid inlet temperature are presented in Plot A of Figure 17. The steady-state heat transfer rates increase from 5.50 kW to 6.44 kW. The increase in heat transfer rates occurs because of the increase in the temperature difference between the solution inlet and coupling fluid inlet temperatures. During the transient period, the coupling fluid heat transfer rate increases faster and to a larger amplitude than the solution heat transfer rates. This is due to the faster ramp of the coupling fluid inlet temperature in comparison with that of the solution inlet properties. In response to the increased energy input into the system, the wall and solution storage rates increase. As the solution flux and convective heat transfer rates respond, the energy storage rates decrease until a new equilibrium is achieved.

Plot B of Figure 17 shows the time-evolution of the heat transfer rates due to a decrease in the coupling fluid inlet temperature. The heat transfer rates decrease from 5.50 kW to 4.08 kW in response to this change. The reduced difference between the coupling fluid and solution temperatures in comparison to the design conditions causes this reduction in the heat transfer rates.

4.4.2.3. Temperature variation

Figure 18 shows the variation in the inlet and outlet desorber temperatures as a result of an increase (Plot A) and decrease (Plot B) in the coupling fluid inlet temperature. In general, if the coupling fluid inlet temperature is increased, the refrigerant vapor, dilute solution, solution inlet, and coupling fluid outlet temperatures increase as well. If the coupling fluid inlet temperature decreases, all the inlet and outlet temperatures decrease as well.

Plot A of Figure 18 presents the response of the desorber temperatures to an increase in the coupling fluid inlet temperature. The refrigerant vapor temperature increases from 120.2°C to 129.9°C, the dilute solution temperature increases from 145.2°C to 159.7°C, and the coupling fluid outlet temperature increases from 155.6°C to 171.5°C.

The time-evolution of the desorber temperatures due to a decrease in the coupling fluid inlet temperature is shown in Plot B of Figure 18. The refrigerant vapor, dilute solution, and coupling fluid outlet temperatures decrease from 120.2°C to 106.0°C, 145.2°C to 123.3°C, and 155.6°C to 132°C, respectively. Thermal capacitance effects cause the coupling fluid temperatures to respond first, followed by the solution-side temperatures.

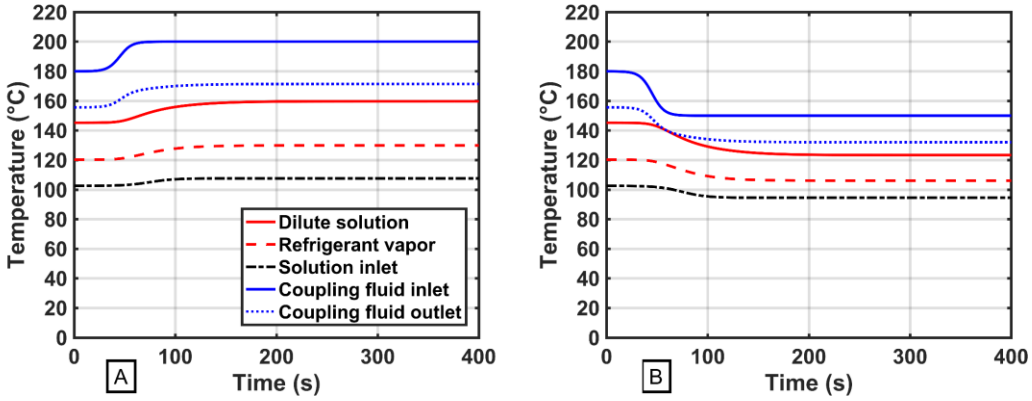

Figure 18: Response of desorber temperatures to an increase (A) and decrease (B) in the coupling fluid inlet temperature.

4.4.2.4. Concentration variation

In Figure 19, the response of the desorber concentrations to an increase (A) and decrease (B) in the coupling fluid inlet temperature are presented. In general, an increase in the coupling fluid inlet temperature results in a decrease in the refrigerant vapor and dilute solution concentrations. Conversely, the refrigerant vapor and dilute solution concentrations increase in response to a decrease in the coupling fluid inlet temperature.

The response of the solution concentrations due to an increase in the coupling fluid inlet temperature are presented in Plot A of Figure 19. The refrigerant vapor concentration decreases from 0.9387 kg kg^{-1} to 0.9151 kg kg^{-1}. The dilute solution concentration decreases from 0.2826 kg kg^{-1} to 0.2343 kg kg^{-1}. The decrease in the refrigerant vapor concentration follows the increase in the outlet vapor temperature in the system. The dilute solution concentration decreases as well to satisfy the species conservation equation.

Plot B of Figure 19 shows the response of the desorber concentrations to a decrease in the coupling fluid inlet temperature. The refrigerant vapor concentration increases from 0.9387 kg kg^{-1} to 0.9639 kg kg^{-1}. The dilute solution concentration increases from 0.2826 kg kg^{-1} to 0.3579 kg

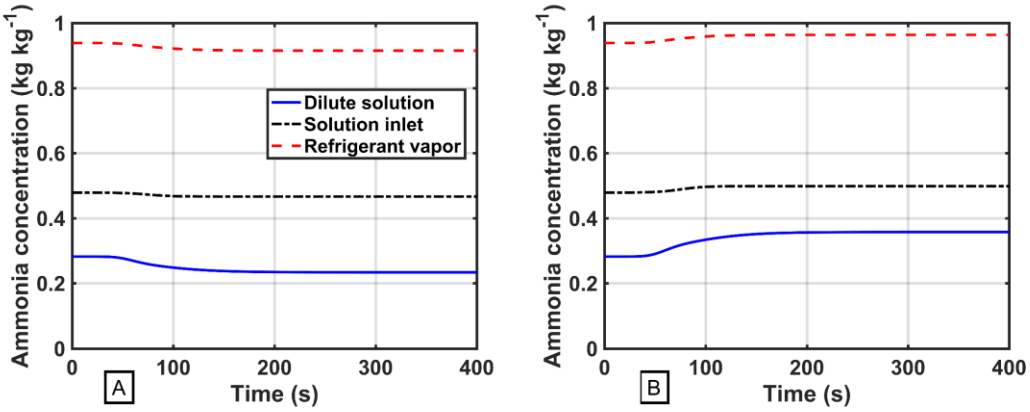

Figure 19: Response of desorber concentrations to an increase (A) and decrease (B) in the coupling fluid inlet temperature.

kg^{-1}. The refrigerant concentration increases in response to the decrease in the outlet vapor temperature. Similar to the coupling fluid inlet temperature increase case, the dilute solution concentration increases to satisfy species conservation following the decrease in the vapor mass flow rate and the increase in the dilute solution flow rate.

The responses of the desorber flow rates, heat transfer rates, concentration, and temperatures to a change in the coupling fluid inlet temperature were discussed above. An increase in the coupling fluid inlet temperature leads to an increase in heat transfer rates and refrigerant vapor generation. However, the generated refrigerant vapor exits the desorber at a lower concentration due to the increase in the vapor temperature. Decreasing the coupling fluid inlet temperature has an inverse effect, decreasing the desorber heat transfer rates and vapor mass flow rates. However, the refrigerant concentration increases significantly with the decrease in the outlet vapor temperature. Tuning of the coupling fluid temperature is an effective means to control the refrigerant vapor flow rate and overall system capacity.

4.4.3. Response to change in ambient temperature

The response to a change in the ambient temperature is also considered. Unlike the other simulations described above, this represents a change in an uncontrolled input in a different part of the system outside the desorber that is the focus of the present study. This ambient condition change is not a direct input into the desorber model, but instead affects the solution pressure, inlet temperature, and inlet concentration by changing the ambient coupling of the condenser and absorber in the overall absorption system. These changes in ambient temperature can occur due to diurnal or seasonal variations and lead to changes in system performance. Understanding the response of the desorber to this change will guide the design of control algorithms to improve performance at these off-design conditions. The input conditions and simulation times for ambient

temperature change cases are presented in Table 8. For this standalone desorber model, it is assumed that the changes in the solution pressure, inlet temperature, and inlet concentration occur over the same duration in response to the change in ambient temperature. A complete system model can provide a more realistic rate of variation in these properties due to the change in ambient conditions.

In the first case, the ambient temperature is increased from 35°C to 45°C over 240 seconds. This change results in the solution-side pressure increasing from 2087 kPa to 2459 kPa, the solution inlet temperature increasing from 102.5°C to 118.6°C, and the solution inlet concentration

Table 8: Initial and final conditions, and simulation times for desorber ambient temperature perturbation cases.

Constant Parameters		**Value**
Coupling fluid inlet temperature (°C)		180
Coupling fluid flow rate (kg s^{-1})		0.084
Solution inlet flow rate (kg s^{-1})		0.00975
Solution inlet vapor quality (-)		0
Ramped Parameters	**Initial**	**Final**
Ambient temperature (°C)	35	29, 45
Solution inlet temperature (°C)	102.5	93.0, 118.6
Pressure (kPa)	2087	1884, 2459
Solution inlet concentration (kg kg^{-1})	0.4789	0.5038, 0.4400
Simulation Time Name		**Time**
Total simulation time (s)		400
Solution side dead time (s)		15
Pressure ramp time (s)		240
Solution inlet temperature ramp time (s)		240
Solution inlet concentration ramp time (s)		240

decreasing from 0.4789 kg kg^{-1} to 0.4400 kg kg^{-1}, all in the 240 second ramping period. In the second case, the ambient temperature decreases from 35°C to 29°C over 240 seconds. Due to the decrease in ambient temperature, the solution pressure, inlet temperature, and inlet concentration change from their design conditions from 2087 kPa to 1884 kPa, 102.5°C to 93.0°C, and 0.4789 kg kg^{-1} to 0.5038 kg kg^{-1} in the 240 second ramping period, respectively. In both cases, the coupling fluid inlet temperature and mass flow rate remain at their design values of 180°C and 0.084 kg s^{-1}, respectively. The solution inlet mass flow rate also remains constant at 0.00975 kg s^{-1}.

4.4.3.1. Mass flow rate variation

The responses of the desorber mass flow rates to an increase (A) and decrease (B) in the ambient temperature are presented in Figure 20. In general, an increase in the ambient temperature results in an increase in the dilute solution mass flow rate and a decrease in the refrigerant vapor mass flow rate. Conversely, a decrease in the ambient temperature leads to a decrease in the dilute solution mass flow rate and an increase in the refrigerant vapor mass flow rate.

Plot A of Figure 20 shows the response of the desorber mass flow rates to an increase in the ambient temperature from 35°C to 45°C. The simulation remains at steady-state for the first 15 seconds, and then the solution pressure, inlet temperature, and inlet concentration are ramped over 240 seconds (t = 15 s to t = 255 s) to their final conditions of 2459 kPa, 118.6°C, 0.4400 kg kg^{-1}, respectively. During this period, the refrigerant vapor flow rate decreases from 0.002915 kg s^{-1} to 0.002301 kg s^{-1} and the dilute solution flow rate increases from 0.006836 kg s^{-1} to 0.007449 kg s^{-1}. The decrease in the refrigerant vapor flow rate and, thus, increase in dilute solution flow rate, are results of the decrease in the temperature difference between the solution and coupling fluid that drives the heat transfer. An increase in the ambient temperature leads to a decrease in the heat transfer in the absorber, leading to a hotter solution and lower concentration at the inlet of the

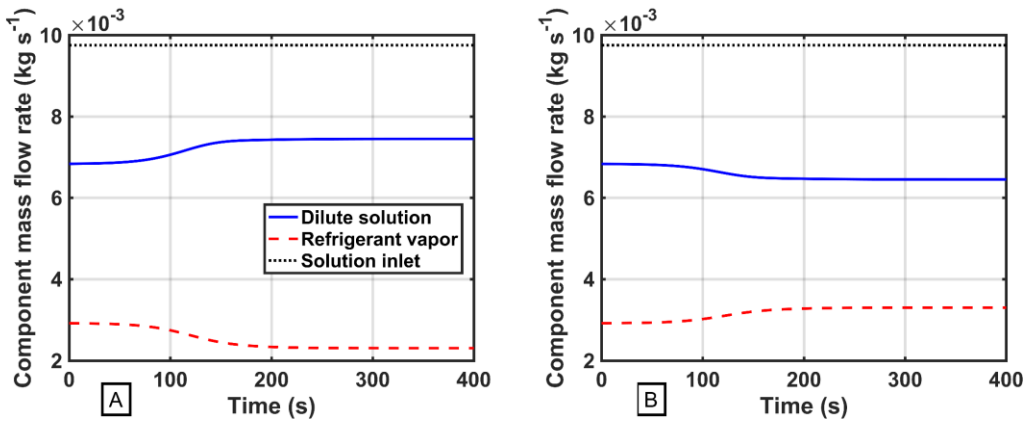

Figure 20: Response of desorber flow rates to an increase (A) and decrease (B) in ambient temperature.

desorber. This hotter solution reduces the heat transfer rates, and combined with lower ammonia concentration, decreases the amount of refrigerant vapor generated in the desorber. During transients, both outlet flow rates reach their new steady-state values during the inlet ramping period from t = 15 s to t = 255 s, reflecting the smooth and gradual ramp in the inlet solution properties.

In Figure 20, Plot B presents the desorber mass flow rate response to a decrease in the ambient temperature from 35°C to 29°C over 240 seconds from t = 15 s to t = 255 s. This ambient change results in the pressure changing to 1884 kPa, the solution inlet temperature changing to 93.0°C, and the inlet concentration changing to 0.5038 kg kg^{-1}, all from design conditions during the 240 second ramping period. These solution-side changes lead to the refrigerant vapor flow rate increasing from 0.002917 kg s^{-1} to 0.003300 kg s^{-1} and the dilute solution flow rate decreasing from 0.006832 kg s^{-1} to 0.00645 kg s^{-1}. The increase in refrigerant vapor flow rate results from the increase in the temperature driving temperature difference between the solution and coupling fluid, resulting in an increase in heat transfer rate. The solution inlet mass flow rate is kept constant, and as a consequence, the dilute solution flow rate decreases. During the transient period from t = 15

s to t = 255 s, both flow rates achieve steady state a smooth ramp-up/ramp-down manner due to the corresponding changes in the inlet solution conditions.

4.4.3.2. Heat transfer rate variation

The time-evolution of the desorber heat transfer rates in response to an increase (Plot A) and decrease (Plot B) in the ambient temperature are presented in Figure 21. In general, an increase in the ambient temperature results in a decrease in the heat transfer rates and a decrease in the ambient temperature results in an increase in the heat transfer rates.

Figure 21 (A) presents the variation in heat transfer rates due to an increase in the ambient temperature. The overall desorber heat transfer rate decreases from 5.50 kW to 4.38 kW because of the decrease in the temperature difference between the coupling fluid and solution temperatures. During transients, the solution-side flux and convective heat transfer rates decrease faster than the coupling fluid-side heat transfer rates because of the thermal capacitance effects in the solution and the desorber wall. During transients, the wall and solution energy storage rates increase as the solution temperature increases. As the coupling fluid heat transfer decreases due to the increased

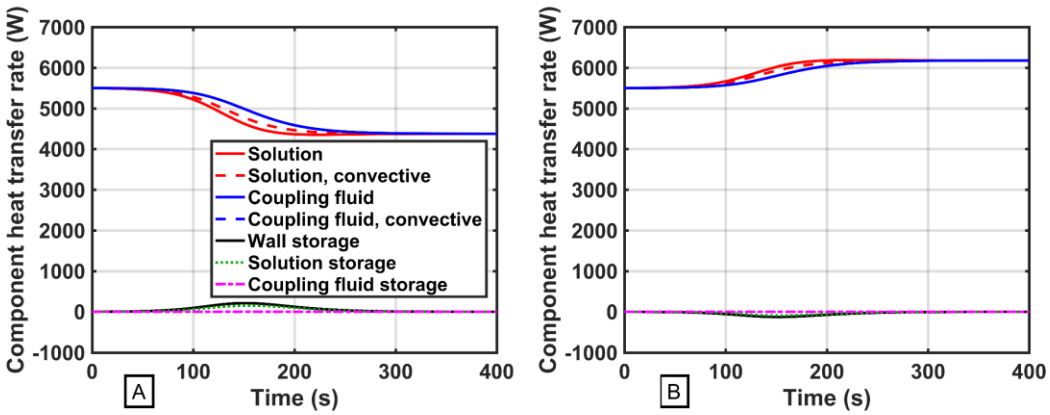

Figure 21: Response of desorber heat transfer rates to an increase (A) and decrease (B) in ambient temperature.

solution temperature, the storage rates decrease back to zero and the system settles to a new steady state.

Plot B of Figure 21 shows the response of the desorber heat transfer rates to a decrease in the ambient temperature. The desorber heat transfer rates increase from 5.50 kW to 6.18 kW due to the larger temperature difference between the solution and coupling fluid temperatures. Thermal capacitance effects in the stored solution mass and the heat exchanger wall cause the coupling fluid side heat transfer rate to lag behind the solution heat transfer rate finally reaching a new steady-state.

4.4.3.3. Temperature variation

Figure 22 presents the response of the desorber solution and coupling fluid inlet and outlet temperatures to an increase (A) and decrease (B) in the ambient temperature. In general, an increase in the ambient temperature results in an increase in the solution inlet and outlet temperatures, as well as the coupling fluid outlet temperature. When a decrease in the ambient temperature occurs, the solution inlet and outlet temperatures, and the coupling fluid outlet temperature decrease. In both cases, the coupling fluid inlet temperature is maintained constant at the design condition.

Figure 22 (A) presents the response of the component temperatures to an increase in the ambient temperature. The refrigerant vapor, dilute solution, and coupling fluid outlet temperatures increase from 120.2°C to 132.4°C, 145.2°C to 151.7°C, and 155.6°C to 160.6°C, respectively. As the solution inlet temperature increases, the refrigerant vapor and dilute solution temperatures increase as well. The increase in the solution temperature leads to a decrease in the heat transfer from the coupling fluid, resulting in an increase in the coupling fluid outlet temperature. The

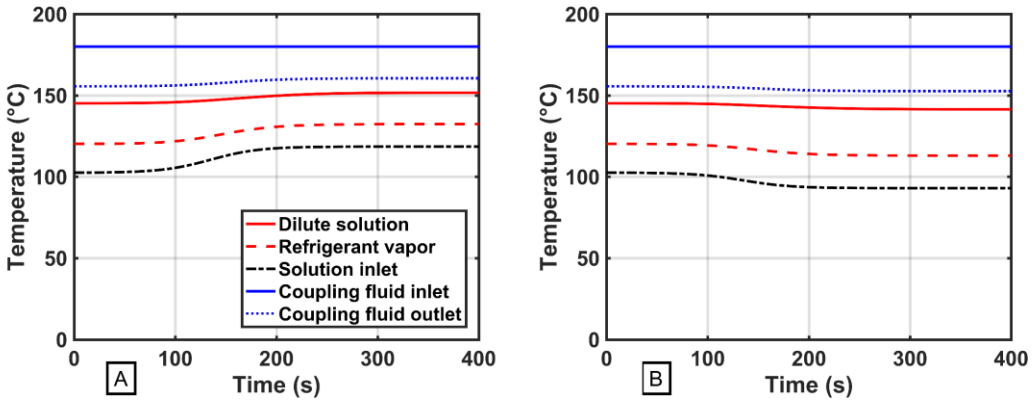

Figure 22: Response of desorber temperatures to an increase (A) and decrease (B) in ambient temperature.

refrigerant vapor temperature increases the fastest after the solution inlet temperature due to the solution inlet and vapor outlet being at the same location in the desorber.

The response of the desorber temperatures to a decrease in the ambient temperature is shown in Plot B of Figure 22. The refrigerant vapor temperature decreases from 120.2°C to 113.0°C, the dilute solution temperature decreases from 145.2°C to 141.5°C, and the coupling fluid outlet temperature decreases from 155.6°C to 152.7°C. During transients, the vapor temperature follows closely the rate of decrease in the solution inlet temperature, and the dilute solution and coupling fluid outlet temperature lag behind. As explained previously, this delayed response is due to the thermal capacitance effects in the propagation of input perturbations through the desorber.

4.4.3.4. Concentration variation

The responses of the desorber concentrations to an increase (Plot A) and decrease (Plot B) in the ambient temperature are presented in Figure 23. In general, the refrigerant vapor concentration decreases and the dilute solution concentration increases due to an increase in the

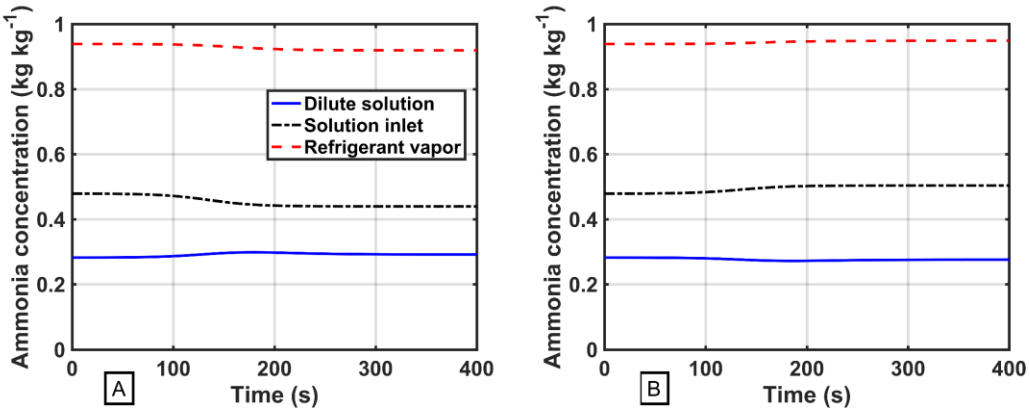

Figure 23: Response of desorber concentrations to an increase (A) and decrease (B) in ambient temperature.

ambient temperature. A decrease in the ambient temperature results in an increase in the refrigerant vapor concentration and a decrease in the dilute solution concentration.

The response of the desorber concentrations to an increase in the ambient temperature is shown in Plot A of Figure 23. The refrigerant vapor concentration decreases from 0.9387 kg kg^{-1} to 0.9191 kg kg^{-1} and the dilute solution concentration increases from 0.2826 kg kg^{-1} to 0.2922 kg kg^{-1}. The refrigerant vapor concentration decreases because of the increase in the vapor outlet temperature, which causes more water to change phase to vapor. The decreased mass flow rate and lower ammonia concentration of the vapor-phase lead to higher ammonia concentration in the liquid phase. During the transient period, the liquid concentration exceeds its final steady-state value, reaching a peak value of 0.2987 kg kg^{-1} before settling at its new equilibrium position. This response is due to the rise in component pressure preceding the rise in the dilute solution temperature.

Plot B of Figure 23 presents the time-evolution of the desorber concentrations due to a decrease in the ambient temperature. The refrigerant vapor concentration increases from 0.9387 kg kg^{-1} to 0.9487 kg kg^{-1} and the dilute solution concentration decreases from 0.2826 kg kg^{-1} to

0.2760 kg kg^{-1}. The increase in refrigerant vapor concentration is due to its decreased temperature. The increased vapor mass flow rate and concentration then lead to the decrease in the dilute solution concentration. Similar to the previous case, the dilute solution concentration overshoots its steady-state value, reaching a minimum value of 0.2725 kg kg^{-1}. This response is due to the decrease in dilute solution temperature lagging behind the decrease in component pressure.

An increase in ambient temperature results in a reduction in performance due to reduced vapor concentration and flow rate. Although the heat transfer rates of the system decrease following this change, the decrease in refrigerant flow rate and concentration negatively impact the refrigerant stream and the cooling capacity of the complete absorption system. Conversely, a decrease in the ambient temperature results in increased purity and mass flow rate of the refrigerant vapor. However, the desorber heat transfer rates also increase, leading to an increase in the required heat input into the system. Using these results, control algorithms can be developed to adjust tunable parameters such as solution flow rate and coupling fluid inlet temperature to maintain desired performance for a range of operating conditions.

5. CONCLUSIONS AND RECOMMENDATIONS

5.1 Conclusions

In this work, a detailed, physics-based dynamic model was developed to study the transient behavior of a small-scale ammonia-water desorber. A finite volume method was used to model the branched-tray desorber, with CVs placed around each desorber tray. The upwinding differencing scheme was used to integrate the mass, species, and energy continuity equations over each CV, resulting in a set of differential algebraic equations that define the system. Special considerations were used to account for the zeotropic ammonia-water solution and the counter-flow of the solution liquid and vapor. Geometric and heat transfer parameters are representative of those studied by Delahanty (2015) and Keinath *et al.* (2015). To solve the system of equations, the *ode15s* stiff DAE solver built-in to MATLAB® (Mathworks, 2016) was used. The results of the steady-state models validated the modeling assumptions. Simulations were performed for varying solution inlet mass flow rates, coupling fluid mass flow rates, coupling fluid inlet temperatures, and ambient temperatures to understand the steady-state performance at both on- and off-design conditions, and resulted in good agreement with the literature for the steady-state temperature profiles and heat transfer rate (Delahanty, 2015).

Analysis of the start-up cases revealed the large transients that occur when the desorber is initialized from room-temperature conditions and the coupling fluid inlet temperature is increased to its operating value of 180°C. Due to the lag between the increase in coupling-fluid and solution-side temperatures, the desorber experiences a period of transients where the heat transfer rates exceed their design steady-state conditions, leading to increased vapor generation. Due to the open-loop nature of the model presented in this study, accurate time constants could not be obtained. However, the range of simulations conducted showed the variation in possible responses of the

desorber and can be used as a baseline for the evaluation of future transient profiles once integrated into a system model.

Lastly, a series of transient perturbation cases were analyzed to evaluate the dynamic response of the desorber to changes in the design conditions. Simulations of perturbations in operating conditions were performed in which the desorber experienced a change from its design operating conditions by either increasing or decreasing the solution inlet mass flow rate, coupling fluid inlet temperature, or ambient temperature. The results of these simulations show the flexibility, accuracy, and efficiency of the detailed dynamic desorber model developed in this study. This model can be incorporated into a larger system model and assist in the evaluation of detailed and accurate system dynamics, as well as the development of robust control algorithms to improve the performance of small-scale ammonia-water absorption systems.

5.2 Recommendations

The models developed in the present study had the objective of investigating component behavior during start-up and in response to perturbations from the design conditions in an open-loop manner. The largest improvement on the work presented in this study would be the integration of the model into an overall ammonia-water absorption system model. This integration will provide a well-established source for the solution inlet property ramp times for given coupling fluid ramping times. Results from these larger system models will aid in the validation of the range of simulations presented in this study.

The integration of the desorber model into the system model will require further improvements in the computational efficiency of the desorber model. This will require development and validation of the reduced-order modeling techniques described in this study.

The complete desorber component also typically includes an analyzer and rectifier, which further aid in refrigerant generation and purification. Modeling of these subsections of the complete desorber will improve the accuracy of the present model, as well as the future development of the complete dynamic system model.

The heat transfer coefficients and tray efficiencies were kept constant at their design conditions in all analyses. In the future, temporally and spatially variable heat transfer coefficients can be included to improve the accuracy of the model. Time-dependent tray efficiency should also be investigated to improve model accuracy. Heat transfer between the wall and vapor was neglected in this work. Investigation into this heat transfer mechanism should be investigated in future models to determine its significance.

PART II

Optimal Control of an Electric Vehicle Cabin Air Conditioning System

6. INTRODUCTION

6.1 Overview

It is estimated by the International Energy Agency that by 2030 the global stock of electric vehicles (EVs) will surpass 130 million vehicles, up from the stock of 3.7 million vehicles in 2017 (IEA, 2018). The rise of the electric vehicle presents some unique challenges in the realm of vehicle cabin cooling and the comfort of the vehicle's occupants. Instead of using work from the combustion engine to drive the compressor, energy must be drawn from the batteries to condition the vehicle cabin. Especially in times of extreme ambient conditions, the energy required to acclimatize the cabin can significantly reduce the range of battery electric vehicles. As customers will not accept a reduction in performance with this new form of mobility, research must be undertaken into the most efficient manner of controlling the electric vehicle's cabin air conditioning (AC) system.

In the present work, the optimal control of an electric vehicle's air conditioning system is presented. The comfort of the passenger(s) is considered via a targeted cabin temperature, limitation on the CO_2 concentration in the cabin, and tracking of the cabin humidity level. By approaching the problem using optimal control theory, it is possible to achieve the desired cabin state while reducing the energy consumption of the thermal system. This will enable range extension of the electric vehicle while maintaining the high level of user comfort that consumers have come to expect.

In the following sections, the general topics of vehicle climate conditioning, including differences between EVs and internal combustion engine vehicles (ICEVs), and control techniques are introduced.

6.2 Climate conditioning in vehicles

Climate conditioning in automobiles refers to the maintaining of targeted cabin conditions through the use of a powertrain-driven air conditioning and heating cycle. These targeted conditions can be achieved, in general, in one of two ways: a manual system or using an automatic climate control system. In the simpler manual system, the occupant of the vehicle sets a constant air system blower speed and desired air temperature range, usually on a blue-to-red color-coded scale, exiting the vents using the control panel in the cabin. Although a simple and inexpensive system, the manual climate conditioning method is less efficient and can require intermediate adjustment by the user to maintain a comfortable cabin environment.

By comparison, a climate control system takes a target temperature input from the vehicle occupant and, using a variety of sensors, such as cabin temperature, humidity, solar load, and so on, adjusts the AC system compressor output, blower speed, distribution and mixing flaps. Adjustment of these inputs is performed in a manner that achieves and maintains the target cabin in the quickest and most efficient manner possible.

In comparison to climate control in buildings and other stationary applications, the modeling and control of automobile AC systems present some unique challenges. For example, the conditioned volume is much smaller, but the vehicle cabin is often exposed to more extreme changes in external conditions and internal starting conditions than in stationary applications. The solar load through the various windows is also more pronounced in automotive applications (Großmann, 2013)**.**

In order to accurately adjust the control parameters within the system, the climate control system must have access to a simplified representation of the physics present within the vehicle cabin and the air conditioning system. Background of these modeling topics are presented in the

following sections, along with the differences between model applications in electric and internal combustion engine-powered vehicles.

6.2.1 Air conditioning system modeling

As mentioned previously, climate conditioning in automobiles is performed using a vapor-compression air conditioning loop coupled to the cabin air system. Figure 24 presents a common automotive AC system. In its most basic configuration, the AC loop consists of an evaporator, compressor, condenser, accumulator, and an expansion valve. A synthetic refrigerant, commonly R134a, runs through the loop as the working fluid. A mixture of recirculated cabin air and fresh air is blown over the evaporator by an automotive blower fan, cooling the air entering the cabin.

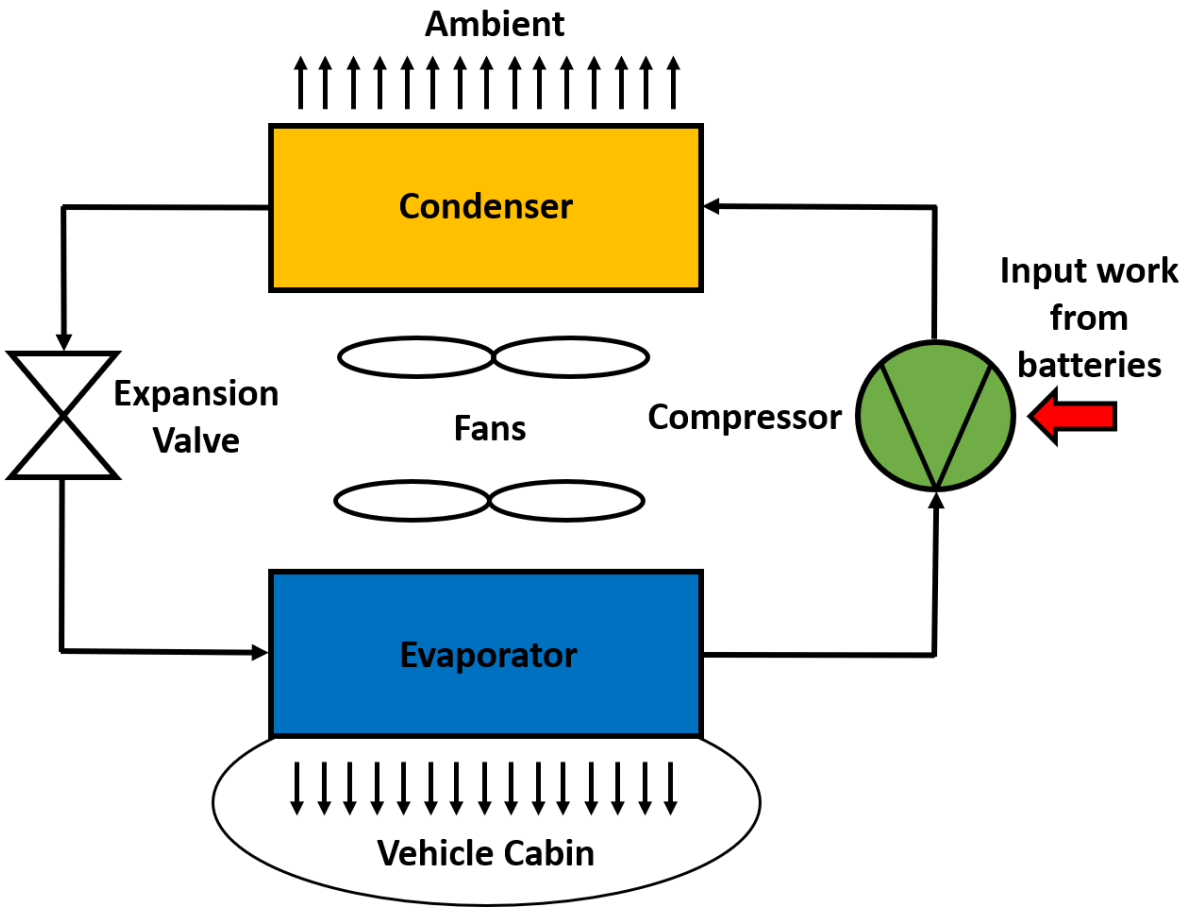

Figure 24: Schematic of a common automotive AC system.

The compressor is driven by the engine via a belt in a combustion engine powered vehicle or, as analyzed in the present work, using energy drawn from the electric vehicle's battery pack.

Modeling of the air conditioning system can be performed on a spectrum ranging from complex system models that include individual component performance, to more generalized, system-level models that consider the larger performance of the AC cycle. It has been shown in Farzaneh and Tootoonchi (2008); Khayyam *et al.* (2011); Khayyam (2013) that the simplified system-level models are sufficient to capture the dynamics of the vehicle AC system for control scheme development. In these studies, the authors use a first law efficiency, also referred to as a Coefficient of Performance (COP), to relate the required work to be input into the AC compressor and the cooling load provided by the evaporator. Such models are useful when considering the effect the AC system has on the state of the cabin, not the detailed states of the refrigerant-side of the AC cycle.

6.2.2 **Cabin modeling**

A vehicle cabin model, at its most simple, gives a relationship for the exchange of air between the automobile air system and cabin, the interior surface temperature of the cabin, the bulk cabin air conditions, the external conditions, including solar loading, and any occupants present in the cabin. These models can take complex forms, such as three-dimensional, computational fluid dynamics (CFD) and heat transfer models, as presented in Ling *et al.* (2013); Ye (2013); Danca *et al.* (2017); Singh and Abbassi (2018). These models are useful when evaluating detailed airflow of the ventilation entering the cabin from the air conditioning system, as well as region-by-region thermal state. However, when analyzing the general cabin and air conditioning system performance and control, these three-dimension models are too complex and slow to be useful.

It has been shown in Khayyam *et al.* (2011); Marcos *et al.* (2014); Lee *et al.* (2015); Torregrosa-Jaime *et al.* (2015), that when evaluating larger system performance, simplified cabin models provide enough accuracy to capture the general dynamics of the system. These lumped-parameter models simplify the cabin by combining all cabin thermal mass in contact with the internal air, such as the seats and dashboard, into a single, "lumped" mass. The only other portion of the cabin assumed to have thermal inertia is the cabin air, which is assumed to be homogeneous. Thermal loading due to solar radiation absorbed by the vehicle roof, and absorbed by and transmitted through the windows are treated with varying levels of complexity.

In this work, the added elements considered, on top of the bulk temperature of the cabin, are the humidity and CO2 concentration in the cabin air. These two factors play a significant role in the performance of the air conditioning system and the comfort of the passengers in the cabin.

6.3 Climate control

In order to maintain the target conditions in the cabin while minimizing the energy use of the system, a climate control system must be utilized. In the literature, researchers have implemented vehicle climate control schemes with varying degrees of control system complexity and overall thermal system detail.

Khayyam *et al.* (2011) employed a proportional-integral-derivative (PID) controller tuned using a neural network to limit the energy use of an internal combustion engine-powered vehicle air conditioning system. A targeted cabin air temperature was maintained by the system through the adjustment of the AC system compressor set point and blower flowrate, along with stepper-control of fresh air and recirculation gates to maintain comfortable CO_2 and humidity levels. The system was shown to reduce energy use in comparison to a manually-tuned PID control system.

A number of researchers have employed fuzzy logic controllers to efficiently control vehicle AC systems. Fuzzy logic control systems utilize a range-to-point or a range-to-range control system where ranges of input variables (e.g. “high”, “medium”, “low” cabin temperature) are mapped to a range of control variables (e.g. “fast”, “medium”, “slow” compressor speed) in an if-then manner (Bai *et al.*, 2006).

An HVAC system optimized fuzzy controller incorporating considerations for thermal comfort of the passengers of an ICEV was presented by Farzaneh and Tootoonchi (2008). The parameters of the fuzzy controller were optimized using a genetic algorithm. Thermal models of both the vehicle cabin and HVAC system were utilized.

Ibrahim *et al.* (2012) developed a partial-differential (PD) fuzzy logic-based temperature and humidity control strategy for an EV heating, ventilation, and air conditioning (HVAC) system. The authors used a three input (cabin temperature error, cabin temperature error change, and cabin relative humidity) and three output (heater bypass gate, outside/recirculated air mixing gate, and blower speed) to achieve and maintain the target cabin temperature and relative humidity range as fast as possible. However, system energy use is not minimized as the AC evaporator and heater are given constant heat inputs.

Khayyam (2013) introduced a more complex, fuzzy controller for an ICEV air conditioning system that employed a “look-ahead” element to anticipate road condition demands and adapt the membership functions of the controller accordingly. By controlling the AC compressor, blower, fresh-air, and recirculation gates, the authors showed that the system could better reduce energy consumption compared to a fuzzy ordinary controller while maintaining a comfortable temperature in the cabin.

Finally, optimal control methods have been evaluated in the literature for the efficient control of vehicle AC systems. Optimal control refers to the formulation of a control strategy that seeks to dynamically optimize a system given a set of constraints on the state and control variables. The solution to a given set of differential equations is deemed optimal if it minimizes a given cost function, which is a function of the path and control variables (Bryson, 1996).

Huang *et al.* (2016) presented a set of optimal energy-efficient predictive controllers for the control of ICEV AC systems. All controllers model and control the AC system and its individual components on a detailed level, but the control system does not consider the thermal effects of the cabin, only the output conditions of the evaporator and the energy consumption of the system. The controllers are evaluated using simulations and experiments compared to a conventional on/off controller to prove their energy-saving capabilities. Zhang *et al.* (2016) evaluated and presented a similar optimal control system for an ICEV AC system, also without considering the thermal effects of the cabin.

He *et al.* (2018) developed a model predictive control (MPC) framework to minimize the AC energy use of an electric bus AC system using three forecasted approaches for the variation in the number of passengers, all while maintaining the cabin temperature of the bus within a comfortable regime. The authors showed that the developed prediction and optimal control schemes were able reduce the system's energy use markedly over a rule-based control method.

Schaut and Sawodny (2018, *under review*) developed a climate control scheme based on a linear-quadratic model predictive controller (MPC) for the HVAC system of a battery electric vehicle. The MPC seeks to reduce the energy consumption of the HVAC system while maintaining the thermal comfort of the vehicle passengers. To verify the effectiveness of this control model, the authors compared its performance with a non-linear optimization model and a simple on/off

benchmark control scheme. The optimization-based MPC successfully was able to minimize the system energy with comparable results to the non-linear optimal controller, but with significantly reduced computation time.

In the present work, a non-linear optimal control scheme for the air conditioning system for an electric vehicle is introduced. The control system seeks to limit the energy used by the thermal system while maintaining a given level of thermal comfort for passengers. The method introduced in the present work is based on the non-linear control model developed by Schaut and Sawodny (2018, *under review*), but includes modifications in the modeling of the cabin, system of equations, cost function formulation, and the test cases used to validate the applicability of the optimal control scheme. Also varying from the literature is the definition of the thermal comfort of the passengers, which is here determined by a target cabin temperature and maximum CO_2 concentration. Constraints are placed on intermediate states within the system, such as the evaporator outlet temperature and absolute humidity. Predictive data, such as variable solar radiation load and other ambient disturbances, are included to exhibit the robustness of the developed control scheme.

6.4 Outline

In order to solve the optimal control problem (OCP), mathematical models for the vehicle cabin and air system are developed, including definition of the cabin geometry, heat transfer parameters, and disturbance vectors. The nonlinear optimal control problem is then introduced, along with constraints on inputs and states. The system is evaluated using a diverse set of use-cases that include both dynamic and constant disturbances to represent a wide range of operation conditions an electric vehicle air conditioning system could be exposed to.

The structure of the present study is as follows. Chapter 2 outlines the mathematical formulation of the vehicle cabin and air conditioning system model. This includes the governing equations, assumptions, and development of the polynomial fits for the humid air property routines.

Chapter 3 presents the development of the optimal control program for implementation using the CasADi toolkit. This chapter also introduces the simple baseline controller for performance comparison to the non-linear optimal control model. The software used in the present study is also summarized.

Chapter 4 presents and discusses the results obtained from a range of representative test case simulations. First, the simulation parameters are summarized. Next, the results of the constant disturbances ("basic") use-cases are presented and discussed, including comparison to the results of the simple benchmark controller. Finally, the results of the "advanced" use-cases employing time-varying disturbances are presented and analyzed.

Finally, Chapter 5 summarizes the present work and provides recommendations for future development.

7. MATHEMATICAL MODELING

Before the control scheme can be developed, the climate conditioning system of the electric vehicle must first be modeled. The thermal system consists of two parts: the vehicle cabin and the air system, including the AC. Figure 25 presents an overview of the vehicle thermal system, including the disturbances (red, dotted), inputs (blue, solid), and the system variables (no border). In the following sections, the thermal models for the vehicle cabin and air system, broken down in their components, are presented.

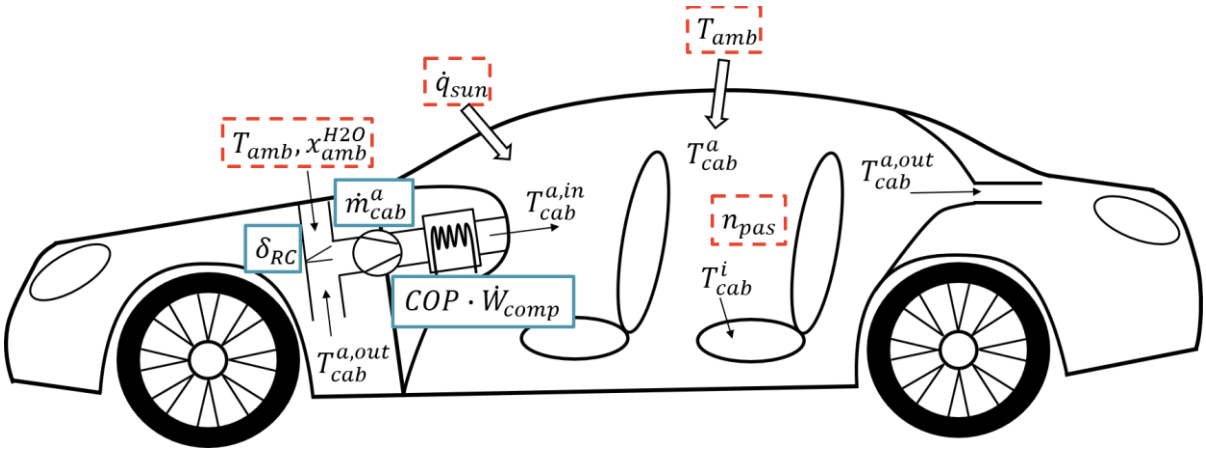

Figure 25: General vehicle diagram including cabin and air system.

7.1 Cabin

As mentioned earlier, the present work uses a 1-D, lumped-parameter approach to model the vehicle cabin, similar to those used by Marcos *et al.* (2014); Lee *et al.* (2015); Torregrosa-Jaime *et al.* (2015); Schaut and Sawodny (2018, *under review*). A representation of the cabin is given in Figure 26. As shown in the figure, air enters the vehicle cabin from vent outlets of the air system, mixes with the existing cabin air, which exchanges heat with the interior surfaces of the cabin. The cabin air state is further affected by the number of passengers and solar radiation. Finally, the air exits the cabin to recirculate into the vehicle air system. Four dynamic states exist

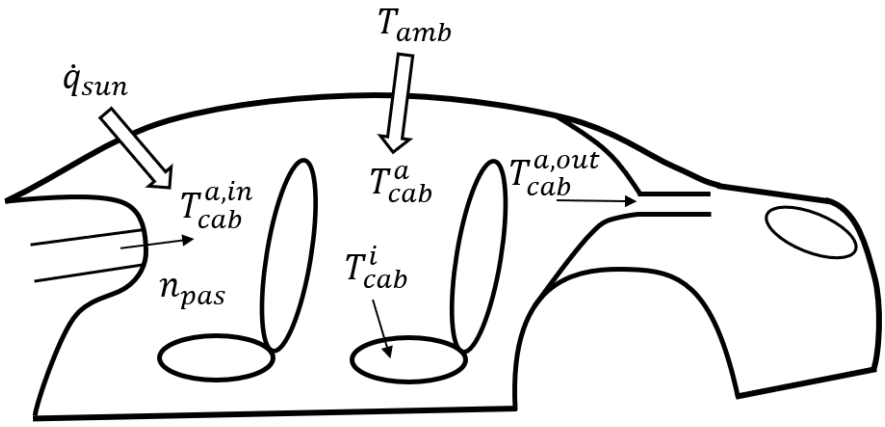

Figure 26: Schematic of the vehicle cabin.

in the cabin: the mean temperature of the interior surfaces T_{cab}^{i}, the mean temperature of the cabin air T_{cab}^{a}, the carbon-dioxide concentration in the cabin air x_{cab}^{CO2}, and, finally, the absolute humidity of the cabin air x_{cab}^{H2O}.

In the present work, the following assumptions were made when developing the cabin model:

- Only the interior surfaces of the cabin and the air contained therein are assumed to have thermal mass. These lumped masses are assumed spatially uniform, as is the carbon-dioxide concentration and absolute humidity of the cabin air.
- The sun is assumed to be directly overhead of the vehicle.
- Radiation heat transfer from the interior surfaces of the cabin to/from the cabin air is neglected, as the temperature differential is assumed small.
- Heat transfer between the cabin air, and the trunk and floor is neglected as those regions are assumed to be well insulated.
- The heat capacities, densities, and heat transfer coefficients are assumed constant.
- The pressure is assumed constant within the cabin and equal to the ambient pressure.

- No mass storage is assumed in the system. Any change in the mass flow rate within the air system is felt instantaneously and remains homogeneous throughout the system.

The thermal mass of the interior surfaces represents the contact area between the cabin air and the dashboard, seats, and other surfaces contained in the interior. These surfaces, however, do not include the windows and vehicle body panels that directly separate the cabin from the ambient air. The variation of the interior surfaces is given by

$$\dot{T}_{cab}^{i} = \frac{1}{C_{cab}^{i}}\left[\alpha_{cab}^{i} A_{cab}^{i}\left(T_{cab}^{a} - T_{cab}^{i}\right) + \tau_{sun}^{i} A_{sun}^{i} \dot{q}_{sun}\right], \tag{33}$$

where C_{cab}^{i} is the heat capacity of the interior. The interior surfaces exchange heat with the cabin air via convection, where α_{cab}^{i} represents the convective heat transfer coefficient with the cabin air, and A_{cab}^{i} is the sum area of the interior surfaces in contact with the cabin air. The interior surfaces of the cabin gain heat via the specific solar radiative heat flux $\dot{q}_{\mathrm{sun}}$, but the total solar radiation load is not transmitted into the vehicle cabin due to the transmissivity of the EV's windows τ_{sun}^{i} and the effective area of the interior surface "visible" to the sun A_{sun}^{i}, which are functions of the relative position of the vehicle and the sun.

The variation in temperature of the cabin air is given by

$$\dot{T}_{cab}^{a} = \frac{1}{c_{cab}^{a} V_{cab}^{a} \rho_{cab}^{a}}\left[n_{pas}\dot{Q}_{pas} + \dot{m}_{cab}^{a} c_{cab}^{a}\left(T_{cab}^{a,in} - T_{cab}^{a,out}\right) + U_{bod} A_{bod}\left(T_{amb} - T_{cab}^{a}\right) + \alpha_{cab}^{i} A_{cab}^{i}\left(T_{cab}^{i} - T_{cab}^{a}\right)\right], \tag{34}$$

where c_{cab}^{a} is the specific heat capacity of the cabin air, V_{cab}^{a} is the volume of the air in the cabin, and ρ_{cab}^{a} is the density of the cabin air. The occupants within the vehicle contribute heat to the cabin air at a rate of $\dot{Q}_{pas}$ per passenger, with n_{pas} being the number of passengers. The heat input into the system due to the air blown into the cabin at a mass flow rate of $\dot{m}_{cab}^{a}$ is quantified using the temperature difference between the cabin inlet and outlet air $T_{cab}^{a,in}$ and $T_{cab}^{a,out}$. The expression

for cabin outlet air temperature is explored in a later section. Heat transfer between the cabin air and the ambient air is calculated using the overall heat transfer coefficient U_{bod} and the overall heat transfer area A_{bod} of the vehicle body, and the temperature difference between the cabin air and the ambient air T_{amb}.

The changes in carbon-dioxide concentration and absolute humidity of the cabin air are determined via mass balance and are given by equation 35 and equation 36, respectively (Großmann, 2013)

$$\dot{x}_{cab}^{CO2} = \frac{1}{V_{cab}^{a}\rho_{cab}^{a}}\left[n_{pas}\dot{m}_{pas}^{CO2} + \dot{m}_{cab}^{a}\left(x_{cab}^{CO2,in} - x_{cab}^{CO2} \right) \right] \tag{35}$$

$$\dot{x}_{cab}^{H2O} = \frac{1}{V_{cab}^{a}\rho_{cab}^{a}}\left[n_{pas}\dot{m}_{pas}^{H2O} + \dot{m}_{cab}^{a}\left(x_{cab}^{H2O,in} - x_{cab}^{H2O} \right) \right] , \tag{36}$$

where $x_{cab}^{CO2,in}$ and $x_{cab}^{H2O,in}$ represent the carbon-dioxide concentration and absolute humidity of the inlet air entering the cabin from the air system. The passengers are also sources of both carbon-dioxide and water vapor, and their contributions are denoted by $\dot{m}_{pas}^{CO2}$ and $\dot{m}_{\mathrm{pas}}^{H2O}$, respectively. Both equations assume that the carbon-dioxide concentration and absolute humidity of the air exiting the cabin are equal to the mean values of the cabin air

$$x_{cab}^{CO2,out} = x_{cab}^{CO2} \;;\; x_{cab}^{H2O,out} = x_{cab}^{H2O} \quad .$$

7.1.1 Cabin outlet temperature

When modeling the outlet temperature of the vehicle cabin, a number of analogies have been presented in the literature. Nitz and Hucho (1979) proposed that the cabin can be treated as a heat exchanger with a heat capacity rate ratio of zero, resulting in a cabin outlet air temperature defined by

$$T_{cab}^{a,out} = T_{amb} + \left(T_{cab}^{a,in} - T_{amb}\right)\exp\left(-\frac{U_{bod}A_{bod}}{\dot{m}_{cab}^{a}c_{cab}^{a}}\right) . \quad (37)$$

The model proposed by Nitz and Hucho (1979) was employed by Schaut and Sawodny (2018, *under review*) to calculate the temperature of the air exiting the vehicle cabin.

Frank (1971) put forward that the ratio of the temperature of the air entering the cabin to the mean cabin air temperature is equal to the ratio of the mean cabin air temperature to the cabin outlet air temperature, with all temperatures using the ambient temperature as the reference temperature. With some rearranging, the resulting temperature of the air leaving the cabin is obtained and given by

$$T_{cab}^{a,out} = T_{amb} + \frac{\left(T_{cab}^{a} - T_{amb}\right)^2}{\left(T_{cab}^{a,in} - T_{amb}\right)} . \quad (38)$$

In addition to the two equations presented above, it can also be assumed that, either, the outlet cabin air temperature is an average between the mean cabin interior surface temperature and the mean cabin air temperature, or equal to the mean cabin air temperature, as given by

$$T_{cab}^{a,out} = \frac{\left(T_{cab}^{a} + T_{cab}^{i}\right)}{2} \quad (39)$$

$$T_{cab}^{a,out} = T_{cab}^{a} . \quad (40)$$

It needs to be noted that both equation 37 and equation 38 assume zero effect on the cabin from solar radiation. However, in the present work, solar radiation does strongly affect the thermal state of the cabin, as is often the case during operation of an air conditioning system with high ambient temperatures. This effect is separately accounted for in the $\tau_{sun}^{i}A_{sun}^{i}\dot{q}_{sun}$ term of equation 33. Figure 27 presents a comparison of the cabin mean air, interior surface, and outlet air temperatures during a cool down of the vehicle cabin from a heat-soaked condition of 60°C. All

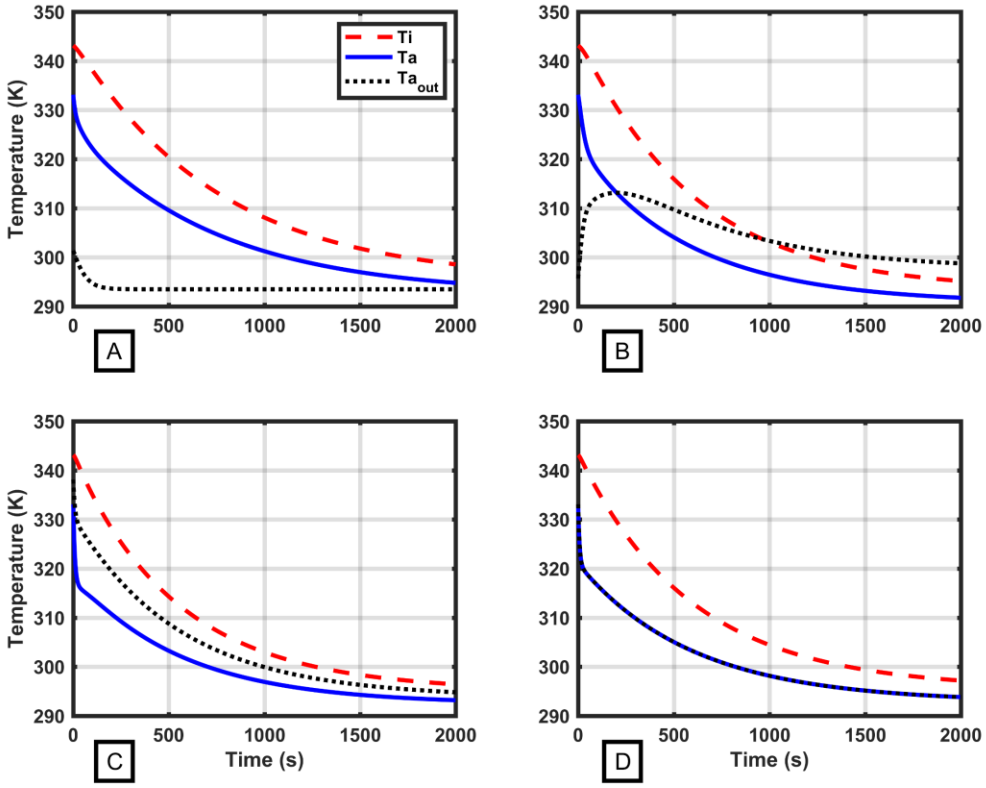

Figure 27: Comparison of cabin temperatures for various outlet air temperature equations: (A) Nitz and Hucho (1979), (B) Frank (1971), (C) average of cabin temperatures, and (D) equal to mean cabin air temperature.

cabin parameters, air system variables, ambient conditions, and initial conditions are kept constant between all four trials. The only change between the plots is the expression used for the cabin outlet temperature. Plot A presents the results using the expression according to Nitz and Hucho (1979), Plot B according to Frank (1971), Plot C using the average temperature expression, and, finally, Plot D using the assumption that the outlet air temperature is equal to the mean cabin air temperature.

As can been seen in Plot A, the equation proposed by Nitz and Hucho (1979) consistently underestimates the exit temperature of the air leaving the cabin when compared to realistic AC system operation at high ambient temperatures. Given the heat exchange analogy employed by the

authors, the results can be interpreted to mean not as much heat is being transferred from the entering air to the bulk air in the cabin before the air exits the cabin, cooling the cabin at a relatively slower rate than would be expected. Thus, this estimation of the outlet air temperature is deemed inaccurate for the cooling condition explored in this work.

Based on observations, the expression proposed by Frank (1971) (Plot B) represents the most realistic approximation for the cabin outlet temperature while cooling of the cabin is taking place. For the majority of the cooling period of the cabin, the outlet air temperature remains above the mean cabin air temperature and, as steady-state is approached, above the mean interior surface temperature as well. The period in which the outlet temperature is below the mean cabin temperatures occurs when both the ambient and inlet air temperatures are greater than the heat-soaked cabin air. Thus, not as much heat is pulled from the inlet air due to the contribution of the surroundings. Cooling is faster during this period, but slows as the mean cabin air temperature approaches and passes below the ambient temperature. More heat is then pulled from the inlet air to cool the cabin, as well as the outlet air being heated by the warmer ambient air as it returns to the air system.

Given these observations and the relative similarities between Plot B and the average and mean cabin outlet air temperature plots presented in Plot C and D, equation 38, as proposed by Frank (1971), will be used from this point forward to model the temperature of the air exiting the cabin.

7.2 Air system

The air system takes a mixture between the recirculated air from the cabin and fresh air from the surroundings, and, using an evaporator connected to the air conditioning system, cools the air entering the cabin. The model employed in the present work is based on the component

model employed by Schaut and Sawodny (2018, *under review*). A representation of the air system is presented in Figure 28. Within the air system, the climate control system presented later can adjust the position δ_{RC} of the recirculation flap, the mass flow rate of air $\dot{m}_{cab}^{a}$ via the power supplied to the blower, and the power supplied to the AC system compressor $\dot{W}_{\mathrm{comp}}$, which determines the cooling rate of the evaporator. The modeling of these three elements is explored in the following sections.

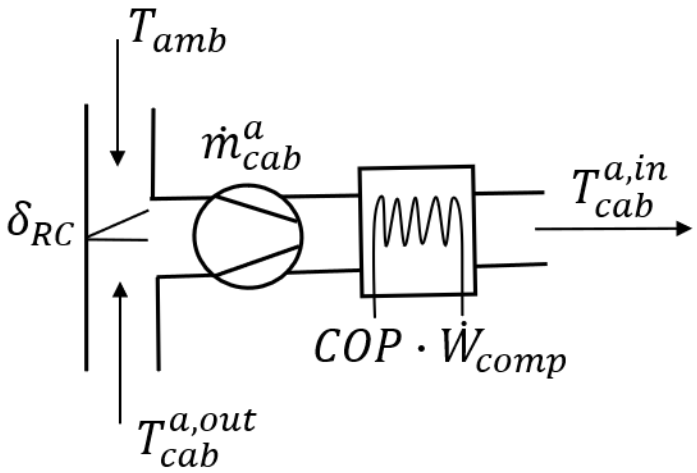

Figure 28: Schematic of vehicle air system consisting of the recirculation flap, the blower, and the evaporator.

7.2.1 Recirculation flap

The recirculation flap within the air system controls the mixture of recirculated air to fresh air entering the blower and evaporator. The flap position varies from 0 to 1, where 0 represents full fresh air operation and 1 represents full recirculation mode. The recirculated air has the properties of the air exiting the cabin: $T_{\mathrm{cab}}^{a,out}$, x_{cab}^{CO2}, and x_{cab}^{H2O}. The properties of the air after the recirculation flap, and entering the blower and evaporator are given by

$$T_{evap}^{in} = \delta_{RC} T_{cab}^{a,out} + \left(1-\delta_{RC}\right) T_{amb} \tag{41}$$

$$x_{evap}^{CO2,in} = \delta_{RC} x_{cab}^{CO2,out} + \left(1-\delta_{RC}\right) x_{amb}^{CO2} \tag{42}$$

$$x_{evap}^{H2O,in} = \delta_{RC} x_{cab}^{H2O,out} + \left(1-\delta_{RC}\right) x_{amb}^{H2O} \quad , \tag{43}$$

where the carbon-dioxide concentration and absolute humidity of the ambient air are given by x_{amb}^{CO2} and x_{amb}^{H2O}, respectively.

7.2.2 Blower

The blower determines the mass flow rate of the air in the air system and entering the cabin. The power consumed by the blower is approximated by

$$P_{bl} = a_{bl,1} + a_{bl,2} \left(\dot{m}_{cab}^{a}\right)^2 \quad , \tag{44}$$

where the blower coefficients $a_{\mathrm{bl},1}$ and $a_{\mathrm{bl},2}$ are determined for a 12V blower from Abb. 3.5 of Großmann (2013).

7.2.3 AC system

The AC system cools the air entering the cabin through connection to the air system via an evaporator. The enthalpy of the air entering the evaporator $h_{\mathrm{evap}}^{a,in}$ is a function of the air temperature and absolute humidity exiting the recirculation flap, as given by

$$h_{evap}^{a,in} = h^{a}\left(T_{evap}^{a,in}, x_{evap}^{H2O,in}, p\right) , \tag{45}$$

where p is the pressure of the air within the system. The development of the surface fits for the humid air properties employed in the air system are explored later in Section 7.4. The enthalpy of the air exiting the evaporator $h_{\mathrm{evap}}^{a,out}$ is determined by

$$h_{evap}^{a,out} = h_{evap}^{a,in} - \frac{COP \cdot \dot{W}_{comp}}{\dot{m}_{cab}^{a}} \quad , \tag{46}$$

where COP is the coefficient of performance of the AC system, and $\dot{W}_{comp}$ is the power supplied to the AC system compressor. The $COP \cdot \dot{W}_{\text{comp}}$ term represents the cooling power of the evaporator, $\dot{Q}_{\text{evap}}$.

As the carbon-dioxide concentration of the air does not change across the evaporator, the concentration of the air entering the cabin is same as the concentration after the recirculation flap, as given by

$$x_{evap}^{CO2,out} = x_{evap}^{CO2,in} \quad . \tag{47}$$

When the air exits the evaporator, it is assumed that the air is saturated, possessing a relative humidity of 100 percent. To support this assumption, Figure 29 presents the working regions of the evaporator on a psychrometric chart for humid air at standard atmospheric pressure (Ogawa, 2009). During standard operation, the range of possible temperatures and absolute humidity of the air entering the evaporator, shown in the region in red, lies above the possible outlet evaporator air temperature and absolute humidity, presented as the blue region, in the present work. For any absolute humidity entering the evaporator above 8 g·kg^{-1} dry air, the air exiting the evaporator is guaranteed to be saturated. In the case, however, the absolute humidity of the inlet drops below the 8 g·kg^{-1} dry air, as may be the case with very dry ambient conditions, the evaporator outlet air temperature is more likely to be cooled further. The cooler outlet air will hold the saturated absolute humidity of the outlet air below the inlet value, keeping the assumption valid in the majority of cases.

With the enthalpy and relative humidity of the air exiting the evaporator known, the temperature $T_{cab}^{a,in}$ and absolute humidity $x_{\text{cab}}^{H2O,in}$ at the outlet can be found, as given by

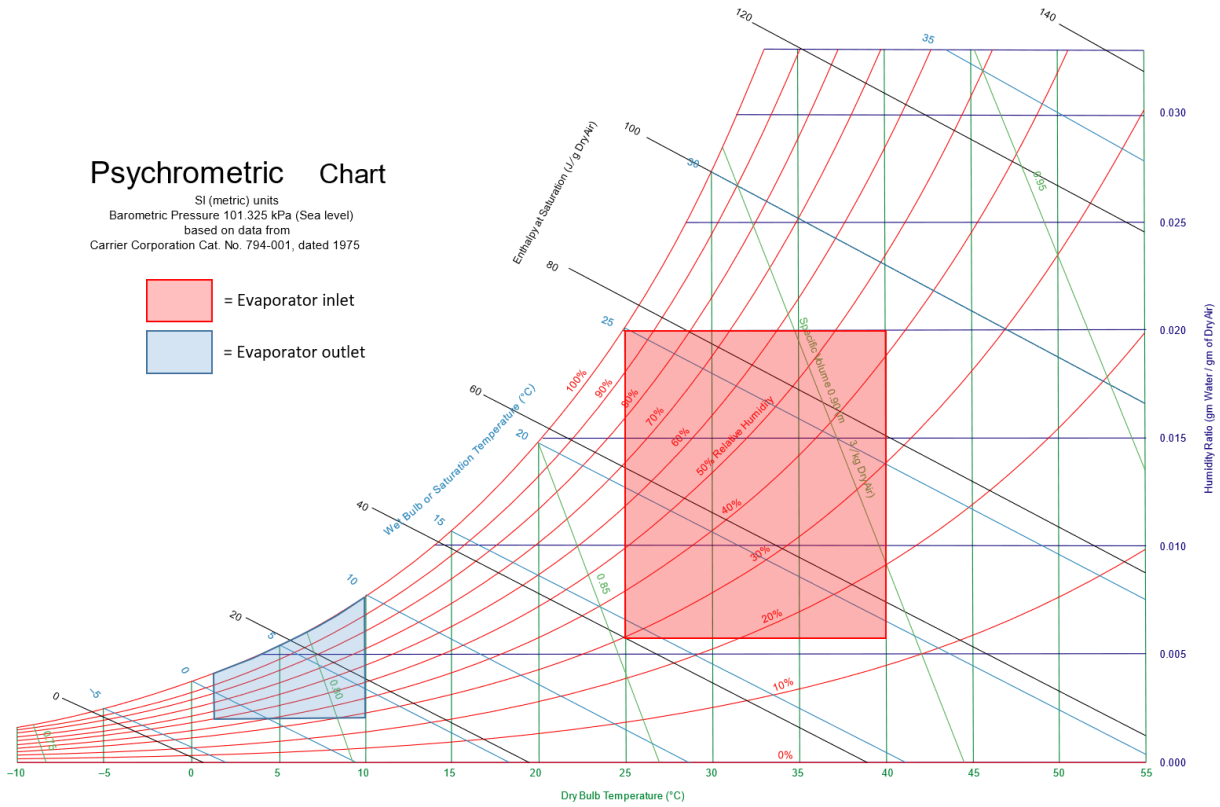

Figure 29: Psychrometric chart for humid air at atmospheric pressure. Red area highlights approximate operating range of the AC evaporator inlet and the blue area the approximate range of the evaporator outlet (Ogawa, 2009).

$$T_{cab}^{a,in} = T^{a}\left(h_{evap}^{a,out}, R=1, p\right) \tag{48}$$

$$x_{cab}^{H2O,in} = x^{H2O}\left(h_{evap}^{a,out}, R=1, p\right). \tag{49}$$

These properties are calculated using derived property surface fits as was similarly done for the enthalpy of the inlet. The derivation of these fits is presented in Section 7.4. With these two properties calculated, the air system is completely defined. In the next section, the cabin and air system equations are combined into a complete system of equations for the EV cabin conditioning system.

7.3 Overall model composition

By combined the individual components of the air system with the cabin model, an overall system of equations for the thermal system can be constructed. The differential and algebraic states, *x* and *z*, are defined, respectively, by

$$x = \left[T_{cab}^{i}, T_{cab}^{a}, x_{cab}^{CO2}, x_{cab}^{H2O} \right]^{T} \tag{50}$$

$$z = \left[T_{cab}^{a,out}, x_{evap}^{H2O,in}, T_{evap}^{a,in}, h_{evap}^{a,in}, h_{evap}^{a,out}, T_{cab}^{a,in}, x_{cab}^{H2O,in} \right]^{T} \ . \tag{51}$$

The system dynamics of the climate system are defined by

$$\dot{x} = f\left(x, z, u, d\right) \ , \tag{52}$$

where *f(x,z,u,d)* is given by

$$f\left(x,z,u,d\right) = \begin{bmatrix} \dfrac{1}{C_{cab}^{i}} \left[\alpha_{cab}^{i} A_{cab}^{i} \left(T_{cab}^{a} - T_{cab}^{i} \right) + \tau_{sun}^{i} A_{sun}^{i} \dot{q}_{sun} \right] \\ \dfrac{1}{c_{cab}^{a} V_{cab}^{a} \rho_{cab}^{a}} \left[n_{pas} \dot{Q}_{pas} + \dot{m}_{cab}^{a} c_{cab}^{a} \left(T_{cab}^{a,in} - T_{cab}^{a,out} \right) + U_{bod} A_{bod} \left(T_{amb} - T_{cab}^{a} \right) + \alpha_{cab}^{i} A_{cab}^{i} \left(T_{cab}^{i} - T_{cab}^{a} \right) \right] \\ \dfrac{1}{V_{cab}^{a} \rho_{cab}^{a}} \left[n_{pas} \dot{m}_{pas}^{CO2} + \dot{m}_{cab}^{a} \left(1 - \delta_{rc} \right) \left(x_{amb}^{CO2} - x_{cab}^{CO2} \right) \right] \\ \dfrac{1}{V_{cab}^{a} \rho_{cab}^{a}} \left[n_{pas} \dot{m}_{pas}^{H2O} + \dot{m}_{cab}^{a} \left(x_{cab}^{H2O,in} - x_{cab}^{H2O} \right) \right] \end{bmatrix} . \tag{53}$$

The third expression within equation 53 is determined by combining equations 35, 42, and 47 into a single equation.

The additional algebraic states *z* required to close the system defined are given by equations 38, 41, 43, and 46, as well as the surface fits for $h_{\text{evap}}^{a,in}$, $T_{\text{cab}}^{a,in}$, and $x_{\text{cab}}^{H2O,in}$ given by equations 45, 48, and 49. These equations are combined in the function *h(x,z,u,d)* given by

$$h(x,z,u,d)=\begin{bmatrix} T_{amb}+\dfrac{\left(T_{cab}^{a}-T_{amb}\right)^{2}}{\left(T_{cab}^{a,in}-T_{amb}\right)} \\ \delta_{rc}T_{cab}^{a,out}+\left(1-\delta_{rc}\right)T_{amb} \\ \delta_{rc}x_{cab}^{H2O}+\left(1-\delta_{rc}\right)x_{amb}^{H2O} \\ h^{a}\left(T_{evap}^{a,in},x_{evap}^{H2O,in},p\right) \\ h_{evap}^{a,in}-\dfrac{COP\cdot\dot{W}_{comp}}{\dot{m}_{cab}^{a}} \\ T^{a}\left(h_{evap}^{out},R,p\right) \\ x^{H2O}\left(h_{evap}^{out},R,p\right) \end{bmatrix} . \quad (54)$$

The input vector *u* defining the control variables of the system is defined by

$$u=\left[\delta_{RC},\dot{m}_{cab}^{a},\dot{W}_{comp}\right]^{T} , \quad (55)$$

and the disturbance vector *d* is given by:

$$d=\left[\dot{q}_{sun},T_{amb},x_{amb}^{H2O},n_{pas}\right]^{T} . \quad (56)$$

With these equations defined, a system of differential-algebraic equations (DAE) takes shape to define the climate conditioning system of the EV, due to the fact that the outlet temperature of the cabin defined by equation 38 depends on the inlet temperature.

7.4 Air property surfaces curve fits

In order to calculate the properties of the humid air present at different points in the air system, polynomial fits of the property surfaces for enthalpy of humid air as a function of temperature and absolute humidity, air temperature as a function of enthalpy and relative humidity, and absolute humidity as a function of enthalpy and relative humidity were created. These fits were employed at the inlet and outlet of the evaporator within the air system in order to close the DAE system of equations.

The polynomial fits were created using the humid air property routines contained within the CoolProp library (Bell *et al.*, 2014) and MATLAB®'s curve fitting toolbox (Mathworks, 2016). A wide range of anticipated air temperatures (-10 to 60°C), enthalpies (-1×10^4 to 3×10^5 J·kg^{-1}), relative humidity (5% to 100%), and absolute humidity (0 to 0.10 kg kg^{-1} dry air) were used in order to ensure the greatest possible accuracy of the resulting fits. Polynomial fits were selected as their accuracy was high enough while still enabling an output from the MATLAB® toolbox of an analytic, differentiable function for use in the system of equations. A summary of the three fits is presented in Table 9.

Table 9: Summary of the humid air property surface fits performed using the MATLAB® curve fitting toolbox.

Property Fit	Variable 1	Variable 2	Order of fit used	R-squared value
Enthalpy	Temperature	Absolute humidity	Poly21	1
Temperature	Enthalpy	Relative humidity	Poly55	0.9997
Absolute humidity	Enthalpy	Relative humidity	Poly44	0.9999

8. OPTIMIZATION AND CONTROL

In this chapter, the optimal control scheme for the electric vehicle climate control system is introduced. First, the optimal control model is introduced, including the required constraints on the model and the solver implementation. Then, the benchmark on-off control model used to validate the effectiveness of the optimal control scheme is presented. Finally, the software packages used in the present work are outlined.

8.1 Optimal control problem formulation

The optimal control problem is formulated in order to minimize the energy used by the EV climate control system. While minimizing the energy, the scheme must also meet the comfort requirement of the passengers by achieving the target cabin air temperature and limiting the carbon-dioxide concentration of the cabin air. In order to meet these goals, a non-linear, constrained optimal control problem (OCP) was defined. The OCP for the EV climate control system, featuring the objective function and constraints, takes the form

$$\min \quad J = \int_0^{t_{end}} J_u + J_c dt \tag{57}$$

$$\text{with} \quad J_u = \dot{W}_{comp} + a_{bl,1} + a_{bl,2}\left(\dot{m}_{cab}^{a}\right)^2 \tag{58}$$

$$J_c = S_{Tc}\left(T_{cab}^{a} - T_{goal}^{a}\right)^2 \tag{59}$$

$$\text{s.t.} \quad \dot{x} = f\left(x, z, u, d\right) \tag{60}$$

$$z = h\left(x, z, u, d\right) \tag{61}$$

$$x(0) = x_0 \tag{62}$$

$$x_{cab}^{CO2} \le x_{crit}^{CO2} \tag{63}$$

$$T_{evap,min}^{a,out} \le T_{evap}^{a,out}\left(x, u, z, d\right) \le T_{evap,max}^{a,out} \tag{64}$$

$$u_{\min} \le u \le u_{\max}\,, \tag{65}$$

where J is the total cost of the thermal system from time zero until the end of the simulation period t_{end}, J_u and J_c are the usable and comfort terms of the cost function, respectively, S_{Tc} is the penalty coefficient for cabin air temperature thermal comfort, T^a_{goal} is the target cabin air temperature, x_0 is the vector of initial conditions, x^{CO2}_{crit} is the critical level of the carbon-dioxide concentration of the cabin air, and the *max* and *min* subscripts denote the maximum and minimum values allowable for a given variable's state, respectively.

The objective (or cost) function J determines the "energy" used by the thermal system, which is minimized by the optimal controller. The energy use given by the air conditioning system cost function can be broken into two parts: 1) usable J_{u} and 2) comfort J_{c}. The usable portion consists of the first two terms of the function, representing the actual energy drawn by the AC compressor and air system blower during cabin climatization.

The cabin air temperature penalty term $S_{Tc}\left(T^a_{\text{cab}} - T^a_{goal}\right)^2$ within the cost function is the singular comfort energy term. It is employed to force the mean cabin air temperature down to a given target temperature. The cabin air temperature penalty term does not represent actual energy usage by the air conditioning system, but rather a thermal comfort condition for passengers that is an additional load on the system. Whether the cabin air temperature over- or undershoots the target temperature, the quadratic temperature error term ensures that the control scheme is penalized. The coefficient S_{Tc} determines the amplitude of the temperature penalty term. In the present work, this coefficient is sized such that temperature penalty is an order of magnitude larger than the usable energy term, ensuring that the target cabin temperature is met.

The non-linear dynamics of the cabin and the conditions throughout the air system are defined by $\dot{x}$ and z, which are determined using equations 53 and 54 (Section 7.3), respectively.

Constraints are placed on the non-linear state, component, and input vectors with equations 63, 64, and 65, respectively. These constraints are explained in detail in the following section.

8.1.1 Constraints

8.1.1.1. Carbon-dioxide concentration

The concentration of carbon-dioxide in the cabin air is limited by the health and safety of the occupants of the vehicle. As given in equation 35 (Section 7.1), the passengers add carbon-dioxide to the air, increasing the concentration steadily in excess of the starting ambient CO_2 concentration. In the present work, the critical limit of the carbon-dioxide concentration in the cabin is set at 0.001221 kg-CO_2 per kg-air, which is at the beginning of the room concentration range where drowsiness and reports of poor air quality can occur, according to the United States Occupational Safety and Health Administration (OSHA) (OSHA, 2017). The carbon-dioxide cabin air concentration constraint is given by

$$x_{cab}^{CO2} \leq x_{crit}^{CO2} \quad . \tag{66}$$

8.1.1.2. Evaporator outlet temperature

The outlet air temperature of the evaporator must be constrained in order to avoid icing at the low end and sufficient cooling at the upper end of the temperature range. The temperature restraint on the evaporator outlet is given by

$$T_{evap,min}^{a,out} \leq T_{evap}^{a,out} \leq T_{evap,max}^{a,out} \quad . \tag{67}$$

The evaporator outlet temperature is given by equation 48 (Section 7.2.3). In the present work, the outlet temperature is set to be 2°C at a minimum and 10°C at a maximum.

8.1.1.3. Control variables

The three control variables that are available for adjustment by the controller are the recirculation flap position δ_{RC}, mass flow rate of air driven by the blower $\dot{m}_{\mathrm{cab}}^{a}$, and the AC compressor power $\dot{W}_{\mathrm{comp}}$. These three variables are constrained within the optimal control problem in order to ensure that the solution is realistically achievable by the AC system. The control vector is, thus, restricted according to

$$u_{\min} \leq u \leq u_{\max} \quad , \tag{68}$$

where the maximum and minimum control vectors are similarly defined as in equation 55 (Section 7.3) with their respective constant maximum and minimum values.

The recirculation flap determines the mixture of fresh air to recirculated cabin air and is simply restricted to the continuous range between full recirculation mode at position 1 and full fresh air mode at position 0.

The mass flow rate of air is restricted on the bottom end to a mathematical zero position and a maximum flow rate on the top end representative of a standard vehicle ventilation system. The mass flow rate can never equal zero as this would lead to an infeasible condition for the enthalpy of the air exiting the evaporator, as defined by equation 46 (Section 7.2.3).

Lastly, the power provided to the AC compressor can lie at or continuously between zero and 3 kW. The *COP* for the AC cycle is assumed to be 2, which, as reported in Jabardo *et al.* (2002), is a conservative assumption for the efficiency of a modern automotive AC system and, thus, will give a low-end estimate for the energy consumption by the AC cycle. Given this assumed cycle efficiency, the maximum AC compressor power results in a maximum cooling load of 6 kW,

which is representative of a standard automotive AC evaporator (Jabardo *et al.*, 2002; Wang *et al.*, 2005).

8.1.2 Integration method and solver

In order to solve the optimal control problem, the direct multiple shooting method (Bock and Plitt, 1984) is employed using a fourth-order Runge-Kutta method to discretize the system. According to the direct multiple shooting method, the entire continuous horizon is first divided into N discrete control intervals, on which the input vector is defined. The state vector is then estimated at every grid point, with the initial state defined by the initial conditions. The trajectory of the state vector on each interval is then estimated using the fourth-order Runge-Kutta method, as defined by

$$\begin{aligned} k_1 &= f\left(x(t), \quad u(t), d, z(t)\right) \\ k_2 &= f\left(x(t) + k_1 \frac{dt}{2}, u(t), d, z(t)\right) \\ k_3 &= f\left(x(t) + k_2 \frac{dt}{2}, u(t), d, z(t)\right) \\ k_4 &= f\left(x(t) + k_3 dt, \ u(t), d, z(t)\right) \\ x(t+dt) &= x(t) + \frac{dt}{6}\left(k_1 + 2k_2 + 2k_3 + k_4\right) \ , \end{aligned} \tag{69}$$

where k_1 is the slope at the start of the time step dt, k_2 is the first estimate of the slope at the midpoint of the time step, k_3 is the second estimate of the slope at the midpoint using the first estimate, and k_4 is the estimate of the slope the endpoint. Using these four slopes, a weighted sum can be formulated to get the final state at the end of the time step $x(t + dt)$. To maintain continuity, the endpoint state of the previous interval is defined as the starting position of the next interval. Given this subdivided, discretized, and constrained horizon, the OCP is transformed into a non-linear program. The non-linear program is then solved using the IPOPT solver (Wächter and

Biegler, 2006), with the required derivatives provided to the solver by the CasADi toolkit (Andersson *et al.*, 2018).

8.2 Benchmark control model

A benchmark control method is used to validate the effectiveness of the optimal control strategy introduced in the present work. The cabin air temperature is controlled using a basic feedback controller, which seeks to reduce the difference between the mean cabin air temperature and the reference target air temperature by adjusting the power supplied to the AC compressor.

To begin the control process, the position of the recirculation flap must be determined. The CO_2 concentration of the cabin air is kept below the critical limit by changing the position δ_{RC} between maximum and minimum values. When the critical limit is met, the position is changed to favor fresh air, decreasing the carbon-dioxide concentration of the cabin air. When a given lower concentration limit is reached, the flap is returned to favor recirculated air. The lower limit in the present work is set at 1.25-times the ambient carbon-dioxide concentration. The recirculation flap position algorithm is summarized by

$$\delta_{RC}\left(t\right)=\begin{cases}\delta_{RC,max} & \text{for } x_{cab}^{CO2}<1.25\cdot x_{amb}^{CO2}\\ \delta_{RC,min} & \text{for } x_{cab}^{CO2}>x_{crit}^{CO2}\\ \delta_{RC}\left(t-dt\right) & \text{otherwise.}\end{cases} \tag{70}$$

Next, the controller determines the maximum and minimum allowable compressor power, respectively, using

$$\dot{W}_{comp,max}=\min\left(\dot{m}_{cab,max}^{a}\frac{\left(h_{evap}^{a,in}-h_{evap,min}^{a,out}\right)}{COP},\dot{W}_{comp,Lim}\right) \tag{71}$$

$$\dot{W}_{comp,min}=\dot{m}_{cab,min}^{a}\frac{\left(h_{evap}^{a,in}-h_{evap,max}^{a,out}\right)}{COP}\quad . \tag{72}$$

The evaporator inlet air enthalpy $h_{evap}^{a,in}$ is determined by equation 45 (Sect 2.2.3). The minimum and maximum evaporator outlet air enthalpy are predetermined given the evaporator out air limiting temperatures of 2°C and 10°C by

$$h_{evap,max}^{a,out} = h^a\left(T_{evap,max}^{a,out}, R=1, p\right) \tag{73}$$

$$h_{evap,min}^{a,out} = h^a\left(T_{evap,min}^{a,out}, R=1, p\right) \ . \tag{74}$$

With the maximum and minimum compressor power constraints known, the simple feedback controller can then be applied to the AC compressor power using

$$\dot{W}_{comp,FB} = a_{comp}\left(T_{goal}^{a} - T_{cab}^{a}\right) + \dot{W}_{comp,max} \quad , \tag{75}$$

where $\dot{W}_{\mathrm{comp,FB}}$ is the estimated AC compressor power to drive the mean cabin air temperature to the target temperature T_{goal}^{a}, and a_{comp} is a weighting coefficient for the mean cabin air temperature error. However, the feedback controller-determined compressor power may not exceed the compressor power limit $\dot{W}_{\mathrm{comp,Lim}}$ of 3 kW (as given in Section 8.1.1.3), nor be lower than the minimum compressor power determined by equation 72. The final AC compressor power, given the above constraints, becomes

$$\dot{W}_{comp} = \max\left(\dot{W}_{comp,FB}, \dot{W}_{comp,min}\right) \ . \tag{76}$$

Once the AC compressor power has be determined, the controller calculates the mass flow rate of the air. The feedback controller-determined mass flow rate $\dot{m}_{FB}^{a}$ to achieve the desired evaporator outlet temperature is determined by

$$\dot{m}_{FB}^{a} = \max\left[\min\left(\frac{COP\cdot\dot{W}_{comp,FB}}{h_{evap}^{a,in} - h_{evap,max}^{a,out}}, \dot{m}_{cab,max}^{a}\right), \dot{m}_{cab,min}^{a}\right] \ . \tag{77}$$

Given this desired level of air mass flow rate, the final applied air mass flow rate can be determined by

$$\dot{m}_{cab}^{a} = \begin{cases} \dot{m}_{FB}^{a} & \text{if} \quad \dot{m}_{cab,max}^{a} \cdot h_{evap}^{a,in} - COP \cdot \dot{W}_{comp} > h_{evap,\max}^{a,out} \cdot \dot{m}_{cab,max}^{a} \\ \dot{m}_{cab,max}^{a} & \text{otherwise.} \end{cases} \tag{78}$$

Equation 78 is applied in order to maintain an outlet air enthalpy (and, thus, temperature) that lies under the maximum outlet air enthalpy given by equation 73.

The system described above is comparable to those found in modern production vehicles. A similar control scheme was used as a baseline for comparison by Schaut and Sawodny (2018, *under review*).

8.3 Software packages

This section gives a brief introduction to the software packages used in the present work. These programs are used to model the vehicle air system and cabin, and solve the optimal control problem.

8.3.1 MATLAB®

MATLAB® (Mathworks, 2016) is a widely-used matrix-based platform useful for numerical and symbolic computing, and includes extensive libraries and toolboxes. The script-based program development allows for simplified model modification, debugging, and plotting.

8.3.2 Simulink™

Simulink™ (Mathworks, 2016) is an additional package within MATLAB® that provides a graphical programming platform using block diagrams for mathematical operations and is used typically for multi-domain simulations and model-based control design. Simulink also features the ability to import system elements from MATLAB® scripts and C-codes.

8.3.3 **CasADi & IPOPT**

For the solution of the nonlinear optimal control problem, a set of software is used within the MATLAB® platform. The CasADi toolkit (Andersson *et al.*, 2018) is an open-source tool for algorithmic differentiation and non-linear optimization. CasADi employs among other possible solvers, the IPOPT solver (Wächter and Biegler, 2006) to solve the established non-linear program.

8.3.4 **CoolProp**

CoolProp (Bell *et al.*, 2014) is a C++ library for mixture properties, pure and pseudo-pure fluid equations of state and transport properties, and high-accuracy psychrometric routines. Of specific importance to the present work is the library's humid air property routines, which are the basis for the curve-fitted air property equations described in Section 7.4.

9. RESULTS AND DISCUSSION

The results of the optimal control model for an electric vehicle air conditioning system are presented here. First, the simulation parameters are introduced, including a summary of the model constraints. Next, the results of the basic test cases with constant disturbance vectors are then introduced and are compared to the results of the simple, benchmark controller model. Lastly, the results of the advanced test cases with time-varying disturbance vectors are analyzed.

9.1 Simulation parameters

Table 10 presents the model parameters for the test cases. All parameters remain constant throughout all trials presented in this work.

The first section of Table 10 gives the constant air properties. The air volume of the cabin represents the volume of a sedan-sized automobile. The air density, specific heat capacity, and pressure are indicative of standard atmospheric conditions. The next section of parameters applies to the thermal mass of the interior surfaces of the cabin, including seats, dashboard, interior paneling, etc. The interior heat capacity is representative of the product of the average of the specific heat capacities for cotton, ABS plastic, and aluminum, and an approximate interior mass of 120 kg. The interior convective heat transfer conductance gives the estimated extent of convective heat transfer from the interior thermal mass to the cabin air. The value was selected, in combination with the body overall heat transfer conductance, to give a cool down of the cabin at full compressor power and maximum mass flow rate from a 60°C heat-soaked condition to the target temperature of 22°C in approximately 30 minutes given ambient conditions of 40°C and relative humidity of 40 percent. This cool down test of the air conditioning system is taken in the present work as benchmark scenario for the air conditioning control schemes.

Table 10: Summary of the constant cabin, ambient, and other simulation parameters.

Property	Nomenclature	Units	Value
Air volume	V_{cab}^{a}	m^3	2.4
Air density	ρ_{cab}^{a}	kg m^{-3}	1.2
Air specific heat capacity	c_{cab}^{a}	J kg^{-1} K^{-1}	1005
System pressure	p	Pa	1×10^5
Interior heat capacity	C_{cab}^{i}	J K^{-1}	144×10^3
Interior convective heat transfer conductance	$\alpha_{\text{cab}}^{i} A_{\text{cab}}^{i}$	W K^{-1}	180
Window transmissibility	τ_{sun}^{i}	-	0.6
Effective solar area	A_{sun}^{i}	m^2	1.3
Body overall heat transfer conductance	$U_{\text{bod}} A_{\text{bod}}$	W K^{-1}	90
Ambient CO_2 concentration	x_{amb}^{CO2}	kg CO_2 kg^{-1} air	5.8×10^{-4}
Passenger CO_2 output	$\dot{m}_{\text{pas}}^{CO2}$	kg CO_2 s^{-1}	1.39×10^{-5}
Passenger H_2O output	$\dot{m}_{\text{pas}}^{H2O}$	kg H_2O s^{-1}	2.08×10^{-5}
Passenger heat output	$\dot{Q}_{\text{pas}}$	W	100
Blower coefficient, 1	$a_{bl,1}$	W	150
Blower coefficient, 2	$a_{bl,2}$	J s kg^{-2}	2450
Coefficient of performance, AC system	COP	-	2

The window transmissibility determines the amount of thermal radiation transmitted via the vehicle's windows. The chosen value is indicative of treated, or tinted, automotive windows. The effective solar area of the interior is assumed based upon a solar vector coming from directly over the vehicle.

The vehicle body overall heat transfer conductance assumes an overall heat transfer coefficient of the body of 5 W m^{-2} K^{-1} and a body surface area of 18 m^2. As mentioned previously,

this term was adjusted with the interior convective heat transfer conductance to achieve the desired cooling time for the heat-soaked cabin.

The ambient carbon-dioxide concentration reflects a conservative estimate for CO_2 concentrations on roadways in an urban environment given an average atmospheric CO_2 level of 400 ppm (Gately *et al.*, 2015). The passenger CO_2, H_2O, and heat output rates were chosen based upon the standard output of an adult person as found in ASHRAE (2001). The two blower coefficient values are for a 12 V blower based on Fig. 3.5 of Großmann (2013). As mentioned previously, the coefficient of performance (*COP*) of the AC system was chosen based upon the results of Jabardo *et al.* (2002).

Table 11 summarizes the constraints placed on the control variables, state variables, and component variables in the present work for all test cases. A detailed discussion of the constraint values used in the present work can be found in Section 8.1.1.

For the following test cases, a final simulation time of t_{end} = 4000 seconds was used in order to allow state variables to settle to their approximate steady-state levels. The number of control intervals N was selected as 800, giving an interval length dt of 5 seconds. The mean computing time on a laptop with an Intel Core i7-7700HQ CPU with 2.80 GHz and 16 GB of RAM for the basic trials was 77.45 seconds to solve the optimal control problem.

Table 11: Summary of the constraints placed on the control, state, and component variables.

	Property	Nomenclature	Units	Min	Max
State Variables	Mean cabin air temperature target	T^{a}_{goal}	°C	22	
	Cabin air CO_2 concentration	x^{CO2}_{cab}	kg CO_2 kg^{-1} air	x^{CO2}_{amb}	1.221× 10^{-3}
Component Variable	Evaporator outlet air temperature	$T^{a,out}_{\text{evap}}$	°C	2	10
Control Variables	Recirculation flap position	δ_{RC}	-	0	1
	Air mass flow rate	$\dot{m}^{a}_{\text{cab}}$	kg s^{-1}	1 × 10^{-6}	0.15
	AC compressor power	$\dot{W}_{comp}$	kW	0	3

9.2 Basic test cases

This section presents the basic test case results of the optimal control scheme for an electric vehicle air conditioning system. For all simulations in this section, the disturbance vector is not time-varying. The optimal control problem solution is compared with that from the simple benchmark controller, with focus on the energy use of each control system and the time to achieve the desired cabin temperature. The disturbances and initial conditions for each test case are presented in Table 12.

Table 12: Disturbances and initials conditions for the basic test cases for the optimal controller and simple benchmark controller.

	Disturbances				Initial conditions	
Case	$\dot{q}_{sun}$ [W m^{-2}]	T_{amb} [°C]	x_{amb}^{H2O} [g H_2O kg^{-1} dry air]	n_{pas}	$T_{cab}^{i}(0)$ [°C]	$T_{cab}^{a}(0)$ [°C]
1	1000	30	13.7	1	50	40
2	800	40	19.0	1	70	60
3	650	40	19.0	1	50	45
4	650	40	44.5	1	50	45
5	650	30	13.7	1	50	40
6	650	30	13.7	4	50	40

Case 1 presents the scenario of a high solar radiation load on the vehicle cabin. This high solar radiation load also raises the initial mean cabin air and interior surface temperatures to elevated levels, referred to here as a heat-soaked condition, while the absolute humidity of the cabin remains at ambient levels to begin. Only the driver is present in the vehicle in this scenario. Case 2, similarly, presents the case of a high solar load, as well as elevated ambient and cabin starting conditions. Case 2 is considered in the present work as the benchmark test of the air conditioning control system. Ideally, the air conditioning system will be able to cool the cabin from this starting condition and at these external conditions to the target temperature in approximately 30 minutes. Cases 3 and 4 simulate the air conditioning of the cabin given a less elevated solar load and cabin starting conditions, but elevated ambient temperature and absolute humidity. The extreme humidity in case 4 results in an ambient relative humidity of approximately 90%, testing the limits of the air conditioning control systems. Finally, cases 5 and 6 present the effect of the number of occupants on the climate conditioning of a heat-soaked vehicle cabin.

Table 13 summarizes the results of the basic test cases for the optimally controlled air conditioning system in comparison to the simple feedback controller. As shown, the optimal

Table 13: Results of the basic test cases for the optimal controller and simple benchmark controller.

	Optimal controller			Simple controller			Optimal vs simple controller		
Case	J_u	J_c	t to T^a_{goal} [min]	J_u	J_c	t to T^a_{goal} [min]	Savings, J_u	Improvement, J_c	Improvement t to T^a_{goal}
1	0.66	5.58	10.17	0.78	5.87	10.31	-15.35 %	-5.06 %	-1.36 %
2	1.01	77.95	24.25	1.28	181.39	66.67	-21.05 %	-57.02 %	-63.63 %
3	0.89	8.46	11.67	1.26	31.35	50.23	-29.63 %	-73.01 %	-76.77 %
4	1.14	27.66	22.33	1.27	224.17	N/A	-9.86 %	-87.66 %	N/A
5	0.61	5.29	9.25	0.73	5.81	9.28	-16.26 %	-9.05 %	-0.32 %
6	0.93	9.44	13.00	0.97	16.21	19.09	-5.01 %	-41.78 %	-31.90 %

control scheme gives significant energy savings ranging from 5% to nearly 30% over the benchmark controller across all test cases. In addition, in all cases the optimal controller attains the target temperature in the same or less time compared to the simple feedback controller.

Cases 2 and 4 present two cases in which the optimal controller far out performs the simple benchmark controller. Both are extreme test cases, in which the initial conditions and disturbances place a large amount of stress on the vehicle AC system. In case 2, the extremely heat-soaked cabin is able to be cooled effectively by the optimal controller in just over 24 minutes, but the simple benchmark controller is barely able to achieve the target cabin temperature before the end of the simulation. The extreme ambient humidity in case 4 similarly presents a trouble for the simple feedback model, as it cannot reach the target temperature before the end of the trial. The optimal controller, however, remains flexible and attains the target cabin air temperature after 22.33 minutes.

Figure 30 compares the OCP and simple feedback controller input (Plot A) and state (Plot B) vector trajectories for case 1. As can be seen in the cabin air temperature (top) and absolute humidity (bottom) plots of Plot B, the start of the cooling period is spent reducing the temperature and absolute humidity of the heat-soaked cabin air. These initial few minutes are aided by heat transfer with the ambient air, as it is at a lower temperature than that of the cabin air. When utilizing the optimal control solution (solid lines), the system stays in recirculation mode with a compressor power (Plot A, bottom) draw of over 2 kW at the beginning in order to cool the cabin air as quickly as possible. However, once the cabin air CO_2 concentration (Plot B, middle) critical limit is reached, the recirculation flap (Plot A, top) opens partially for a mixture of just over 85% recirculated air, allowing warmer ambient air to enter the air system. In response, the compressor power rises and the slope of the change in cabin air temperature reduces in magnitude due to the need to cool the incoming fresh air. The system remains in this position, cooling the cabin at

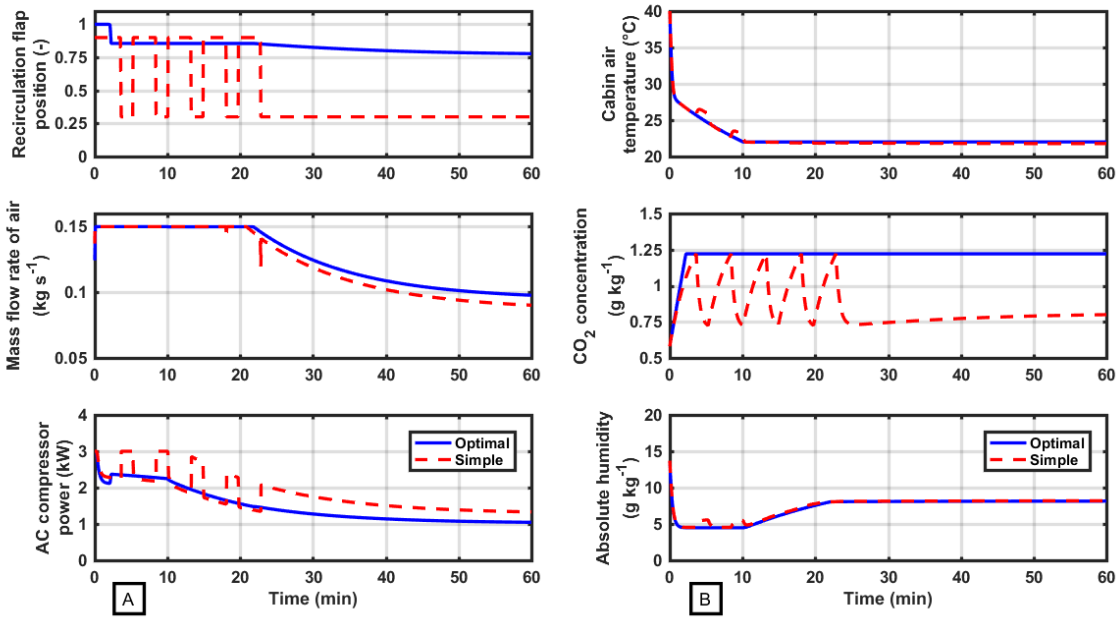

Figure 30: Comparison of the OCP and simple feedback controller input (Plot A) and state (Plot B) vector trajectories for basic test case 1.

roughly the rate of 0.6°C per minute until approximately 10 minutes into the simulation. At this point the mean cabin air temperature attains its target temperature of 22°C. With the target cabin air temperature achieved, the compressor power is reduced, resulting in a steady rise in the evaporator outlet air temperature from the minimum state of 2°C to the maximum level of 10°C. The evaporator outlet absolute humidity rises with the outlet temperature, increasing the cabin air absolute humidity to its steady-state value of 8.135 g H_2O per kg dry air, or a final cabin relative humidity at 22°C of roughly 49%. Once the cabin air temperature and absolute humidity have reached their steady-state values, the blower reduces the mass air flow of the system (Plot A, middle) from the peak of 0.15 $kg \cdot s^{-1}$ steadily down to a final state of just below 0.1 $kg \cdot s^{-1}$.

In comparison with the optimal controller, the simple feedback controller (dashed lines) achieves a similar reduction in the cabin air temperature, but in a coarser manner. As the cabin air CO_2 concentration reaches the critical limit, the recirculation flap position is changed from 90% recirculated air to 70% fresh air, driving the CO_2 concentration down. However, in order to continue cooling the cabin at a steady rate, the AC compressor must respond by increasing its power draw to the maximum allowable value of 3 kW, as the mixing ambient air is warmer and more humid than the recirculated cabin air. These square-wave profiles for the recirculation flap position and AC compressor power continue until the cabin air temperature and absolute humidity reach their steady-state positions. At this point, the mass air flow rate can be reduced and the AC compressor can adequately cool the majority fresh air-recirculated air mixture while maintaining the target cabin conditions. Due to the on-off nature of the compressor power draw and higher steady-state level due to the increased fresh air fraction in the incoming air, the simple feedback-controlled air conditioning system requires just over 15%-more usable power to air condition the vehicle cabin compared to the optimal controller.

The trajectories of the mean interior surface, mean cabin air, and cabin outlet air temperatures for the optimal controller and simple feedback controller are presented in Figure 31 for case 1. The similarity in cabin air and out air temperature profiles between the two control schemes further shows the applicability of the optimal control scheme, given its reduced energy use to achieve the same state. The lower interior surface temperature using the simple feedback control scheme compared to the OCP is due to the slight difference in the cabin air temperature and the target temperature, increasing the convective heat transfer from the warmer cabin surfaces throughout the cool down of the cabin. This difference in the cabin air temperature results from the form of the feedback equation (equation 51 of Section 8.2) for the simple controller not being as constraining as the penalty term in equation 35 (Section 8.1) for the optimal controller.

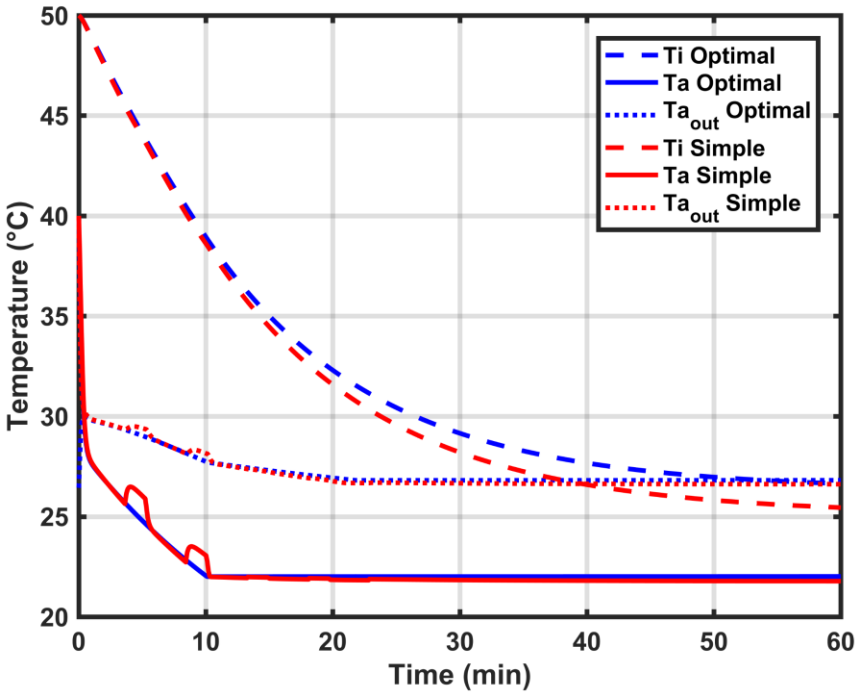

Figure 31: Comparison of the OCP and simple feedback controller cabin mean air, mean interior surface, and outlet air temperature trajectories for basic test case 1.

Figure 32 presents the OCP and simple feedback controller input (Plot A) and state (Plot B) vector trajectories for case 6. In case 6, the solar load is reduced by comparison, but the number of vehicle occupants is increased to four. Similar to case 1, the optimal control scheme (solid lines) for the AC system begins by cooling and dehumidifying the cabin air. However, the effect of the increased number of passengers is immediately apparent as the CO_2 concentration (Plot B, middle) in the cabin rapidly rises to the critical limit within the first minute. In response, the recirculation flap position (Plot A, top) is adjusted to provide a 0.42:1 mixing ratio of recirculated to fresh air in the air system. This maintains the carbon-dioxide concentration at its limit, but slows the cooling of the cabin. Throughout this process, the AC compressor power (Plot A, bottom) remains at its maximum in order to compensate for the four-fold increase in the passenger heat output.

At the 13-minute mark, the cabin air temperature (Plot B, top) achieves its target temperature of 22°C. Thus, the AC compressor reduces its power draw, increasing the evaporator

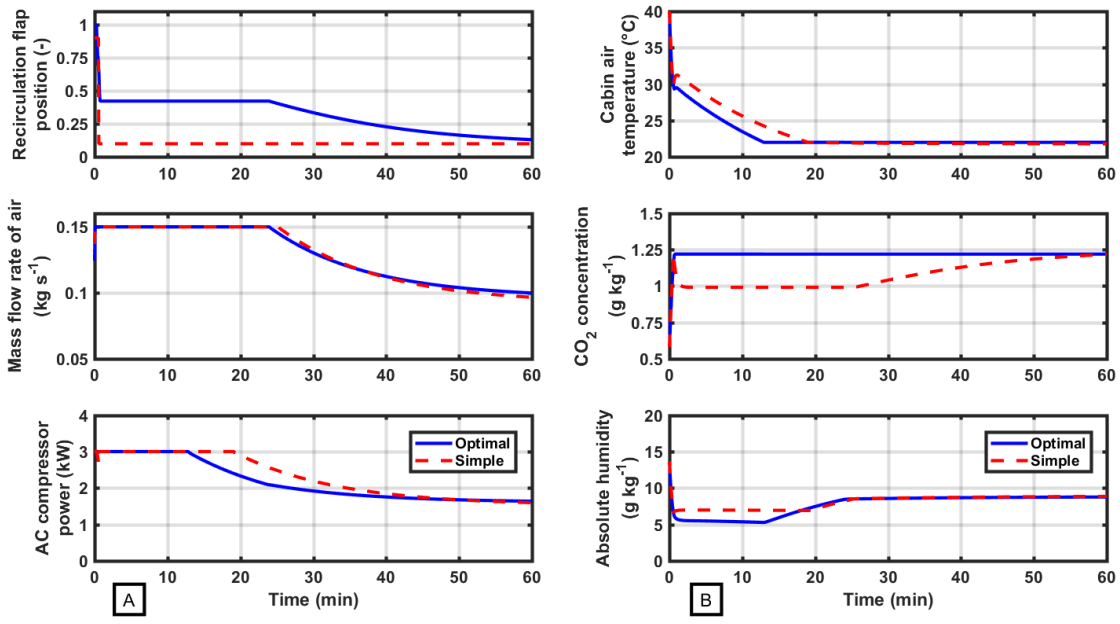

Figure 32: Comparison of the OCP and simple feedback controller input (Plot A) and state (Plot B) vector trajectories for basic test case 6.

outlet air temperature and absolute humidity. The cabin absolute humidity (Plot B, bottom) plateaus at approximately 24 minutes into the simulation, triggering a reduction in the mass air flow rate (Plot A, middle) and recirculation flap position to their final values of approximately 0.1 kg s^{-1} and 0.1, respectively. The AC compressor power, similarly, settles to its final value of approximately 1.64 kW.

By comparison, the simple feedback controller (dashed line) achieves a similar final position for all inputs and states, but due to the coarseness of the recirculation flap position, the benchmark controller takes 32% longer to achieve the target cabin air temperature and uses 5% more energy. This can be seen in more detail in Figure 33, where the comparison of the trajectories of the mean interior surface, mean cabin air, and cabin outlet air temperatures for case 6 are presented for the two control schemes. The simple controller, shown in red lines, has a rise in the cabin air temperature as the partially-cooled cabin is flooded with warmer and more humid ambient air. This requires the AC compressor to run longer at full power, using more energy in comparison to the optical control scheme, presented in blue.

Given the smoother adjustment of input variables, reduction in energy use by the air conditioning system, and the comparable or improved time to achieve the target cabin conditions, these results show the effectiveness of the optimal control scheme in comparison to the simple feedback-controlled system.

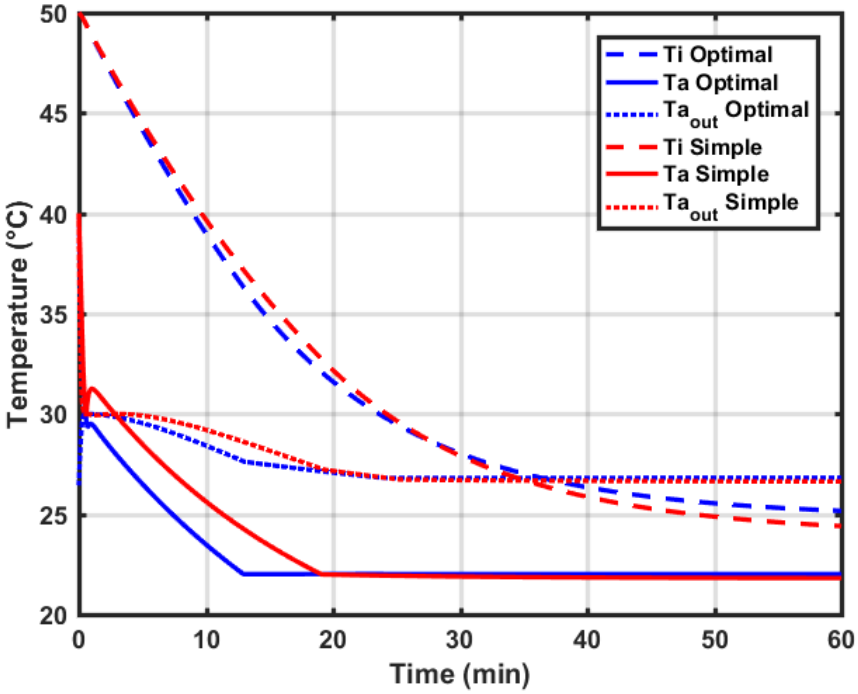

Figure 33: Comparison of the OCP and simple feedback controller cabin mean air, mean interior surface, and outlet air temperature trajectories for basic test case 6.

9.3 Advanced test cases

In order show the flexibility of the optimal control scheme presented in this work, this section presents three advanced test cases employing time-varying disturbance vectors. First, a simulated driving route through a tunnel is presented. Then, a variation in the number of vehicle occupants is adjusted for by the air conditioning control system. Finally, the response of the control scheme to the approximate conditions present during the formation of a thunderstorm is presented.

9.3.1 Tunnel route

This scenario presents the case of a single person driving their electric vehicle on a hot, sunny day along a route that takes them for an extended period of time through a tunnel. Figure 34 presents the disturbance vector trajectories for the simulated tunnel route. The test case begins with

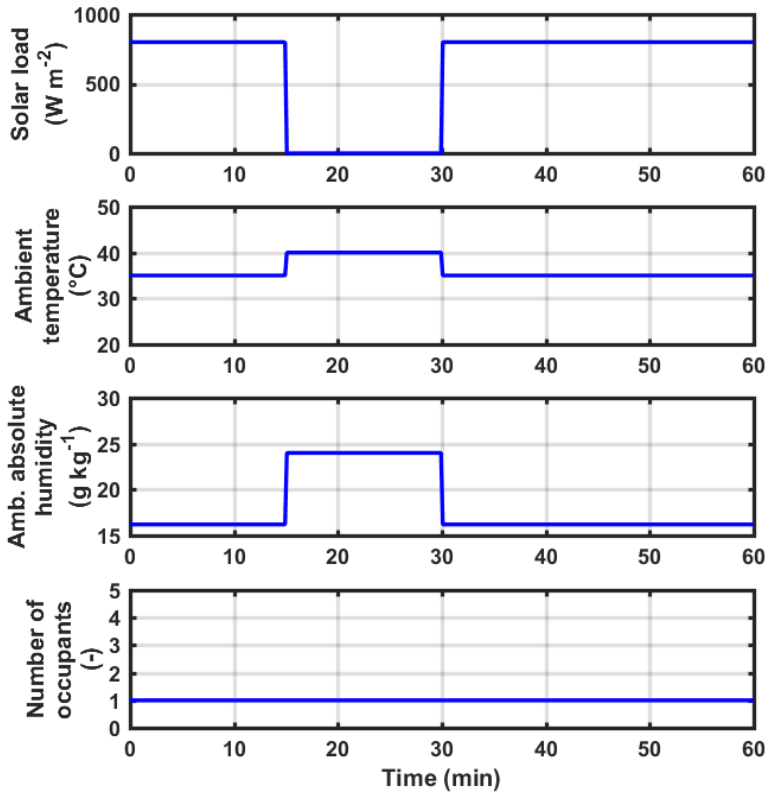

Figure 34: Disturbance vector trajectories for the simulated tunnel route. The simulated tunnel occurs during the period from 15 to 30 minutes.

a 15-minute drive in the sunny conditions of a 35°C day with 45% relative humidity and a solar load of 800 $W \cdot m^{-2}$. At the 15-minute mark, the vehicle enters the tunnel, resulting in a rapid drop in the solar load to 0 $W \cdot m^{-2}$. The ambient temperature and humidity of the tunnel, however, rise in the tunnel to 40°C and 50%, as has been shown to commonly occur in tunnels (Bopp and Peter, 2006). The route takes the vehicle on an extended drive through the tunnel, emerging 15 minutes later to the same ambient conditions as were present at the beginning of the scenario.

Figure 35 shows the input (Plot A) and state (Plot B) vector trajectories for the scenario utilizing the air conditioning optimal control scheme presented in this work. The vehicle cabin begins the scenario at a heat-soaked condition of 50°C mean cabin air temperature, while still at

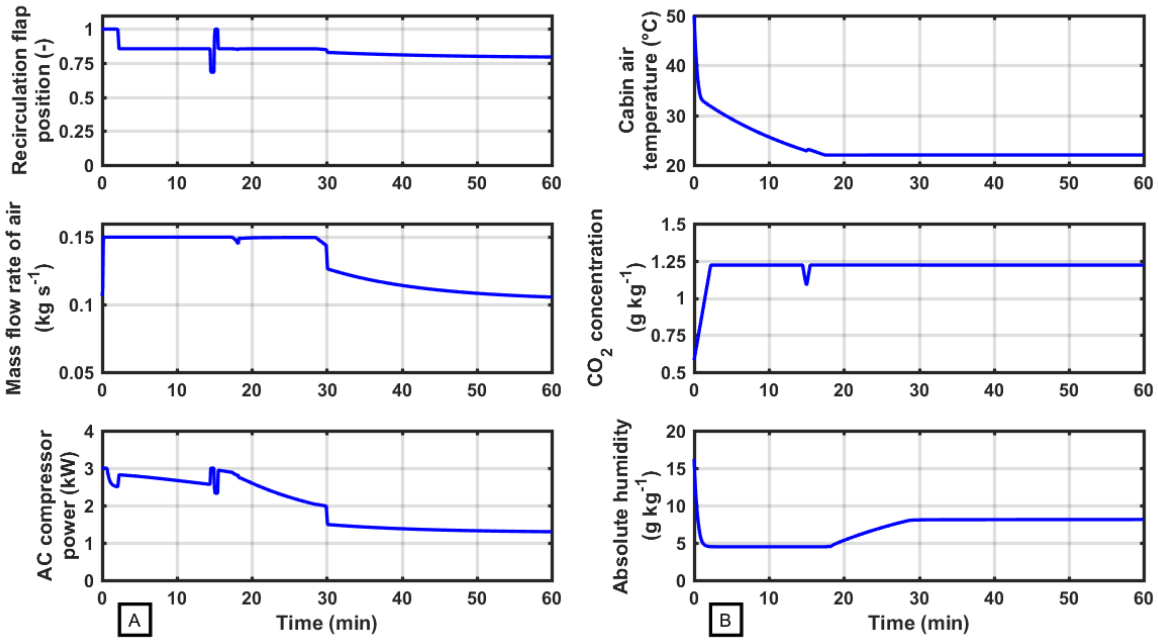

Figure 35: Input (Plot A) and state (Plot B) vector trajectories for the simulated tunnel route.

the ambient absolute humidity of 16.2 g·kg^{-1}. Starting from this elevated position and similar to the trajectories seen in basic test case 1, the air conditioning system begins to rapidly cool and dehumidify the cabin air until the ambient air temperature is achieved in the cabin around one minute from the beginning of the simulation. The AC compressor draws power during this period at near it maximum allowable level, recirculating cooled cabin air through the system. As before, the cabin air CO_2 concentration reaches its critical limit around 2 minutes into the simulation, requiring the position of the recirculation flap to be change to allow roughly 15% fresh air to be mixed in with the recirculated cabin air. This change leads to an increase in the AC compressor power draw to compensate for the warmer and more humid ambient air entering the air system.

At the 15-minute mark, the vehicle enters the tunnel, marked by the rapid changes in all the disturbance vector trajectories (Plot A). These changes are assumed to be numerical artifacts as the optimal controller compensates for the rapid change in the disturbance vector. Such

oscillations will be further investigated and accounted for in future work, but are not observed to affect the final solution. Shortly after the change in ambient conditions and brief oscillation in inputs, the control system compensates for the warmer and more humid ambient air by raising the AC compressor power draw. Thus, entering and driving in the tunnel has little effect on the cabin conditions, other than a brief increase in the cabin air temperature just after the 15-minute mark in Plot B (top).

The cabin air temperature achieves its target of 22°C after 17.5 minutes, allowing the control system to reduce its AC compressor power draw and, as a result, raise the evaporator outlet air temperature. Coincidentally, the cabin absolute humidity reaches its steady-state level at approximately the point that the vehicle exits the tunnel into the slightly cooler and less humid ambient conditions at the 30-minute mark. In response, the AC compressor power and mass air flow rates drop sharply as the control system trends to a steady-state balance between the two input variables of approximately 1.3 kW and 0.1 kg s^{-1} in order to maintain the target cabin conditions.

This scenario shows the flexibility of the present optimal control scheme to effectively compensate for simultaneous, rapid changes in the ambient conditions while still minimizing the energy use of the AC system and maintaining desired cabin conditions.

9.3.2 Variation in number of occupants

In this section, the number of occupants present within the vehicle cabin is changed during the course of the simulation. Figure 36 shows the disturbances for the current scenario. The solar load, ambient temperature, and ambient humidity remain constant for the entire 60-minute test case at 800 $W \cdot m^{-2}$, 40°C, and 19.0 g H_2O per kg dry air, respectively. The cabin begins at a heat-soaked condition of 50°C air temperature and 60°C interior surface temperature. Only the driver is present in the vehicle until the 5-minute mark, at which point three passengers join for a 25-

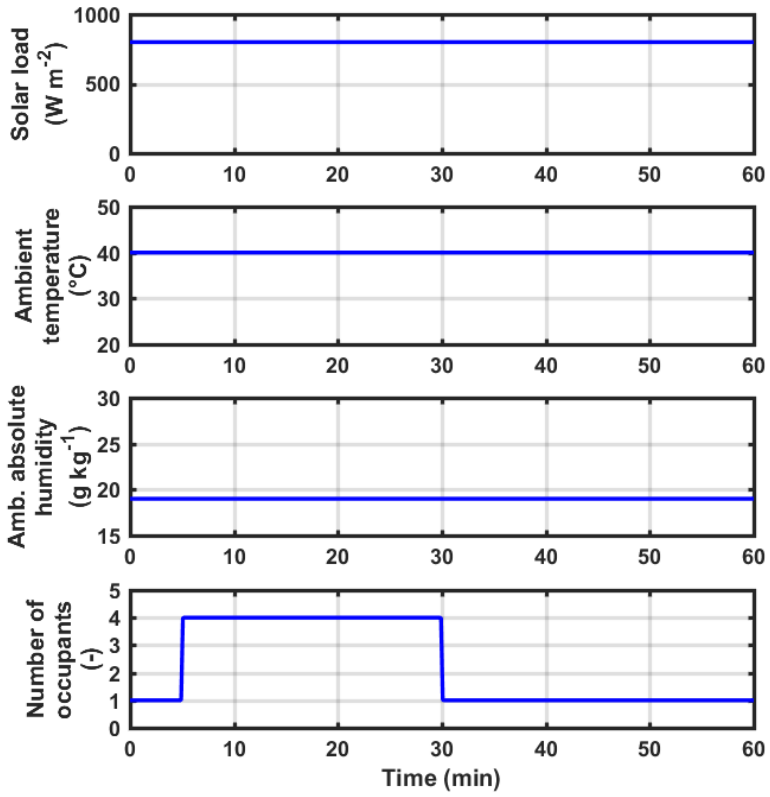

Figure 36: Disturbance vector trajectories for the scenario of a variation in the number of passengers. The increase in the number of passengers occurs during the period from 5 to 30 minutes.

minute drive. Finally, the three passengers exit the vehicle and the driver continues alone until the end of the test case.

In Figure 37, the input (Plot A) and state (Plot B) vector trajectories for the current scenario are shown. Once again, the AC system begins by cooling and dehumidifying the cabin air by applying max AC compressor power (Plot A, bottom), fully recirculating the cabin air (Plot A, top), and having the blower output the maximum mass air flow (Plot A, middle). At the 5-minute mark, three passengers join the driver in the vehicle. This increases the heat, H_2O, and CO_2 outputs internal to the cabin. In order to maintain the CO_2 concentration (Plot B, middle) of the cabin below the critical limit, the controller floods the cabin with fresh air, setting the recirculation flap

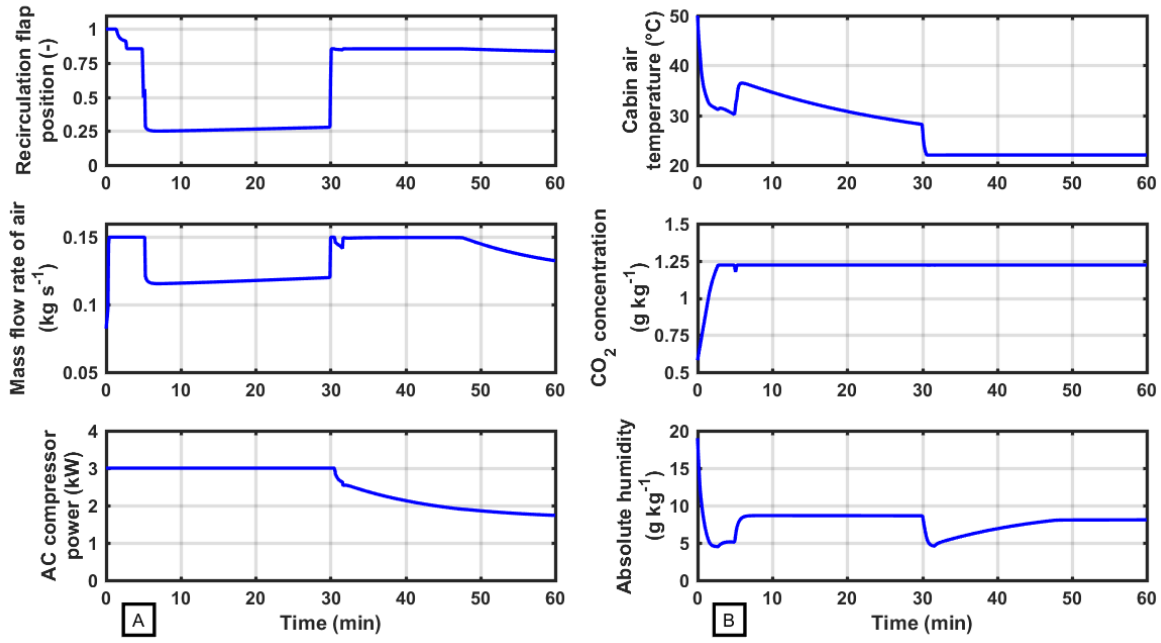

Figure 37: Input (Plot A) and state (Plot B) vector trajectories for the scenario of a variation in the number of passengers.

to approximately 25% recirculated air. However, the very warm ambient air, high thermal output of the four vehicle occupants, and still uncooled cabin drive the evaporator outlet ambient temperature to its maximum, despite the AC compressor being at full power. In order to meet the evaporator outlet temperature constraint, the system reduces the mass flow rate of the air. The cabin air temperature (Plot B, top) rises, but then begins falling again at a steady rate until the 30-minute mark. At this point in time, the three additional passengers exit the vehicle. With the reduction in the heat, H_2O, and CO_2 outputs internal to the cabin, the optimal control system is able to quickly cool the cabin air down to its target temperature. In turn, the AC compressor power falls to a final level of about 1.74 kW. The mass flow rate of air falls as well once the cabin absolute humidity (Plot B, bottom) reaches flattens out to its final position at approximately 48 minutes.

In this scenario, the effect of a rapid change in the number of vehicle occupants during the cooling of the vehicle cabin by an optimally controlled AC system were presented. The test case

further shows the robustness of the optimal control scheme, despite extreme changes in the disturbances.

9.3.3 **Thunderstorm**

In the final scenario with time-varying disturbances, the approximate conditions present during the formation of a thunder- or heavy rain-storm are simulated. To approximate these conditions, a meteogram[1] for a thunderstorm in 2010 in Lille, France was used (Meteoblue.com, 2018).

Figure 38 presents the disturbances for the current scenario. During the test case, the solar load (top) and number of passengers (bottom) remain constant at 200 $W \cdot m^{-2}$ and 1, respectively. The ambient temperature (middle-top) and humidity (middle-bottom) begin at 35°C and 50% (18.09 g-H2O per kg-dry-air), respectively, and remain at these levels until the 5-minute mark. The cabin air temperature begins at 45°C and the interior surface temperature at 50°C. The starting cabin air absolute humidity is the same as ambient, resulting in an initial relative humidity of 29.31%.

At the 5-minute mark, the simulated thunderstorm begins, decreasing the ambient temperature to 30°C over 15 minutes and increasing the ambient relative humidity to 85% (23.40 g-H2O per kg-dry-air) in 10 minutes. The peak in the ambient relative humidity at approximately 12 minutes is due to the functional relationship between absolute humidity, temperature, and relative humidity. As the relative humidity is rising quicker than the temperature is falling during the formation of the rain storm, the warmer air can carry more water vapor due to its higher dew

[1] A meteogram is a graphical representation of multiple meteorological variables (temperature, relative humidity, pressure, so on) with respect to time for a given location [NWS (2009). *National Weather Service Glossary - Meteogram*, NOAA.]

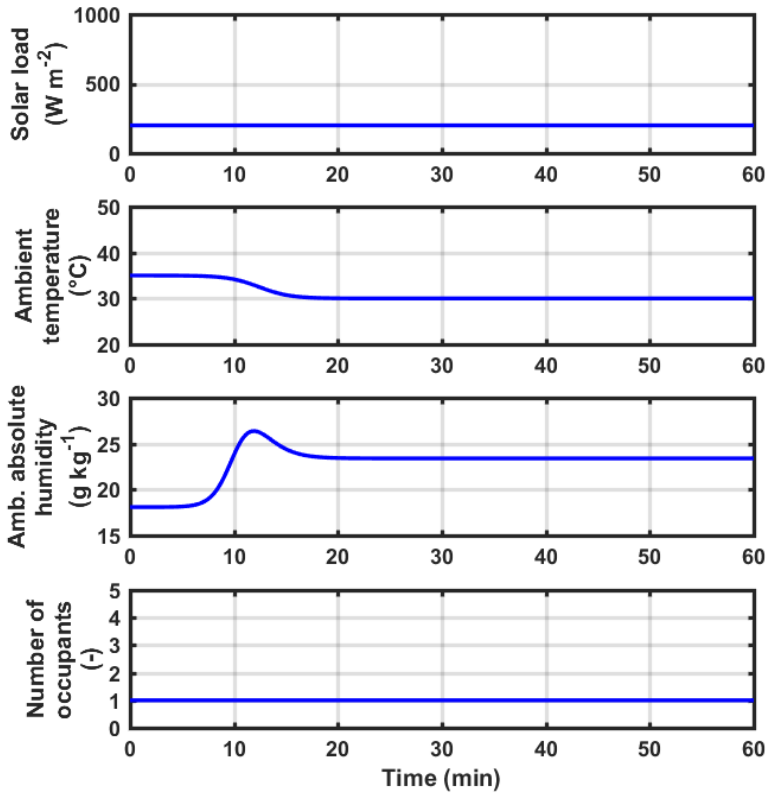

Figure 38: Disturbance vector trajectories for a simulated thunderstorm. The increase change in the ambient conditions begins at t = 5 minutes.

point. Once the relative humidity settles to its final position, the temperature is able to catch up, lowering the dew point of the air and, thus, reducing the absolute humidity of the ambient air.

Figure 39 shows the input (Plot A) and state (Plot B) vector trajectories for the simulated thunderstorm. The results are very similar to that of basic test case 1 presented previously. Due to the reduced solar load, the cabin air temperature actually reaches its target temperature quicker in the current scenario compared to basic test case 1 (8.9 versus 10.2 minutes), despite the increased ambient temperature and humidity. Therefore, the previously described response of the optimal control scheme holds for the current scenario as well.

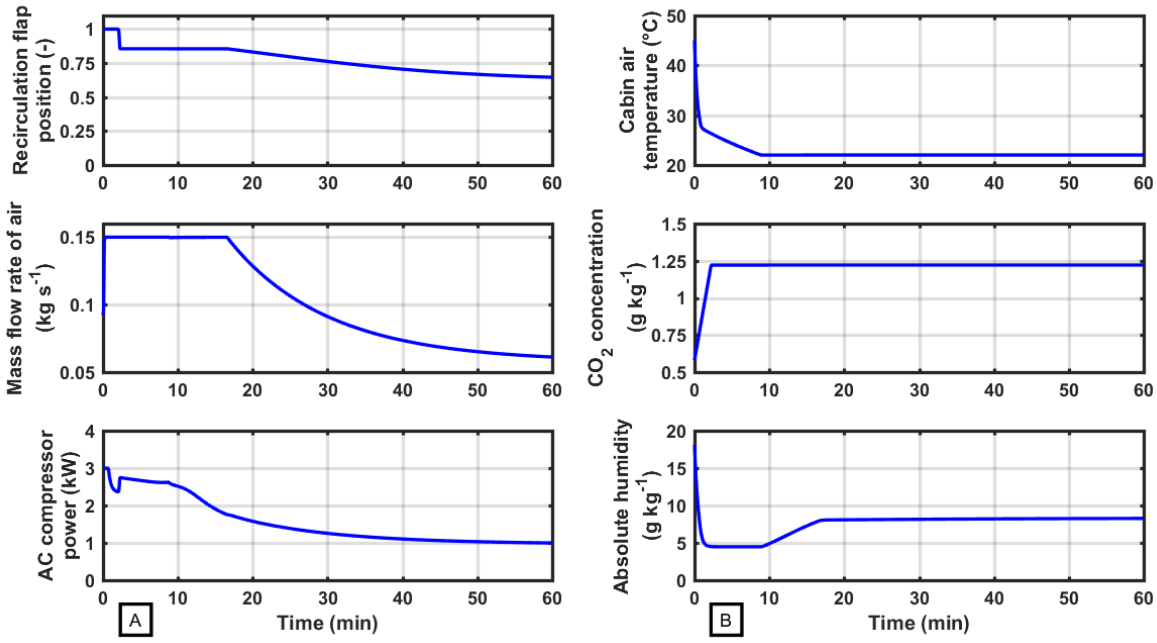

Figure 39: Input (Plot A) and state (Plot B) vector trajectories for a simulated thunderstorm.

This test case shows the relative low effect that a simulated thunderstorm has on the cooling of a vehicle cabin using the proposed optimal control scheme.

9.4 Summary of results

In this chapter, the effectiveness of the non-linear, constrained optimal control scheme to limit the energy consumption of the EV air conditioning system while simultaneously achieving a target cabin temperature was tested. The proposed model compared well to a benchmark simple feedback controller, using between five to and thirty percent less energy in test cases with constant disturbances, all while obtaining the target cabin temperature in less time. In addition to these use-cases, the flexibility and robustness of the optimal controller was shown for scenarios involving time-varying disturbances.

10. CONCLUSIONS AND RECOMMENDATIONS

10.1 Conclusions

In this work, an optimal control scheme for an electric vehicle air conditioning system was developed in order to simultaneously reduce the energy consumption of the system, and achieve the targeted cooling level of the cabin air and safe CO_2 concentration.

A lumped-parameter approach was used to model the vehicle cabin, with the mean interior surface temperature, mean air temperature, CO_2 concentration, and absolute humidity selected as the cabin state variables. Different approximations from the literature for the cabin outlet air temperature were explored, with the formulation from Frank (1971) selected as the best approximation given the cooling condition of the cabin.

The air system, consisting of a recirculation flap, blower, and attached AC evaporator were modelled on a component basis, as proposed by Schaut and Sawodny (2018, *under review*). It was assumed that the outlet of the evaporator was always at the saturated condition, simplifying the modeling of evaporator. The input variables were selected as the recirculation flap position, mass flow rate of air created by the blower, and the power supplied to the AC compressor, which generates the cooling rate at the evaporator. The COP of the AC system was assumed constant. The system disturbances were the solar heat load, ambient temperature, ambient absolute humidity, and number of vehicle occupants. The occupants each are constant sources of heat, water vapor, and carbon-dioxide.

A constrained, non-linear optimal control problem was then defined with a cost function whose goal was to minimize the energy consumption of the vehicle while compensating for the target cabin air temperature. Constraints were placed on the outlet temperature of the evaporator, the cabin CO_2 concentration, and the allowable values for the inputs. The OCP was then

transformed into a non-linear program using the direct multiple shooting strategy and a fourth-order Runge-Kutta method for discretization. The NLP was solved using the IPOPT solver, with the required derivatives supplied by the CasADi toolkit.

The effectiveness of the optimal control method was tested using scenarios with both time-varying and constant disturbances. The proposed scheme was compared to the response of a simple feedback controller given constant disturbances. The optimal controller resulted in significant energy savings in comparison to the benchmark controller, ranging from 5 to nearly 30% across all test cases. In addition, the proposed control scheme reached the target cabin temperature in the same or less time than the simple feedback controller. The optimal control scheme for the EV AC system was also tested in more realistic test cases employing time-varying disturbances. Scenarios tested included a simulated driving route with an extended period driving in a tunnel, a rapid variation in the number of vehicle occupants, and a simulated thunderstorm. The proposed model performed well in all cases, showing its flexibility and robust ability to minimizing the energy consumption of the air conditioning system while simultaneously cooling the vehicle cabin to targeted levels.

10.2 Recommendations

To improve the control scheme developed in this study, it would be advantageous to connect the air conditioning model to a resistive heater model within the air system, forming a joint heating, ventilation, and air conditioning (HVAC) system model. This would bring the control scheme closer to a realistic vehicle system, allowing for control of the cabin conditions and reduction of system energy consumption at a wider range of operating conditions.

Expanded system constraints would also allow for more nuanced control of the cabin state. Examples of additional constraints could be a window fogging model, which would limit the

absolute humidity and temperature in the cabin based on ambient conditions, and a more detailed thermal comfort model, among other possibilities.

Finally, adding a “slider” to the weighting of occupant thermal comfort versus energy savings in the cost function would be a good addition to the model. This would allow for the time-dependent shifting of the target of the control scheme from maintaining the state in the cabin to, for example, an even larger focus on energy savings within the HVAC system to further extend the range of the electric vehicle. Such a feature would be useful in cases of low battery charge level.

REFERENCES

Andersson, J. A. E., J. Gillis, G. Horn, J. B. Rawlings and M. Diehl (2018), "Casadi: A Software Framework for Nonlinear Optimization and Optimal Control," *Mathematical Programming Computation* DOI: 10.1007/s12532-018-0139-4.

ASHRAE (2001), "Fundamentals Handbook," *American Society of Heating, Refrigerating and Air Conditioning Engineers, Atlanta* Vol. 111

Bai, Y., H. Zhuang and D. Wang (2006). *Advanced Fuzzy Logic Technologies in Industrial Applications (Advances in Industrial Control)*, Springer-Verlag.

Bell, I. H., J. Wronski, S. Quoilin and V. Lemort (2014), "Pure and Pseudo-Pure Fluid Thermophysical Property Evaluation and the Open-Source Thermophysical Property Library Coolprop," *Industrial & Engineering Chemistry Research* Vol. 53(6) pp. 2498-2508 DOI: 10.1021/ie4033999.

Bequette, B. W. (1998). *Process Dynamics : Modeling, Analysis, and Simulation*. Upper Saddle River, NJ, Prentice Hall PTR.

Bock, H. G. and K.-J. Plitt (1984), "A Multiple Shooting Algorithm for Direct Solution of Optimal Control Problems," *IFAC Proceedings Volumes* Vol. 17(2) pp. 1603-1608

Bopp, R. and A. Peter (2006). *Windshield Fogging in Road Tunnels–Final Results*. 3rd International Conference 'Tunnel Safety and Ventilation'. Graz, Austria.

Bryson, A. E. (1996), "Optimal Control-1950 to 1985," *IEEE Control Systems Magazine* Vol. 16(3) pp. 26-33 DOI: 10.1109/37.506395.

Danca, P., F. Bode, I. Nastase and A. Meslem (2017), "On the Possibility of Cfd Modeling of the Indoor Environment in a Vehicle," *Energy Procedia* Vol. 112 pp. 656-663 DOI: https://doi.org/10.1016/j.egypro.2017.03.1133.

Delahanty, J. C. (2015). *Desorption of Ammonia-Water Mixtures in Microscale Geometries for Miniaturized Absorption Systems*, Georgia Institute of Technology.

Delahanty, J. C., S. Garimella and M. A. Garrabrant (2015), "Design of Compact Microscale Geometries for Ammonia–Water Desorption," *Science and Technology for the Built Environment* Vol. 21(3) pp. 365-374 DOI: 10.1080/23744731.2015.1015906.

Determan, M. D. and S. Garimella (2011), "Ammonia–Water Desorption Heat and Mass Transfer in Microchannel Devices," *International Journal of Refrigeration* Vol. 34(5) pp. 1197-1208 DOI: http://dx.doi.org/10.1016/j.ijrefrig.2011.02.004.

Determan, M. D. and S. Garimella (2012), "Design, Fabrication, and Experimental Demonstration of a Microscale Monolithic Modular Absorption Heat Pump," *Applied Thermal Engineering* Vol. 47 pp. 119-125 DOI: http://dx.doi.org/10.1016/j.applthermaleng.2011.10.043.

Farzaneh, Y. and A. A. Tootoonchi (2008), "Controlling Automobile Thermal Comfort Using Optimized Fuzzy Controller," *Applied Thermal Engineering* Vol. 28(14) pp. 1906-1917 DOI: https://doi.org/10.1016/j.applthermaleng.2007.12.025.

Frank, W. (1971), "Fragen Der Beheizung Und Belüftung Von Kraftfahrzeugen," *ATZ* Vol. 13 pp. 369-376

Gani, R., C. A. Ruiz and I. T. Cameron (1986), "A Generalized Model for Distillation Columns—I," *Computers & Chemical Engineering* Vol. 10(3) pp. 181-198 DOI: http://dx.doi.org/10.1016/0098-1354(86)85001-3.

Garimella, S., C. M. Keinath, J. C. Delahanty, D. C. Hoysall, M. A. Staedter, A. Goyal and M. A. Garrabrant (2016), "Development and Demonstration of a Compact Ammonia–Water Absorption Heat Pump Prototype with Microscale Features for Space-Conditioning Applications," *Applied Thermal Engineering* Vol. 102 pp. 557-564 DOI: https://doi.org/10.1016/j.applthermaleng.2016.03.169.

Garrabrant, M., R. Stout, P. Glanville, C. Keinath and S. Garimella (2013), "Development of Ammonia-Water Absorption Heat Pump Water Heater for Residential and Commercial Applications," (55515) p. V001T004A002 DOI: 10.1115/ES2013-18121.

Gately, C. K., L. R. Hutyra and I. S. Wing (2015), "Cities, Traffic, and Co2: A Multidecadal Assessment of Trends, Drivers, and Scaling Relationships," *Proceedings of the National Academy of Sciences* p. 201421723

Goyal, A., A. A. Roeder and S. Garimella (2017), "Generalized Transient Simulation of Two-Phase Heat Exchangers Using Zeotropic Fluid Mixtures," *In Preparation*

Großmann, H. (2013). *Pkw-Klimatisierung: Physikalische Grundlagen Und Technische Umsetzung*, Springer-Verlag.

He, H., M. Yan, C. Sun, J. Peng, M. Li and H. Jia (2018), "Predictive Air-Conditioner Control for Electric Buses with Passenger Amount Variation Forecast☆," *Applied Energy* Vol. 227 pp. 249-261 DOI: https://doi.org/10.1016/j.apenergy.2017.08.181.

Huang, Y., A. Khajepour, F. Bagheri and M. Bahrami (2016), "Optimal Energy-Efficient Predictive Controllers in Automotive Air-Conditioning/Refrigeration Systems," *Applied Energy* Vol. 184 pp. 605-618 DOI: https://doi.org/10.1016/j.apenergy.2016.09.086.

Ibrahim, B. S. K. K., M. A. N. Aziah, S. Ahmad, R. Akmeliawati, H. M. I. Nizam, A. G. A. Muthalif, S. F. Toha and M. K. Hassan (2012), "Fuzzy-Based Temperature and Humidity Control for Hv Ac of Electric Vehicle," *Procedia Engineering* Vol. 41 pp. 904-910 DOI: https://doi.org/10.1016/j.proeng.2012.07.261.

IEA (2018). Global Ev Outlook 2018: Towards Cross-Modal Electrification. International Energy Agencyp.

Jabardo, J. M. S., W. G. Mamani and M. R. Ianella (2002), "Modeling and Experimental Evaluation of an Automotive Air Conditioning System with a Variable Capacity Compressor," *International Journal of Refrigeration* Vol. 25(8) pp. 1157-1172 DOI: https://doi.org/10.1016/S0140-7007(02)00002-6.

Jeong, S., B. H. Kang and S. W. Karng (1998), "Dynamic Simulation of an Absorption Heat Pump for Recovering Low Grade Waste Heat," *Applied Thermal Engineering* Vol. 18(1) pp. 1-12 DOI: http://dx.doi.org/10.1016/S1359-4311(97)00040-9.

Keinath, C. M., D. Hoysall, J. C. Delahanty, M. D. Determan and S. Garimella (2015), "Experimental Assessment of a Compact Branched Tray Generator for Ammonia–Water Desorption," *Science and Technology for the Built Environment* Vol. 21(3) pp. 348-356 DOI: 10.1080/23744731.2014.1000797.

Khayyam, H. (2013), "Adaptive Intelligent Control of Vehicle Air Conditioning System," *Applied Thermal Engineering* Vol. 51(1) pp. 1154-1161 DOI: https://doi.org/10.1016/j.applthermaleng.2012.10.028.
Khayyam, H., A. Z. Kouzani, E. J. Hu and S. Nahavandi (2011), "Coordinated Energy Management of Vehicle Air Conditioning System," *Applied Thermal Engineering* Vol. 31(5) pp. 750-764 DOI: https://doi.org/10.1016/j.applthermaleng.2010.10.022.
Kim, B. and J. Park (2007), "Dynamic Simulation of a Single-Effect Ammonia–Water Absorption Chiller," *International Journal of Refrigeration* Vol. 30(3) pp. 535-545 DOI: http://dx.doi.org/10.1016/j.ijrefrig.2006.07.004.
Kohlenbach, P. and F. Ziegler (2008), "A Dynamic Simulation Model for Transient Absorption Chiller Performance. Part I: The Model," *International Journal of Refrigeration* Vol. 31(2) pp. 217-225 DOI: http://dx.doi.org/10.1016/j.ijrefrig.2007.06.009.
Lee, H., Y. Hwang, I. Song and K. Jang (2015), "Transient Thermal Model of Passenger Car's Cabin and Implementation to Saturation Cycle with Alternative Working Fluids," *Energy* Vol. 90 pp. 1859-1868 DOI: https://doi.org/10.1016/j.energy.2015.07.016.
Ling, J., V. Aute, Y. Hwang and R. Radermacher (2013), "A New Computational Tool for Automotive Cabin Air Temperature Simulation," *SAE Int. J. Passeng. Cars - Mech. Syst.* Vol. 6(2) pp. 841-846 DOI: 10.4271/2013-01-0868.
Luyben, W. L. (1989). *Process Modeling, Simulation and Control for Chemical Engineers*, McGraw-Hill Higher Education.
Marcos, D., F. J. Pino, C. Bordons and J. J. Guerra (2014), "The Development and Validation of a Thermal Model for the Cabin of a Vehicle," *Applied Thermal Engineering* Vol. 66(1) pp. 646-656 DOI: https://doi.org/10.1016/j.applthermaleng.2014.02.054.
Mathworks (2016). *Matlab*. Natick, Massachusetts, The Mathworks Inc.
Meteoblue.com (2018). *Thunderstorms*, meteoblue.
Nitz, J. and W. H. Hucho (1979). *The Heat Transfer Coefficient of a Passenger Car's Body*, SAE International.
NWS (2009). *National Weather Service Glossary - Meteogram*, NOAA.
Ogawa, A. (2009). *Psychrometric Chart for Sea-Level Pressure Using Si Units*. PsychrometricChart.SeaLevel.SI.svg, Vol. 1406 by 1031 pixels.
OSHA (2017). *Osha Technical Manual*, [Washington, D.C.] : U.S. Dept. of Labor, Occupational Safety and Health Administration
Patankar, S. (1980). *Numerical Heat Transfer and Fluid Flow*, CRC press.
Schaut, S. and O. Sawodny (2018, *under review*), "Thermal Management for the Cabin of a Battery Electric Vehicle Considering Passengers' Comfort," *IEEE Transactions on Control Systems Technology*
Shampine, L. F. and M. W. Reichelt (1997), "The Matlab Ode Suite," *SIAM Journal on Scientific Computing* Vol. 18(1) pp. 1-22 DOI: 10.1137/s1064827594276424.
Singh, S. and H. Abbassi (2018), "1d/3d Transient Hvac Thermal Modeling of an Off-Highway Machinery Cabin Using Cfd-Ann Hybrid Method," *Applied Thermal*

Engineering Vol. 135 pp. 406-417 DOI: https://doi.org/10.1016/j.applthermaleng.2018.02.054.
Skogestad, S. (1997), "Dynamics and Control of Distillation Columns: A Tutroial Introduction," *Chemical Engineering Research and Design* Vol. 75(6) pp. 539-562 DOI: http://dx.doi.org/10.1205/026387697524092.
Srikhirin, P., S. Aphornratana and S. Chungpaibulpatana (2001), "A Review of Absorption Refrigeration Technologies," *Renewable and Sustainable Energy Reviews* Vol. 5(4) pp. 343-372 DOI: http://dx.doi.org/10.1016/S1364-0321(01)00003-X.
Torregrosa-Jaime, B., F. Bjurling, J. M. Corberán, F. Di Sciullo and J. Payá (2015), "Transient Thermal Model of a Vehicle's Cabin Validated under Variable Ambient Conditions," *Applied Thermal Engineering* Vol. 75 pp. 45-53 DOI: https://doi.org/10.1016/j.applthermaleng.2014.05.074.
Viswanathan, V. K., A. S. Rattner, M. D. Determan and S. Garimella (2013), "Dynamic Model for a Small-Capacity Ammonia–Water Absorption Chiller," *HVAC&R Research* Vol. 19(7) pp. 865-881 DOI: 10.1080/10789669.2013.833974.
Wächter, A. and L. T. Biegler (2006), "On the Implementation of an Interior-Point Filter Line-Search Algorithm for Large-Scale Nonlinear Programming," *Mathematical Programming* Vol. 106(1) pp. 25-57 DOI: 10.1007/s10107-004-0559-y.
Wang, S., J. Gu, T. Dickson, J. Dexter and I. McGregor (2005), "Vapor Quality and Performance of an Automotive Air Conditioning System," *Experimental Thermal and Fluid Science* Vol. 30(1) pp. 59-66 DOI: https://doi.org/10.1016/j.expthermflusci.2005.03.019.
Ye, T. (2013). *A Statistical Approach for Correlation/Validation of Hot-Soak Terminal Temperature of a Vehicle Cabin Cfd Model*, SAE International.
Zhang, Q., S. Stockar and M. Canova (2016), "Energy-Optimal Control of an Automotive Air Conditioning System for Ancillary Load Reduction," *IEEE Transactions on Control Systems Technology* Vol. 24(1) pp. 67-80 DOI: 10.1109/TCST.2015.2418322.
Zinet, M., R. Rulliere and P. Haberschill (2012), "A Numerical Model for the Dynamic Simulation of a Recirculation Single-Effect Absorption Chiller," *Energy Conversion and Management* Vol. 62 pp. 51-63 DOI: http://dx.doi.org/10.1016/j.enconman.2012.04.007.